UNIVERSITY OF CINCINNATI

Date: 06/16/2009

I, Nilesh Billade **,**

hereby submit this original work as part of the requirements for the degree of:

Doctor of Philosophy

in Mechanical Engineering

It is entitled:

Mechanical Characterization, Computational Modeling, and Biological Considerations for Carbon Nanomaterial-Agarose Composites for Tissue Engineering Applications

Student Signature: Nilesh Billade

This work and its defense approved by:

Committee Chair: Dr. Kumar Vemaganti

Dr. Shawn Hunter

Dr. Mark J. Schulz

Dr. Yijun Liu

Approval of the electronic document:

I have reviewed the Thesis/Dissertation in its final electronic format and certify that it is an accurate copy of the document reviewed and approved by the committee.

Committee Chair signature: Dr. Kumar Vemaganti

Mechanical Characterization, Computational Modeling and Biological Considerations for Carbon Nanomaterial-Agarose Composites for Tissue Engineering Applications

A dissertation submitted to the

Graduate School

of the University of Cincinnati

in partial fulfillment of the

requirements for the degree of

DOCTOR OF PHILOSOPHY

in the Department of Mechanical Engineering

of the College of Engineering

2009

by

Nilesh S. Billade

B.E., Mechanical Engineering, University of Pune, Pune, India, 2001

M.S., Mechanical Engineering, University of Cincinnati, Cincinnati, OH, 2004

Committee Chair: Dr. Kumar Vemaganti

Committee Members: Dr. Shawn Hunter (Co-advisor)
Dr. Mark J. Schulz
Dr. Yijun Liu

Abstract

Tissue engineering (TE) is an emerging technique to develop biological substitutes for replacing damaged tissues and organs. However, currently used biomaterials for making TE scaffolds are considerably weaker than the native tissue and may not withstand mechanical stimuli during culture needed in TE. Carbon nanomaterials (CNMs) are known to enhance the stiffness of many engineering materials. In this research we explore the use of carbon nanomaterials as reinforcements for tissue engineering scaffold biomaterials. The candidate biomaterial used for this research is agarose, a hydrogel used in articular cartilage tissue engineering.

This research focuses on two broad aspects. The first deals with the application of nanotechnology to tissue engineering in order to develop better scaffold materials and the second deals with the mechanical characterization and computational modeling of agarose and its nanocomposites as biphasic materials. This dissertation is divided into three parts. In part A, the effect of carbon nanofiber (CNF) concentration on the mechanical properties and biocompatibility of agarose is studied through mechanical testing and cell viability tests. We find that the mechanical properties of the agarose-nanocomposite improve with the addition of CNFs in a concentration dependent manner. Also, the agarose-CNF nanocomposites do not display any significant cytotoxicity. In

part B, a variety of CNMs with different kinds of functionalizations are used to study the effect of type and functionalization of the CNMs on the mechanical properties and biocompatibility of agarose. The CNM type and functionalization that gives the best improvement in the mechanical properties of agarose without compromising its biocompatibility is found to be CNFs with COOH type of functionalization. These are selected for detailed mechanical testing and computational modeling in part C. Mechanical testing protocols are developed to model agarose and its nanocomposites as biphasic materials. Multistep unconfined compression stress-relaxation tests are used to develop constitutive equations for the solid phase and confined compression creep tests are used to develop constitutive equations for the fluid phase. The solid phase is modeled using the pseudo-elasticity theory coupled with compressible hyperelasticity to model the hysteretic stress-strain data obtained during the loading-unloading tests. The fluid phase is modeled using a strain-dependent permeability. The computational models developed closely agree with the experimental results.

Acknowledgements

First and foremost, I gratefully acknowledge the constant support, motivation and guidance provided by my advisor Dr. Kumar Vemaganti. It has been a pleasant experience working with him for all these years. He has definitely helped me evolve in several ways. I thank him from the bottom of my heart for being a big inspiration to me throughout my graduate life.

I would also like to thank Dr. Shawn Hunter, my co-advisor, for introducing me to the experimental side of research. I am very thankful for his contribution in laying down the research objectives and developing the approach for the experimental part of this research. Thanks to Dr. Yijun Liu for his suggestions and remarks and for serving on my committee. He has been a great mentor during my graduate studies at UC.

Special thanks to Dr. Mark J. Schulz and Dr. Vesselin Shanov at the Nanoworld and Smart Materials and Devices Laboratory for their invaluable help in this research. I really appreciate their generosity, not only for providing carbon nanomaterials for this research, but also for sharing their knowledge and experience which really played a vital role in improving the quality of this research. On that note, I would also like to thank Pravahan Salunke from the Nanoworld lab for being such a big help with the experiments. Thanks also to Mahyar Pourriahi for his help with the biocompatibility

experiments.

This research would not have been possible without the cooperation and support of the Department of Biomedical Engineering at UC. Thanks to Cindy Gooch for helping me with the biocompatibility experiments. Thanks to Dr. David Butler and Dr. Jason Shearn for allowing me to use the facilities at the Department of Biomedical Engineering.

I would also like to thanks Dr. Balakrishna Haridas for providing me the opportunity to work on interesting biomedical engineering projects and for supporting me partly during my graduate studies. Thanks also to Dr. Ronald Huston for being a great mentor throughout my graduate studies.

This has been a long journey and I have several people to thank who have helped me in direct or indirect ways. All in all, it has been a wonderful experience studying at the University of Cincinnati. I have been lucky to have lived with wonderful roommates through these years. Thanks to Abhijit Jadhav, Shalyajit Jadhav, Kiran Aware and Pushkaraj Deshmukh in the early years and Mandar Kulkarni, Milind Bapat and Shardool Chirputkar towards the end. Thanks also to my friends at UC; Mitesh Oswal, Bhargava Sista, Tirrthankar Bhattacharjee, Sagar Bhamare, Sujit Mahajan, Balaji Sharma, Balakumar Swaminathan, Vikram Radhakrishnan, Krishnaveni Mellachervu, Ananth Gopalakrishnan, Rahul Nambiar, Amit Deshpande, Shazia Sheikh, Manoj Dhanotiya, Rahul Patki, Matin Khan, Amit Naik, Shrikant Pattnaik, Won-Joon Song, Elizabeth Boeckmann, Rosaline Banner and Suresh Alla. I would like to thank them all for their moral support and for making my stay in Cincinnati worthwhile. Thanks also to my friends outside UC; Swarup Nanda, Balaji Srinivasan, Kishore Mudaliar, Anish Surendran and Shekhar Gandhi for helping me in innumerable ways, both deliberately

and unknowingly.

Special thanks to Esra Roan for being such a big motivation and a very nice friend. I would also like to specially thank Larry Schartman for being a great friend and guide. It was a great experience working with him.

I would also like to express my gratitude to the makers of Ramen noodles for helping me survive grad life, especially those busy days towards the end. Many thanks to those ignorant of grad school etiquette, who kept pestering me with questions like "When are you planning to graduate?" and "When do you plan to defend your thesis?". These questions definitely kept reminding me that one day I have to finish what I am doing. On that note, thanks to www.Phdcomics.com for letting me know that there are many others sailing in the same boat. That was somehow a big relief.

Last but definitely not the least, I would like to express my deepest gratitude to my loving parents and my sister back home and my beloved wife, Vaishali, for their constant encouragement, love and motivation. It was only because of their belief in me that I could achieve whatever I have so far. I dedicate this dissertation to them.

Contents

List of Tables

List of Figures

Chapter 1

Introduction

Tissue engineering is an emerging technique to develop biological substitutes for replacing damaged tissues and organs. One of the main challenges in tissue engineering is that the biological materials that are conventionally used to engineer tissues are incapable of handling the physiological loading conditions in vivo or the mechanical stimuli during culture. There is a definite need to develop biological materials that have significant mechanical stability for use in tissue engineering. Nanotechnology seems to have an answer to resolve this issue through the provision of materials with exceptional mechanical properties.

This research focuses on the development of stronger biomaterials for tissue engineering applications using reinforcements in the form of carbon nanomaterials. Several structural, mechanical and biological constraints governing the choice of tissue engineering scaffold materials demand a careful investigation of the effects of the use of different types, concentrations and functionalizations of the carbon nanomaterials used as reinforcements. It is important, particularly, to study the effects of these variables on

essential tissue engineering scaffold properties such as biocompatibility and mechanical strength of the reinforced biomaterials.

In general, the conventional biomaterials used for tissue engineering qualify as soft materials. Mechanics of soft materials largely deals with understanding the large deformation mechanical response and developing constitutive material models of these materials based on deformation physics and underlying microstructure of the material. Computational models developed for these soft biomaterials facilitate the evaluation of the efficacy of the engineered construct as a substitute for the native tissue by simulating physiological loading conditions and analyzing its performance.

1.1 Tissue Engineering and Nanotechnology

1.1.1 Tissue Engineering and its Significance

Tissue engineering, as defined by Langer and Vacanti, is "an interdisciplinary field that applies the principles of engineering and life sciences toward the development of biological substitutes that restore, maintain, or improve tissue function or a whole organ" [49]. Approximately 8 million surgical procedures are performed annually in the United States alone due to tissue disease and organ failure. The costs of these procedures are of the order of billions of dollars a year.

Current therapies include: (a) autologous grafts (or autografts), in which tissue or an organ from another functionally less critical site in the same individual is used to replace the damaged tissue or organ; (b) allografts (or homografts), in which the graft is obtained from a donor of the same species as the recipient; (c) xenografts (or heterografts), in which the graft is obtained from a donor of different species than the recipient; and

(d) use of synthetic materials and bioceramics to replace the injured tissue or organ. These therapies have several limitations. For example, autografts are associated with the problem of creation of an additional injury, whereas allografts and xenografts run the risk of disease transmission, immune rejection and shortage of donors for a transplant. Synthetic materials on the other hand do not behave like true tissues and may lead to inflammation, fatigue, infection and problems with integration. Tissue engineering offers a better solution in these cases since it aims at developing biological substitutes in a natural way to restore, maintain and improve tissue function. These cell based substitutes provide immediate functionality and the capacity to integrate with surrounding host tissues.

Tissue is a combination of cells and an extracellular matrix. The extracellular matrix gives tissue its form and shape. Cell colonies need external cues in the form of mechanical, chemical, and electrical signals in order to grow into functional three-dimensional tissues and organs. Cells exist in a symbiotic relationship with the extracellular matrix, first creating it, then remodeling it, and in turn being regulated by it.

Fig. 1.1 shows a broad overview of tissue engineering. Isolated cells are combined

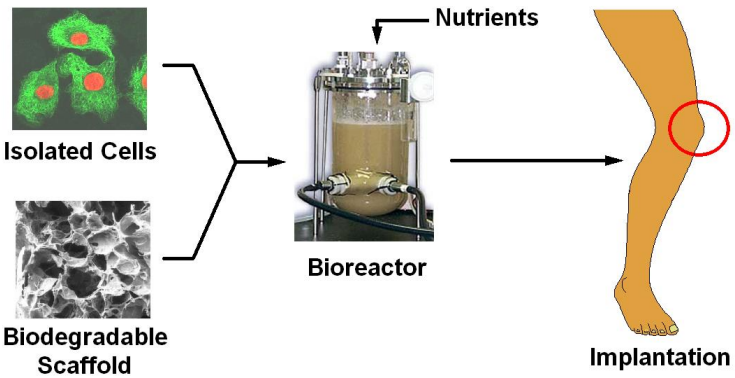

Figure 1.1: Overview of Tissue Engineering.

with a porous structure, a *scaffold*, which serves as a temporary matrix to hold the cells. These are then cultured in a bioreactor supplied with suitable nutrients, growth factors (protein molecules), and other chemical, electrical and mechanical stimuli to obtain engineered tissue which is then implanted into the body at the site of the injury.

1.1.2 Need for Novel Biomaterials for Tissue Engineering

Candidate biomaterials for tissue engineering scaffolds need to satisfy several requirements. From a mechanical point of view, the biomaterial should be as strong as the native tissue in order to handle physiological loading conditions [35, 81, 50, 92, 63]. Functional tissue engineering, however, aims at developing tissues that can withstand mechanical stimuli in culture and satisfy the functional needs of the target tissue [16]. Highly porous materials with a good surface chemistry are required in order to allow cell adhesion, proliferation and differentiation. These characteristics reduce the material's mechanical strength [103, 17]. The porous structure also needs to be interconnected and permeable to allow vascularization of the tissue, exchange of nutrients and disposal of waste. In addition to this, from a biological perspective, it should not adversely affect cell viability and function and it must eventually degrade safely and be replaced by cells' own extracellular matrix in a controlled fashion without losing mechanical stability or form. These severe constraints largely limit our choice of biomaterials and it is seldom possible to find a biocompatible and biodegradable material that can be processed using current techniques to form highly porous interconnected structures with sufficient mechanical strength.

Currently used biomaterials like collagen, agarose, polycaprolactone, fibrinogen, chitosan, among other biodegradable polymers, are a common choice for making tissue

engineering scaffolds. However, these materials are often found to be mechanically incapable of handling the physiological loading conditions in vivo or the mechanical stimuli during culture in a bioreactor. Various recent approaches such as alterations in the biomaterial composition and trying to improve the mechanical strength of polymers through cross-linking [83] have failed to produce biomaterials with sufficient mechanical strength at the required porosity [73, 39]. Thus, there is a definite need to develop mechanically stronger biomaterials for use in tissue engineering.

1.1.3 Carbon Nanomaterials as Reinforcement

Recent developments in the nanotechnology world seem to offer a promising solution. Carbon based nanomaterials (CNM), such as carbon nanotubes (CNT), single- (SWCNT) and multi-walled (MWCNT), and carbon nanofibers (CNF) are known to have exceptional mechanical and electrical properties [96, 29]. For example, the tensile strength of CNT is estimated to be about 200 GPa which is about 100 times that of steel (2 GPa) at one-sixth the weight. SWCNT have diameters ranging from 0.7 to 2.0 nm (typically around 1.0 nm), with lengths that are often hundreds or thousands of times greater than their diameter [4]. SWCNT also have remarkable flexural properties and an extremely high Young's modulus of 1 TPa along their axes [96, 20].

CNM have a huge potential for applications as additives in composite materials due to their exceptional mechanical properties. It has been found that with the addition of relatively very low concentrations of CNM, the mechanical [95, 45, 77, 93, 80, 10, 82, 74, 6, 19, 18, 46, 84], thermal [19, 18, 46], and electrical [60, 6, 104, 18] properties of polymer matrices can be improved considerably. Qian et al. [77] demonstrated that adding only 1% (by weight) of CNT to a polystyrene (PS) matrix, could increase the

stiffness of composites between 36% and 42% while increasing the tensile strength by about 25%.

Reinforcing materials for polymeric matrix systems such as SWCNT and MWCNT, as well as with CNF, have been shown in previous studies, to improve physical properties of the composite materials. These studies included SWCNT/polymethylmethacrylate (PMMA) [30], MWCNT/epoxy [80], CNF/polypropylene (PP) [52, 46], CNF/poly (phenylene sulfide) (PPS) [72], CNF/polystyrene [104], CNF/polycarbonate [19], CNF/epoxy [18], and CNF/ABS [84] composites. Initial studies using composites of CNT and synthetic polymers have shown that these materials can be used in neural and orthopedic tissue engineering applications. The reinforcement of naturally derived biopolymers with CNM is another promising area that is currently being explored. Wang et al. [100] demonstrated that addition of 0.8% MWCNTs almost doubles the tensile strength and Young's modulus of chitosan scaffolds. In another research, Yildirim et al. [105] showed that the addition of 1% SWCNTs to alginate scaffolds increased the tensile strength by about 24%.

CNM can be effectively used to reinforce polymer scaffolds only if the external loads can be efficiently transferred from the matrix to the nanomaterials [5]. CNM exist as agglomerated ropes of hundreds and thousands of nanotubes/nanofibers due to their strong inter-tube van der Waals and $pi - pi$ attraction (0.5 eV/nm). The mechanical properties of polymer nanocomposites largely depend on homogeneous dispersion of individual carbon nanotubes/nanofibers in the matrix since aggregated carbon nanotubes/nanofibers show different mechanical behaviour from individual carbon nanotubes/nanofibers [82, 96, 14]. However, their dispersion in the polymer is a considerable challenge. CNM functionalization and surfactant addition have been successfully

used for effective dispersion of the CNM in the polymer matrix [61, 83, 78]. Further, strong adhesion between the CNM and polymer matrix is essential to ensure good load transfer from the matrix to the CNM [96, 9]. This can also be controlled through the functionalization of CNMs.

1.1.4 Carbon Nanomaterials and Biocompatibility

Currently, the effects of CNMs on cell viability, proliferation and differentiation has not been studied in great detail. For applications in tissue engineering, biocompatibility of CNM is a primary consideration. Khan [44] used PLA (poly lactic acid) scaffolds reinforced with SWCNT for regenerating cartilage tissue and found the CNT had no hostile or debilitating effect on cells. Similarly, Webster et al. [102] found that the cellular response of neuronal and osteoblast cells to CNF-reinforced polycarbonate urethane composites was positive, suggesting that these composites have a good potential for neural and orthopedic applications. Because of their exceptional thermal and electrical conductivities, CNT have also been used by researchers to expose cells to electrical stimulation [91] and neuron growth using certain bioactive coatings [57]. Other studies, however, show that CNT can cause cytotoxicity in the short term (18 hour exposure) in vitro [85, 99, 34, 48, 101]. These effects may, however, be temporary with no differences observed in cell viability in the long term [53].

Currently, not much is known about the in vivo effects of CNT. Pure carbon is considered a harmless material, in general. But, there is little understanding about the effect of carbon nanostructures on cells [68]. The literature suggests that various factors like the method of preparation, type, functionalization and concentration of CNM may have an effect on cell viability. For example, Nimmagadda et al. [67] showed that SWCNT

functionalized with glucosamine have higher cell viability than purified SWCNT preparations at equivalent concentrations.

1.2 Computational Modeling of Soft Biomaterials

Functional tissue engineering aims at developing biological substitutes that are mechanically capable of handling the physiological loads and the mechanical stimulation during culture. It is of fundamental importance to have a better understanding of the loading environment within the construct and the effect of mechanical stimulation on the cells. In order to facilitate this, it is necessary to have robust computational models to describe the tissue/biomaterial.

1.2.1 Biphasic Behaviour of Soft Porous Biomaterials

Most biomaterials used in tissue engineering applications and connective tissues like cartilage, interveterbral disks, cornea, etc., may be different morphologically but they share many similarities in terms of their basic structural components. These are highly heterogeneous structures with a solid matrix, which may be composed of different components forming a porous network, and a high concentration of fluids. In order to obtain an accurate model for the mixture, it is neccessary to account for the different constituents in the model. Such models are called multiphasic models. It is often very difficult to account for each and every component separately in the solid phase and hence the solid phase is assumed to consist of a single homogeneous constituent. Thus, the overall mixture is assumed to consist of one homogeneous solid phase and a fluid phase. Such materials are classified as biphasic materials.

In biphasic materials the solid matrix is permeable to fluid flow and any volumetric deformation of the solid causes flow of fluid into or out of the solid matrix. In general, the permeability of the solid matrix is very low. For example, for articular cartilage it is of the order of 10^{-13} to 10^{-16}m^4/Ns [56, 65]. This low permeability causes the fluid to exert a huge frictional drag on the solid as it flows through the pores. This drag force is significant due to the low elastic moduli (0.01 to 10 MPa) [65] of these porous solids and causes the mixture to exhibit a viscoelastic response. The biphasic mixture displays phenomena like creep and stress relaxation which are characteristics of viscoelastic materials.

When biphasic materials are subjected to sudden compressive loads, most of the load is instantaneously carried by the fluid which is pressurized since it is trapped inside the pores. This explains how the weak solid matrix is capable of supporting large loads. Fluid pressurization shields the solid matrix and also protects the cells living in such tissues from large deviatoric stresses. The porous solid matrix is capable of undergoing large strains of about 50% to 80% before failure. This is due to compaction of the solid matrix and fluid exudation.

1.2.2 Trends in Continuum Mechanics of Porous Media

Since it is extremely difficult to describe the exact location of the pores (either empty or filled with fluid) and the solid material in a biphasic material, the heterogeneous composition is generally investigated using a volume fraction concept wherein the solid and fluid phases are assumed to be smeared throughout the volume occupied by the porous solid such that every point in the volume consists of both solid and fluid phases and these smeared continua thus have reduced densities compared to the original consituents. As

a consequence, mathematical functions describing both geometrical and physical properties of each constituent are field functions defined over the domain of interest.

Although the biphasic approach has been applied successfully to model various tissues such as the meniscus [89], mandibular joints [27], flexor digitorum profundus tendons [31], arterial walls, heart walls, skin and hydrogels [36], it was primarily developed to model articular cartilage. This theory has been successfully used to describe the deformation and stress fields under a variety of loading configurations [86, 66, 54, 64, 7, 87]. This has been possible due to the similarities in the deformational behavior of many soft porous-permeable biomaterials and a variety of tissues.

Preliminary Models

Preliminary models used to describe biphasic materials used a single phase description to explain the combined behaviour of the fluid-solid mixture. Hayes et al. [33] described the articular cartilage as a linearly elastic solid and determined its elastic shear modulus using indentation tests. Kempson et al. [43] used a single phase viscoelastic model to describe the creep experiments performed on articular cartilage. This kind of single-phase description of the biphasic mixture can only be used to describe the behavior in a single mode of deformation at most with limited accuracy. In order to describe the behavior of the mixture accurately it is necessary to account for the different constituents of the mixture.

Linear and Nonlinear Biphasic Theory

The theory of porous media has a long tradition (see [21, 22]). Bowen used the theory of mixtures restricted by the volume fraction concept in order to treat incompressible [12]

and compressible [13] porous media. Mow et al. [66] published a paper independently, similar to Bowen's [12] approach. They developed an incompressible binary mixture model which was mainly concerned with biomechanical problems. In this simplified model, the solid phase was assumed to be isotropic and linearly elastic and the interstitial fluid was assumed to be incompressible and inviscid. This model identified the aggregate modulus, Poisson's ratio and the permeability as the three material constants for a linearly biphasic material. The permeability of the tissue was assumed to be constant in the linear biphasic theory.

There were several shortcomings to the linear biphasic model. The permeability of the material is expected to change as it is deformed. In 1976, Mansour and Mow [55] found that higher strains caused the permeability to decrease exponentially with increase in strain. This phenomenon was incorporated in the biphasic model by Lai and Mow in 1980 [47] by introducing the concept of exponential strain dependent permeability. This theory was validated by Mow et al. for various loading configurations such as indentation [54, 64], and confined and unconfined compression [66, 7].

The linear biphasic theory could not fairly predict material behavior for physiological loading conditions and large deformations. Holmes and Mow [37] proposed a finite deformation biphasic model for hydrated connective tissues and soft gels. They used an exponential hyperelastic constitutive relationship between stress and strain in order to provide a nonlinear description of the solid phase. This model was capable of handling physiological loads and large deformations. It provided a realistic fluid phase constitutive description by including strain-dependent permeability which was absent in the linear biphasic models.

1.2.3 Biphasic Material Models for Agarose

The biomaterial used for making the nanocomposite scaffolds in this research is *agarose*. Agarose is a hydrogel which consists of a highly porous solid matrix that can readily absorb and hold fluid. Agarose has been used in tissue engineering as a scaffold material because it is biocompatible and offers a great substrate for cell attachment, cell differentiation and proliferation [59, 8, 15, 42]. In the context of tissue engineering, it is known that mechanical stimulation can be successfully used to alter the properties of the engineered tissue by controlling the phenotypic expression of the cells within the construct [58]. It has been shown that dynamic compression of cell-seeded gel constructs at certain frequencies and amplitudes stimulates the synthesis of matrix constituents like proteoglycans and proteins [79]. This has a significant effect on the mechanical properties of the construct. For example, it was shown by Mauck et al. [59] that the equilibrium aggregate modulus of cell-seeded disks of agarose subjected to dynamic loading increased by about six times compared to that of free swelling controls after 28 days of loading. In order to better understand the mechanical stimulation and the loading environment within the construct to which the cells are subjected and to be able to compare the mechanical properties of various constructs, it is necessary to have a realistic constitutive model for agarose and a standard way to mechanically characterize these materials.

Tissue engineers have been interested in the material properties of agarose because the success of a tissue engineered construct depends on its ability to mimic the native tissue [42]. Agarose has been modeled as a biphasic material with linearly elastic solid in the literature [15, 51, 59]. Thus, it has been described using its aggregate modulus, Poisson's ratio and permeability to assess its efficacy as a tissue engineering construct. However, when the permeability of the gel from the linear biphasic theory, as proposed

by Mauck [59] for small deformations, was compared with results obtained from direct permeation experiments [88], a huge discrepancy was observed between the two results. This indicated that the linear biphasic theory is inefficient when it comes to predicting agarose response in compression.

Thus, there is a need to model such soft biomaterials and hydrogels using the nonlinear biphasic model as proposed by Holmes and Mow [37] with strain-dependent permeability. It is also known that under high physiological loads these biomaterials undergo finite deformations. The nonlinear biphasic theory supports large deformations. The exponential constitutive relationship for the solid phase used by Holmes and Mow was shown to be appropriate for modeling bovine articular cartilage. However, such a description cannot be generalized for all biphasic materials, although there is a lot of similarity in the structural composition. This is because the constitutive description of the solid phase at equilibrium is largely governed by the microscale properties of the materials. To our knowledge, the nonlinear biphasic behavior of agarose and its nanocomposites for finite strains has not been studied till date.

1.3 Research Objectives

The overall goal of this dissertation is to develop novel carbon nanomaterial-reinforced biomaterial composites with enhanced material properties for use in tissue engineering. This research has two broad aspects. The first deals with application of nanotechnology to tissue engineering in order to develop better scaffold materials and the second focuses on the mechanical characterization and computational modeling of soft porous biomaterials and their composites as biphasic materials. The specific objectives of the

two aspects of this research are as listed here.

In order to assess the application of agarose and its nanocomposites as tissue engineering scaffolds, we need to accomplish the following objectives.

1. Determine the effect of carbon nanomaterial concentration on
   (a) the mechanical properties of the agarose nanocomposite.
   (b) the biocompatibility of the agarose nanocomposite.
2. Determine the type and functionalization of carbon nanomaterials that most improves the mechanical integrity without compromising biocompatibility.

In the context of computational modeling and mechanical characterization of agarose and its nanocomposites, the following objectives need to be accomplished.

1. Develop a standard method to numerically characterize agarose and its nanocomposites.
2. Develop a macro-scale material model for agarose and its nanocomposites based on nonlinear biphasic theory that describes their equilibrium and transient behavior.

1.4 Outline of the Dissertation

The rest of the dissertation is organized as follows. In Chapter 2, we lay down the basic fundamentals of the numerical modeling of soft biomaterials using the biphasic theory. The equations of motion are laid down and the constitutive relations for the solid and the permeability are discussed. The equations of motion along with constitutive relations completely define the problem of modeling the biphasic system and are specialized for

the uniaxial deformation problem.

In Chapter 3, we discuss the materials used for making the constructs for this research. We lay down the test plan summary for the experiments performed for determining the effect of concentration, type and functionalization of the carbon nanomaterials on the mechanical properties and biocompatibility of agarose. We discuss in detail, the experimental protocol for biocompatibility and mechanical testing used to assess the nanocomposites for use in tissue engineering. Following this we discuss the data analysis techniques used to post-process experimental data from the mechanical tests in order to obtain the material parameters for the solid and the fluid phase.

In Chapter 4, we present the results obtained for various tests performed during this research. The results of the mechanical tests are postprocessed to obtain the definitions of the constitutive relationships for the solid and the permeability in order to develop a complete robust computational model for the biphasic system.

Finally, in Chapter 5, we provide some concluding remarks with suggestions for future work in this research.

Chapter 2

Computational Modeling of Soft Biomaterials as Biphasic Materials

As discussed in the previous chapter, most soft hydrated biomaterials and tissues can be treated as biphasic materials consisting of a solid phase and a fluid phase. The simplest example of a biphasic system is a sponge filled with water. In this chapter, we will discuss the balance laws and equations of motion for a biphasic material. Each phase has mass and a displacement field associated with it. Hence, we can apply balance laws for mass momentum and energy for both phases. These equations are not very different from those for a single phase system. However, it is important to account for the interactions between the two phases when considering a biphasic system. These are accounted for by introducing additional *interaction terms* in the balance equations.

Once the balance laws are discussed and equations of motion are formulated for both phases, the next step is to develop constitutive relationships for the fluid and solid phases in order to be able to solve the equations of motion. These constitutive relations

are discussed for the linear and nonlinear biphasic theory. This is followed by the development of specialized governing equations for uniaxial problems.

As discussed in the previous chapter, the biphasic theory uses a binary mixture approach to solve biomechanical problems. It uses the theory of mixtures restricted by the volume fraction concept. The mixture theory is based on certain assumptions, three of which are of particular interest and are discussed below [36].

Properties of the Mixture: The properties of the mixture should be mathematical consequences of the properties of the individual constituents forming the mixture [97]. Thus, the balance laws for for the mixture should be deduced from the balance laws of the individual constituents.

Principle of Mixture: The equations of motion of the mixture are the same as those of the constituents, provided that the interactions between the constituents are accounted for.

Principle of Phase Reduction: The equations of motion for the mixture should reduce to those for a single phase system if the volume fractions corresponding to the remaining phases are set to zero.

2.1 Mixture Theory

Before we discuss the equations of motion for the constituents of the biphasic material, it is important to discuss the concept of volume fractions. According to the mixture theory, the geometrical interpretation of the porestructure and the exact location of the individual constituents are ignored and it is assumed that the pores are statistically

distributed and that an arbitrary volume element in the material is composed of volume elements of the real constituents. In order words, each spatial point in the mixture is assumed to be simultaneously occupied by a material point of each constituent. This concept gives rise to substitute continuum descriptions for the solid and fluid phases with reduced densities by assuming that the constituent phases are "smeared" throughout the mixture volume. Thus, for the α phase, the spatial coordinate $\mathbf{x}^\alpha$ of the material point $\mathbf{X}^\alpha$ is defined as

$$\mathbf{x}^\alpha = \mathbf{x}^\alpha(\mathbf{X}^\alpha, t). \tag{2.1}$$

Thus, for each spatial point in the mixture, $\mathbf{x}$, each constituent has a material point $\mathbf{X}^\alpha$ such that $\mathbf{x} = \mathbf{x}^\alpha(\mathbf{X}^\alpha, t)$. The mass density of the constituents can be defined in two ways; one based on the volume occupied by the constituent alone and one based on the volume occupied by the mixture as follows [36].

$$\begin{aligned}
\rho^\alpha(\mathbf{x}, t) &= \frac{\mathrm{dm}}{\mathrm{d}V} && \text{is the mass density based on the mixture volume } (V) \text{ known as} \\
& && \text{the bulk or partial density, and} \\
\rho^\alpha_T(\mathbf{x}, t) &= \frac{\mathrm{dm}}{\mathrm{d}V^\alpha} && \text{is the mass density based on the volume occupied by the} \\
& && \text{constituent } \alpha(V^\alpha), \text{ known as the intrinsic or material density.}
\end{aligned} \tag{2.2}$$

The volume fraction of the α constituent is defined as the volume of the α phase per unit volume of the mixture,

$$\phi^\alpha = \frac{\mathrm{d}V^\alpha}{\mathrm{d}V}. \tag{2.3}$$

This gives us a relationship between the two densities as

$$\rho^\alpha = \phi^\alpha \rho^\alpha_T. \tag{2.4}$$

The equations of motion are written in terms of the partial densities ρ^α.

2.2 Equations of Motion

In this section, we will discuss the balance laws for mass, momentum and energy applied to biphasic materials. Equations can be written for each phase separately and for the mixture as a whole. It is important to account for the interaction terms between the two phases in the individual phase equations.

For a single-phase material the balance of mass, momentum and energy can be formulated as [40]

$$\frac{\partial \rho}{\partial t} + \rho \nabla \cdot \mathbf{v} = 0, \tag{2.5}$$

$$\nabla \cdot \boldsymbol{\sigma} + \rho \mathbf{b} = \rho \mathbf{a}, \tag{2.6}$$

$$\rho \frac{\partial \epsilon}{\partial t} = \boldsymbol{\sigma} : \mathbf{D} - \nabla \cdot \mathbf{q} + \rho g. \tag{2.7}$$

Here ρ is the density of the material, t is the time, $\mathbf{v}$ is the velocity field, $\boldsymbol{\sigma}$ is the Cauchy stress tensor, $\mathbf{b}$ is the body force vector, $\mathbf{a}$ is the acceleration, ϵ is the internal energy density, $\mathbf{D}$ is the symmetric part of the velocity gradient, $\mathbf{q}$ is the spatial heat flux, and g is the heat supply density.

This can be extended to individual constituents in a multiphasic system by including the interaction terms as follows.

$$\frac{\partial^\alpha \rho^\alpha}{\partial t} + \rho^\alpha \nabla \cdot \mathbf{v}^\alpha = m^\alpha, \tag{2.8}$$

$$\nabla \cdot \boldsymbol{\sigma}^\alpha + \rho^\alpha \mathbf{b}^\alpha = \rho^\alpha \mathbf{a}^\alpha + \boldsymbol{\pi}^\alpha, \tag{2.9}$$

$$\rho^\alpha \frac{\partial \epsilon^\alpha}{\partial t} = \boldsymbol{\sigma}^\alpha : \mathbf{D}^\alpha - \nabla \cdot \mathbf{q}^\alpha + \rho^\alpha g^\alpha + E^\alpha, \tag{2.10}$$

where α denotes the individual phase for which the equations are written and m^α, $\boldsymbol{\pi}^\alpha$ and E^α are the interaction terms for mass, momentum and energy between the α phase and the remaining phases in the mixture. The biphasic theory deals with only two phases, namely the solid and the fluid phases. These phases will be denoted by superscripts s and f.

Assuming that there is no interchange of mass between the solid and the fluid phases, the continuity or the mass balance equations for a biphasic material can be written as,

$$\frac{\partial \rho^s}{\partial t} + \nabla \cdot (\rho^s \mathbf{v}^s) = 0, \tag{2.11}$$

$$\frac{\partial \rho^f}{\partial t} + \nabla \cdot (\rho^f \mathbf{v}^f) = 0. \tag{2.12}$$

Here ρ^s and ρ^f are the partial densities of the solid and fluid phases respectively and $\mathbf{v}^s$ and $\mathbf{v}^f$ are their respective velocities.

Assuming that each constituent is incompressible, the intrinsic density of the material remains constant. It can be easily derived that for a fully saturated biphasic material,

$$\phi^f + \phi^s = 1. \tag{2.13}$$

Here ϕ^f and ϕ^s are the fluid and solid volume fractions respectively. Thus, we can use equation (2.4) in the continuity equations (2.11 and 2.12) for the individual phases and add the equations to obtain

$$\nabla \cdot (\phi^f \mathbf{v}^f + \phi^s \mathbf{v}^s) = 0. \tag{2.14}$$

Now consider the linear momentum balance equations. For a quasi-static problem, the acceleration $\mathbf{a}^\alpha$ can be neglected. Also if we assume that the body forces $\mathbf{b}^\alpha$ are absent, we can write the momentum equations as

$$\nabla \cdot \boldsymbol{\sigma}^s + \boldsymbol{\pi}^s = 0, \tag{2.15}$$

$$\nabla \cdot \boldsymbol{\sigma}^f + \boldsymbol{\pi}^f = 0. \tag{2.16}$$

Here $\boldsymbol{\sigma}^s$ and $\boldsymbol{\sigma}^f$ are the Cauchy stress tensors based on the mixture area, and $\boldsymbol{\pi}^s$ and $\boldsymbol{\pi}^f$ are the body forces that arise due to transfer of momentum between the two phases. According to Newton's third law of motion, these body forces are equal and opposite at each point in the mixture. Hence,

$$\boldsymbol{\pi}^s = -\boldsymbol{\pi}^f = \boldsymbol{\pi} \tag{2.17}$$

Similarly, ignoring the heat flux $\mathbf{q}$ and the heat supply density g, the energy balance equations can be written as

$$\rho^s \frac{\partial \epsilon^s}{\partial t} = \boldsymbol{\sigma}^s : \mathbf{D}^s + E^s, \tag{2.18}$$

$$\rho^f \frac{\partial \epsilon^f}{\partial t} = \boldsymbol{\sigma}^f : \mathbf{D}^f + E^f, \tag{2.19}$$

Additionally, it can be proved using the law of conservation of angular momentum that the stress tensor for the mixture as a whole is symmetric but the stress tensors for each constituent may not be symmetric [36]. They are symmetric if the moment of momentum supply terms to those phases are zero.

The Cauchy stress tensors for the fluid and the solid phases can be obtained from the

balance equations and the Clausius-Duhem entropy inequality as (see [36] for a detailed derivation)

$$\boldsymbol{\sigma}^s = -\phi^s p\mathbf{I} + \boldsymbol{\sigma}^e \text{ and} \tag{2.20}$$

$$\boldsymbol{\sigma}^f = -\phi^f p\mathbf{I}. \tag{2.21}$$

Here $\boldsymbol{\sigma}^e$ is the elastic stress tensor for the solid phase, $\mathbf{I}$ is the identity tensor and p is the pressure term that has to be incorporated due to the incompressibility of the phases. Having developed the equations of motion we will now look at the constitutive relationships for each of the two phases. These equations will be used to define the momentum supply term $\boldsymbol{\pi}$ in the momentum balance equations (2.15 and 2.16) and the elastic stress tensor $\boldsymbol{\sigma}^e$ in the solid stress equation (2.20).

2.3 Constitutive Equations for Biphasic Materials

Constitutive equations are developed for the elastic stress tensor $\boldsymbol{\sigma}^e$ for the solid phase and the momentum supply term $\boldsymbol{\pi}$ for the interactions between the solid and the fluid phases. It is important to note that even though there is an interaction between the solid and the fluid phases, constitutive relationships for both phases can be developed independently. However, the constraints applied to the motion of a single phase material apply to each constituent of the mixture. According to Passmann and Nunziato's [71] principle of phase separation, in a multiphase mixture where the constituents are physically separated, the material specific dependent variables of a given phase, for example, the stress and the Helmholtz free energy density depend only on the independent variables of that phase, whereas the interaction terms, like the momentum transfer term, $\boldsymbol{\pi}$,

depend on all the independent variables.

2.3.1 Solid Phase Constitutive Description

The solid phase can be described as a linearly elastic solid for small strains. For large strains, however, the solid phase constitutive description should account for material and geometrical nonlinearity. In addition to this, the constitutive behavior may also need to be adapted to isotropic, transversely isotropic or anisotropic behaviors. We will restrict our discussion to isotropic solids.

Linearly Elastic Solid

In the linear biphasic theory, the solid phase is described as a linearly elastic material with

$$\boldsymbol{\sigma}^e = \lambda^s \mathrm{tr}(\mathbf{e}^s)\mathbf{I} + 2\mu^s \mathbf{e}^s, \tag{2.22}$$

where, $\mathbf{e}^s$ is the strain tensor for small deformations, $\mathbf{I}$ is the identity tensor and λ^s, μ^s are the Lamé parameters. The strain tensor, $\mathbf{e}^s$, is written in terms of the displacement field $\mathbf{u}^s$ as follows

$$\mathbf{e}^s = \frac{1}{2}\left[\nabla \mathbf{u}^s + (\nabla \mathbf{u}^s)^T\right]. \tag{2.23}$$

Substituting $\boldsymbol{\sigma}^e$ from equation (2.22) in equation (2.20), we obtain the solid phase stress as

$$\boldsymbol{\sigma}^s = -\phi^s p\mathbf{I} + \lambda^s \mathrm{tr}(\mathbf{e}^s)\mathbf{I} + 2\mu^s \mathbf{e}^s \tag{2.24}$$

This describes the constitutive relationship for a linearly elastic isotropic solid phase for the biphasic material.

Nonlinearly Elastic Solid

Given the fact that most hydrated tissues are subjected to large strains in vivo, it is necessary to have a constitutive law for the solid phase that can handle finite deformations. In fact the most significant part of modeling a biphasic material for finite deformation is to find a constitutive relationship for the solid phase elastic stress and the permeability. It is known from the literature that the stress-strain relationship for the solid phase of these biphasic materials is highly nonlinear at large strains [37]. The goal, thus, is to determine a strain energy function, ψ^s, that best describes the nonlinear stress-strain relationship. In this research we will use a compressible nonlinear hyperelastic description for the solid phase. Various forms of the strain energy function [38] can be used to describe such a behavior, namely the Neo-Hookean model, the Mooney-Rivlin model, the Polynomial model, the exponential model, etc. We consider a special form of the strain energy density function called the Ogden-Hill strain energy potential, that is based on the principal stretches and is typically used to model foam-like or elastomeric materials. Before we discuss the specific form of the strain energy potential, it is important to have a brief overview of continuum mechanics applied to biphasic materials. Let Ω denote the current configuration of the biphasic mixture at time t and Ω_0^s and Ω_0^f denote the initial or reference configuration for the solid and fluid phases. As discussed earlier, for each spatial point in the mixture, $\mathbf{x}$, there is a material point $\mathbf{X}^\alpha$, $(\alpha = s, f)$ such that,

$$\mathbf{x} = \mathbf{x}^\alpha(\mathbf{X}^\alpha, t). \tag{2.25}$$

The superscript α is dropped in the further discussion for clarity. The deformation gradient associated with the associated with the motion of each phase is defined as

$$\mathbf{F} = \frac{\partial \mathbf{x}}{\partial \mathbf{X}} \tag{2.26}$$

The right and left Cauchy-Green deformation tensors are defined as

$$\mathbf{C} = \mathbf{F}^T\mathbf{F} \text{ and} \tag{2.27}$$

$$\mathbf{B} = \mathbf{F}\mathbf{F}^T \tag{2.28}$$

respectively. For an isotropic solid, it is also important to introduce the principal invariants of the Cauchy-Green deformation tensors. These are equal for $\mathbf{C}$ and $\mathbf{B}$ and are defined as follows.

$$I_1 = \text{tr}(\mathbf{C}), \tag{2.29}$$

$$I_2 = \frac{1}{2}\left[I_1^2 - \text{tr}(\mathbf{C}^2)\right], \text{ and} \tag{2.30}$$

$$I_3 = \det(\mathbf{C}). \tag{2.31}$$

The eigenvalues of the Cauchy-Green deformation tensors are the squares of the principal stretches λ_1, λ_2 and λ_3. The strain energy density function for the isotropic solid phase can be defined as a function of the Cauchy strain tensors, strain invariants or the principal stretches as,

$$\psi^s = \psi^s(\mathbf{C}) = \psi^s(\mathbf{B}) = \psi^s(I_1, I_2, I_3) = \psi^s(\lambda_1, \lambda_2, \lambda_3). \tag{2.32}$$

Accordingly, the elastic Cauchy stress for the solid phase, defined as

$$\boldsymbol{\sigma}^e = \frac{2}{J}\mathbf{F}\frac{\partial \psi^s}{\partial \mathbf{C}}\mathbf{F}^T, \tag{2.33}$$

can be obtained from the strain energy density definitions in terms of the invariants or in terms of the principal stretches. Here J is the determinant of the deformation gradient and is a measure of the volumetric change. Thus,

$$\boldsymbol{\sigma}^e = \frac{2}{J}(c_1\mathbf{B} + c_2\mathbf{B}^2 + c_3\mathbf{B}^3) \quad \text{or,} \tag{2.34}$$

$$\sigma_i^e = \frac{1}{J}\lambda_i\frac{\partial \psi^s}{\partial \lambda_i} \tag{2.35}$$

where σ_i^e are the principal stress components of the elastic stress tensor for the solid and

$$c_1 = \frac{\partial \psi^s}{\partial I_1} + I_1\frac{\partial \psi^s}{\partial I_2} + I_2\frac{\partial \psi^s}{\partial I_3}, \tag{2.36}$$

$$c_2 = -\frac{\partial \psi^s}{\partial I_2} - I_1\frac{\partial \psi^s}{\partial I_3}, \text{ and} \tag{2.37}$$

$$c_3 = \frac{\partial \psi^s}{\partial I_3}. \tag{2.38}$$

It is convenient to have a strain energy density function that is defined using the principal stretches rather than using the principal invariants since stretches are obtained easily from experiments.

The strain energy density function that will be considered here, called the Ogden-Hill strain energy potential, is defined using the principal stretches. It is used to model the material as a compressible isotropic hyperelastic material during the loading phase and

is defined as

$$\psi^s = \sum_{i=1}^{N} \frac{2\mu_i}{\alpha_i^2} \left[\lambda_1^{\alpha_i} + \lambda_2^{\alpha_i} + \lambda_3^{\alpha_i} - 3 + \frac{1}{\beta_i} \left(J^{-\alpha_i \beta_i} - 1 \right) \right]. \tag{2.39}$$

Here, μ_i, α_i and β_i are the unknown material parameters. The solid phase is completely defined by these three parameters. Although, the parameters may not have direct physical significance, other quantities of physical significance obtained using these parameters are as follows. Poisson's ratio ν_i is related to the parameters β_i as

$$\nu_i = \frac{\beta_i}{1 + 2\beta_i}. \tag{2.40}$$

The initial shear modulus μ_0 is defined as

$$\mu_0 = \sum_{i=1}^{N} \mu_i \tag{2.41}$$

and the initial bulk modulus κ_0 is defined as

$$\kappa_0 = \sum_{i=1}^{N} 2\mu_i \left(\frac{1}{3} + \beta_i \right) \tag{2.42}$$

The Cauchy stress σ_j^e and the nominal stress T_j are obtained from this definition of the strain energy density function as follows

$$\sigma_j^e = \frac{1}{J} \lambda_j \frac{\partial \psi^s}{\partial \lambda_j} = \frac{2}{J} \sum_{i=1}^{N} \frac{\mu_i}{\alpha_i} \left(\lambda_j^{\alpha_i} - J^{-\alpha_i \beta_i} \right) \text{ and} \tag{2.43}$$

$$T_j = \frac{\partial \psi^s}{\partial \lambda_j} = \frac{2}{\lambda_j} \sum_{i=1}^{N} \frac{\mu_i}{\alpha_i} \left(\lambda_j^{\alpha_i} - J^{-\alpha_i \beta_i} \right). \tag{2.44}$$

Pseudo-Elasticity for the Solid Phase

Our experiments indicate that the candidate biomaterial used for this research (agarose) displays a marked stress-softening response during unloading after loading, i.e., the stress in the material during the unloading is significantly less than the stress during the loading for the same deformation. This is represented in Fig. 2.1. This hysteretic response is

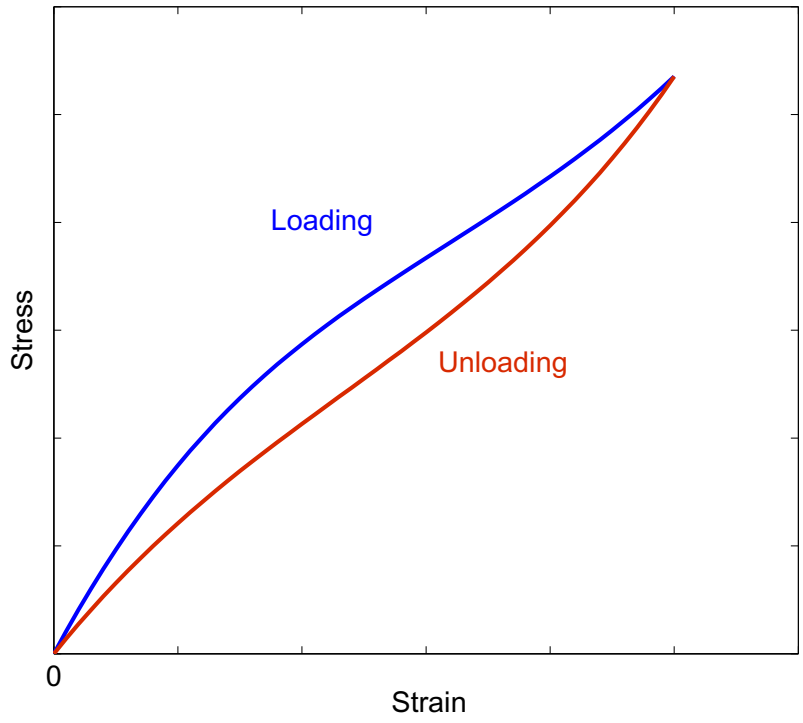

Figure 2.1: Typical stress-strain behavior for a material with a pseudoelastic response (Part C).

observed in a quasistatic loading-unloading process and hence does not involve any time (or rate) dependent effects. Also, the Mullin's effect is ruled out in this case because the specimens are preconditioned up to the maximum strain before testing.

The hysteretic response of the material is presumably due to dissipation of energy associ-

ated with recoverable damage. Such a behavior cannot be modeled using hyperelasticity. The pseudo-elastic model developed by Dorfmann and Ogden [28] for modeling similar behavior in particle-filled rubber is adapted here and is described below.

The strain energy density function for the solid phase ψ^s is modified by incorporating an additional variable η into its definition. Thus,

$$\psi^s = \psi^s(\lambda_1, \lambda_2, \lambda_3, \eta). \tag{2.45}$$

The parameter η allows us to change the form of the strain energy density function according to the deformation process. With this new definition of the strain energy density function, the material can no longer be considered elastic and the function $\psi^s(\lambda_1, \lambda_2, \lambda_3, \eta)$ is referred to as a pseudo-energy function.

The variable η is defined such that it has a constant value during loading and its value keeps changing during unloading. This behavior needs to be incorporated in the definition of η. Setting the constant value of η to unity during loading, we get

$$\psi_0^s(\lambda_1, \lambda_2, \lambda_3) = \psi^s(\lambda_1, \lambda_2, \lambda_3, 1), \tag{2.46}$$

which defines ψ_0^s as the value of the pseudo-energy density function during loading. We obtain the corresponding Cauchy stress and nominal stress as

$$\sigma_{0j}^e = \frac{1}{J}\lambda_j \frac{\partial \psi_0^s}{\partial \lambda_j} \quad \text{and} \tag{2.47}$$

$$T_{0j} = \frac{\partial \psi_0^s}{\partial \lambda_j}, \tag{2.48}$$

respectively.

The definition of the strain energy density function in equation (2.45) is subject to the following constraint [70, 28]

$$\frac{\partial \psi^s}{\partial \eta}(\lambda_1, \lambda_2, \lambda_3, \eta) = 0, \tag{2.49}$$

which implicitly defines η uniquely in terms of λ_i. Thus, we can write the solution of the form $\eta = \eta_e(\lambda_1, \lambda_2, \lambda_3)$. Using this we can define the resulting unique strain energy density function as

$$\hat{\psi}^s(\lambda_1, \lambda_2, \lambda_3) = \psi^s(\lambda_1, \lambda_2, \lambda_3, \eta(\lambda_1, \lambda_2, \lambda_3)). \tag{2.50}$$

Following [28], we define the strain energy density function to have the form,

$$\psi^s(\lambda_1, \lambda_2, \lambda_3, \eta) = \eta \psi_0^s(\lambda_1, \lambda_2, \lambda_3) + \phi(\eta), \;\; \phi(1) = 0. \tag{2.51}$$

This reduces to equation (2.46) for $\eta = 1$ during loading. The function $\phi(\eta)$ represents the energy dissipation and is discussed in detail later in this section.

The resulting Cauchy and nominal stresses are defined as

$$\sigma_j^e = \eta \frac{1}{J} \lambda_j \frac{\partial \psi_0^s}{\partial \lambda_j} \;\; \text{and} \tag{2.52}$$

$$T_j = \eta \frac{\partial \psi_0^s}{\partial \lambda_j}. \tag{2.53}$$

Comparing these with equations (2.47) and (2.48), we get

$$\sigma_j^e = \eta \sigma_{0j}^e \;\; \text{and} \tag{2.54}$$

$$T_j = \eta T_{0j}. \tag{2.55}$$

That is, the stresses in general are equal to the stresses in the undamaged material but scaled by the factor η. These equations hold during loading and unloading. During loading, $\eta = 1$ and the Cauchy and the nominal stresses are simply given by σ^e_{0j} and T_{0j} respectively and during unloading, the stresses are $\eta\sigma^e_{0j}$ and ηT_{0j} respectively. Thus, the new pseudo-energy function allows us to obtain the stress due to softening by scaling the stress without softening (i.e. during loading) by a variable factor η.

It is clear that the variable $\eta \leq 1$. During loading and at the beginning of unloading, $\eta = 1$ and it decreases as the unloading progresses.

We now look at the function $\phi(\eta)$. Differentiating equation (2.51) with respect to η and using equation (2.49), we obtain

$$\phi'(\eta) = -\psi^s_0(\lambda_1, \lambda_2, \lambda_3). \tag{2.56}$$

Thus, $\phi'(\eta)$ is directly related to the energy stored due to the deformation of the material. At the beginning of unloading when $\eta = 1$, $\phi'(\eta)$ is equal to the negative of the maximum value attained by the strain energy, which we denote by ψ^s_{max}, i.e., $\phi'(1) = -\psi^s_{max}$.

When the material is fully unloaded, with $\lambda_i = 1$, η attains a minimum value, denoted by η_{min}, where we have $\phi'(\eta_{min}) = -\psi^s_0(1, 1, 1) = 0$.

At the end of the unloading, the pseudo-energy function given in equation (2.51) has a residual value given by $\psi^s(1, 1, 1, \eta_{min}) = \phi(\eta_{min})$. This is the non-recoverable residual energy that is dissipated through the loading-unloading cycle. Thus, we can refer to $\phi(\eta)$ as the dissipation function.

Following [28], we choose the following form for the dissipation function ϕ

$$\phi'(\eta) = -m \tanh^{-1}\left[r(\eta - 1)\right] - \psi^s_{max}. \tag{2.57}$$

Here r and m are positive material parameters to be determined from experiments. The parameter r is dimensionless and m has the same units as the shear modulus, i.e., MPa. Using equations (2.56) and (2.57), we obtain,

$$\eta = 1 - \frac{1}{r} \tanh\left[\frac{\psi^s_{max} - \psi^s_0(\lambda_1, \lambda_2, \lambda_3)}{m}\right]. \tag{2.58}$$

During loading, the value of ψ^s_{max} is continuously updated to $\psi^s_0(\lambda_1, \lambda_2, \lambda_3)$ as the material deforms and hence $\eta = 1$. During unloading, η decreases continuously and at the end of unloading reaches a η_{min} given by

$$\eta_{min} = 1 - \frac{1}{r} \tanh\left[\frac{\psi^s_{max}}{m}\right]. \tag{2.59}$$

Fig. 2.2 shows a plot of the η function with respect to strain for r = 6.08E-03 and m = 3.89E-01. The specimen is loaded upto 50% strain and is unloaded back to zero strain configuration. Equation (2.57) can be integrated to obtain

$$\phi(\eta) = -m(\eta - 1) \tanh^{-1}\left[r(\eta - 1)\right] - \psi^s_{max}(\eta - 1) - \frac{m}{2r} \log\left[1 - r^2(\eta - 1)^2\right] \tag{2.60}$$

During loading, the strain energy density function is given by $\psi^s_0(\lambda_1, \lambda_2, \lambda_3)$. We define this as the Ogden-Hill strain energy potential given by equation (2.39). Thus, the loading part of the stress-strain curve follows the hyperelastic material behavior. The

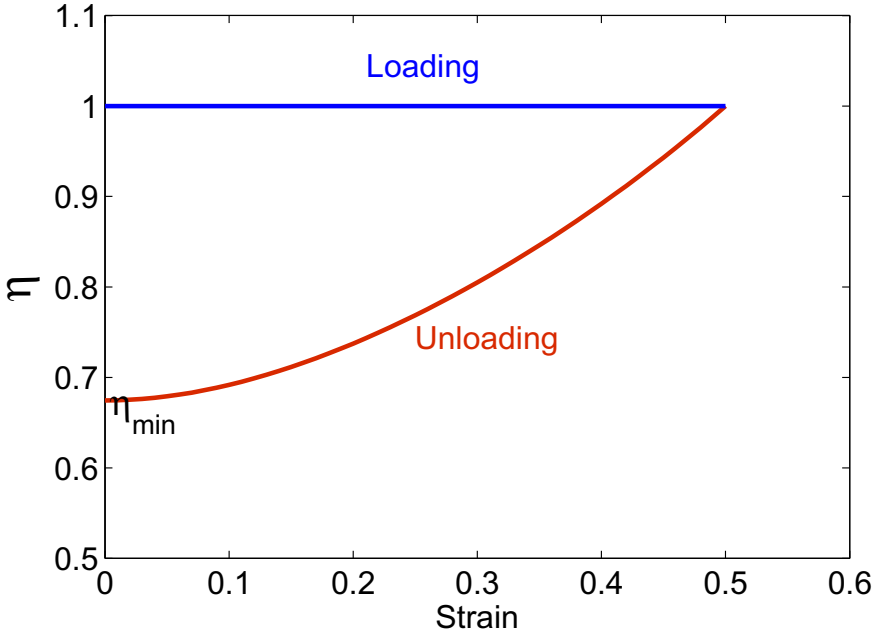

Figure 2.2: η versus strain for a sample loading case where the specimen is loaded up to 50% strain followed by unloading up to 0 % strain using $r = 6.08\text{E-}03$ and $m = 3.89\text{E-}01$.

curve-fitting of the pseudo-elasticity model to the experimental data is discussed in Chapter 3.

2.3.2 Fluid Phase Constitutive Description

The fluid phase is modeled as incompressible and inviscid. The momentum supply term $\boldsymbol{\pi}^s$ in equation (2.15) can be written as [36]

$$\boldsymbol{\pi}^s = p\nabla\phi^s - \boldsymbol{\pi}_0, \tag{2.61}$$

where $\boldsymbol{\pi}_0$ represents the diffusive drag caused due to the relative movement between the fluid and the solid. According to Darcy's law, this drag depends on the relative velocity

of the fluid phase with respect to the solid phase and can be written as

$$\boldsymbol{\pi}_0 = K\left(\mathbf{v}^s - \mathbf{v}^f\right). \tag{2.62}$$

Here, K is non-negative and is called the diffusive drag coefficient. It is related to the intrinsic permeability of the material, k, as

$$k = \frac{(\phi^f)^2}{K} \tag{2.63}$$

The permeability k is assumed to be constant in the linear biphasic theory. However, it is intuitively easy to guess that the material porosity and permeability should change with volumetric deformations, especially at large strains. If Φ_0 denotes the initial solidity or the initial solid fraction, then the current values of solid and fluid fractions, ϕ^s and ϕ^f can be obtained using the third invariant as

$$\phi^s = \frac{\Phi_0}{\sqrt{I_3}} \tag{2.64}$$

and

$$\phi^f = 1 - \frac{\Phi_0}{\sqrt{I_3}}. \tag{2.65}$$

In the nonlinear biphasic theory, the permeability is assumed to depend on the strain. The choice of the relationship between the permeability and strain largely affects the mechanical behaviour of the biphasic material. In this work, the exponential dependence of permeability on the strain, proposed by Holmes and Mow [37], will be used. The

permeability, k, is defined as

$$k = k_0 \left[\frac{\Phi_0 \phi^f}{(1 - \Phi_0)\phi^s} \right]^{\kappa} \exp \left\{ \frac{M(I_3 - 1)}{2} \right\}. \tag{2.66}$$

Here k_0 is the permeability at zero strain and κ and M are non-dimensional coefficients that should be found from experimental data.

2.4 Governing Differential Equations

The momentum equations can be further simplified using the constitutive equations in order to obtain the governing differential equations for the biphasic material. Substituting $\boldsymbol{\sigma}^s$ from equation (2.20) in equation (2.15), and using equation (2.61), we obtain

$$\nabla \cdot (-\phi^s p \mathbf{I} + \boldsymbol{\sigma}^e) + p \nabla \phi^s - \boldsymbol{\pi}_0 = 0. \tag{2.67}$$

Further simplification gives,

$$-\phi^s \nabla p + \nabla \cdot \boldsymbol{\sigma}^e = \boldsymbol{\pi}_0. \tag{2.68}$$

Similarly, for the fluid phase, using equations (2.21) and (2.61) in equation (2.16), we obtain,

$$\nabla \cdot (-\phi^f p \mathbf{I}) - p \nabla \phi^s + \boldsymbol{\pi}_0 = 0. \tag{2.69}$$

This can be simplified using equations (2.13), (2.62) and (2.63) to obtain the simplified momentum equation for the fluid phase,

$$\nabla p = \frac{\boldsymbol{\pi}_0}{\phi^f} = \frac{\phi^f}{k}(\mathbf{v}^s - \mathbf{v}^f). \tag{2.70}$$

Substituting this in equation (2.68), the simplified momentum equation for the solid phase is obtained as,

$$\nabla \cdot \boldsymbol{\sigma}^e = \frac{\boldsymbol{\pi}_0}{\phi^f} = \frac{\phi^f}{k}(\mathbf{v}^s - \mathbf{v}^f). \tag{2.71}$$

2.4.1 Uniaxial Deformation

Since it is easy to develop and solve analytical equations for uniaxial deformation, we will now specialize the momentum equations developed so far for the uniaxial deformation problem. From an experimental point of view also, uniaxial deformation is easy to achieve. Let us assume that the deformation and motion completely take place in the z direction [36] i.e. there is no flow of fluid or solid in the other two directions. This is typical of the so-called confined compression experiment, discussed later in chapter 3. The solid and fluid stresses in the z direction are given by

$$\sigma^s_{zz} = -\phi^s p + \sigma^e_{zz} \tag{2.72}$$

and

$$\sigma^f_{zz} = -\phi^f p \tag{2.73}$$

The momentum equations can be written as

$$\frac{\partial \sigma^e_{zz}}{\partial z} = \frac{\pi_0}{\phi^f} = \frac{\phi^f}{k}(v^s - v^f). \tag{2.74}$$

where the respective velocities are defined in the z direction, and

$$\frac{\partial p}{\partial z} = \frac{\partial \sigma^e_{zz}}{\partial z}. \tag{2.75}$$

This fluid phase equation is readily solvable and it is found that

$$p(z,t) = \sigma^e(z,t) + p_0(t), \tag{2.76}$$

where p_0 is another constant of integration determined from boundary conditions. For a uniaxial problem, the continuity equation (2.14) can be integrated in the z direction to obtain

$$\phi^s v^s + \phi^f v^f = v_0, \tag{2.77}$$

where v_0 is a constant of integration which can be found using the boundary conditions. Substituting this in the solid phase equation, we obtain

$$\frac{\partial \sigma^e_{zz}}{\partial z} = \frac{1}{k}(v^s - v_0). \tag{2.78}$$

Following the derivation in [36] and moving to a material coordinate system Z with solid displacement $U(Z,t)$ and solidity $\Phi^s(Z,t)$, for the uniaxial case, we can write the axial stretch as

$$\lambda = \frac{\partial z}{\partial Z} = 1 + \frac{\partial U}{\partial Z}. \tag{2.79}$$

Also, the velocity of the solid phase, v^s, can be written as

$$v^s = \frac{\partial U}{\partial t}. \tag{2.80}$$

From equation (2.78), we have

$$\frac{\partial \sigma^e}{\partial \lambda}\frac{\partial \lambda}{\partial Z}\frac{\partial Z}{\partial z} = \frac{1}{k}\left(\frac{\partial U}{\partial t} - v_0\right). \tag{2.81}$$

Using equation (2.79) in the above equation and simplifying, we obtain the governing differential equation for the uniaxial deformation problem as stated below

$$\frac{k}{\lambda}\frac{\partial \sigma^e}{\partial \lambda}\frac{\partial^2 U}{\partial Z^2} = \frac{\partial U}{\partial t} - v_0, \quad 0 < Z < h,\ t > 0 \tag{2.82}$$

where h is the thickness of the undeformed material.

Chapter 3

Materials, Experimental Methods, and Computational Modeling

This chapter discusses the materials, and experimental and computational methods used for this research. The candidate biomaterial used for preparation of the nanocomposites is *agarose*, a hydrogel typically used in articular cartilage tissue engineering [69, 59]. Different types of CNMs with different kinds of functionalizations are obtained from two sources. Experimental methods are established to study the effects of concentration, type and functionalization of the nanomaterials on the biocompatibility and mechanical properties of the nanocomposites. This chapter also discusses how robust computational models can be defined for the biphasic soft biomaterials based on experimental data. Data analysis techniques used for postprocessing the results of the mechanical tests and determining the solid and fluid phase constitutive parameters are presented.

3.1 Materials

3.1.1 Agarose

Agarose belongs to a family of polysaccharides known as agars. These are obtained from algae such as seaweed. These polysaccharides hold water and prevent dessication during low tide and also provide mechanical rigidity so that the cells do not collapse. They find applications in the food industry, for example, in ice-creams, desert jelly and instant whips as an ingredient stabilizer. The chemical structure of agarose is composed of two chains forming a tight left-handed double helix. It is structurally classified as a galactose polymer (galactan). Water gets trapped inside the double-helix since the chains are tightly wrapped. The ends of the two chains provide sites for attachment with other chains. This crosslinking develops a three-dimensional complex of helical tubes containing water. The strength of the gel is determined by the length of the helices/coils. The shorter the coils, the smaller the number of crosslinks and the weaker the gel, whereas longer coil gels are stronger due to more crosslinks. However, long coil gels hold less water compared to the short coil ones.

Fig. 3.1 shows a scanning electron microscope image of agarose gel [2]. As seen from the image, the microstructure clearly displays an interconnected network forming a porous structure. These pores trap water molecules which are exuded when a volumetric deformation is applied to the structure.

Agarose (Sigma) used in this research is obtained from Invitrogen Life Technologies, Carlsbad, CA.

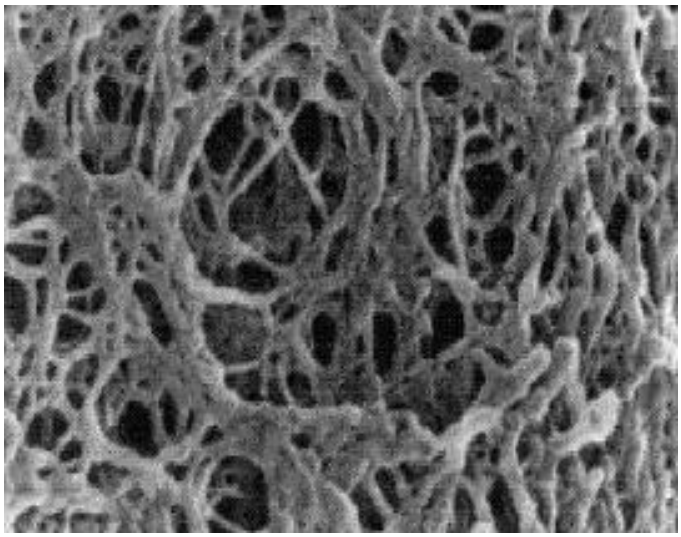

Figure 3.1: A scanning electron microscope image of agarose gel (Magnification: 50,000×) [2].

3.1.2 Carbon Nanomaterials

Different types of carbon nanomaterials (CNMs) with different kinds of functionalizations are obtained from two sources.

Set I

Carbon nanofibers (CNFs) and multi-walled carbon nanotubes (MWCNTs) in their base, untreated form as well as functionalized with the OH group and with oxygen (denoted by OX-functionalization henceforth) are obtained from the Nanoworld and Smart Materials and Devices Laboratory [3] at the University of Cincinnati. Thus, this set comprises of six nanomaterials: CNF, CNF-OH, CNF-OX, MWCNT, MWCNT-OH and MWCNT-OX.

Set II

The second set of CNMs are obtained from an external source, Nanolab Inc., Newton, MA. CNFs and single-walled carbon nanotubes (SWCNTs) in their base, untreated form

as well as functionalized with the carboxyl (COOH) group are obtained. This type of functionalization is chosen based on biocompatibility studies by Mooney et al. [62]. Thus four different nanomaterials are used from this source: CNF, CNF-COOH, SWCNT and SWCNT-COOH.

Structurally SWCNTs are single walled cylinders of rolled graphene sheets. MWCNTs are rolled graphene sheets arranged as concentric cylinders. CNFs, on the other hand, are cylindric nanostructures with graphene layers stacked as truncated cones. The average diameter of the CNFs obtained from the Nanoworld and Smart Materials and Devices Laboratory at the University of Cincinnati is 100 nm. The SWCNTs obtained from Nanolab Inc. have a diameter of about 1.5 nm and a length of about 1 to 5 μm. The CNFs have a diameter of about 50 nm and a length of about 20 μm.

3.2 Goals of Experimentation

The goal of the current work is to explore the use of CNMs as reinforcements for tissue engineering scaffold biomaterials. As discussed in the research objectives in the first chapter, the specific aims are to investigate the effects of CNM concentration, type and functionalization on the biocompatibility and mechanical properties of the nanocomposites. Experiments are designed to evaluate the biocompatibility and the mechanical properties of the nanocomposites.

The mechanical tests are designed such that the results of these tests not only help in comparison of the improvement in mechanical properties, but also provide experimental data for developing robust computational models for the nanocomposites. The mechanical testing protocols are designed to develop a standard method for complete

characterization of the solid and the fluid phase properties of agarose and its nanocomposites. This should facilitate the constitutive description of both phases. It should be noted, however, that all the mechanical tests are performed in compression. It is very difficult to perform tension tests on agarose because it is very weak in tension.

As suggested in the literature and discussed in the first chapter, homogeneous dispersion of the carbon nanomaterials in the matrix biomaterial is essential for effective load transfer from the matrix to the nanomaterials. It is, therefore, also essential to study the dispersion of the nanomaterials in agarose. Dispersion characterization is the key to a better understanding of the materials' mechanical response.

The following is the experimental test plan summary for this research.

3.2.1 Test Plan Summary

In this section, we summarize the experimental work for this research. Table 3.1 provides the summary in a tabular format. The details of the specific experiments will be discussed in the subsequent sections.

Part A: Study of the Effect of CNM Concentration

The effect of CNM concentration on the biocompatibility and mechanical properties of agarose is studied. CNFs supplied by the Nanoworld and Smart Materials and Devices Laboratory at the University of Cincinnati, are used for this study. CNFs in two different concentrations 0.2% and 2.0% (wt. CNF/wt. agarose gel) are mixed with 2.0% (wt./vol. of PBS) agarose and these are compared with a control (2.0% agarose only) case. Biocompatibility and mechanical tests are performed and the results from the mechanical tests are used for computational modeling of these composites as biphasic

	Materials Used	Experiments			Computational Modeling
		Biocompatibility Tests	Mechanical Tests	Dispersion Characterization	
Part A: Effect of CNM Concentration	CNF	Cell Viability (Cellular constructs)	(a) Unconfined compression (50%) (b) Confined compression	x	(a) Solid Phase (b) Fluid Phase
Part B: Effect of CNM Type and Functionalization	**Set I:** CNF CNF-OH CNF-OX MWCNT MWCNT-OH MWCNT-OX	Cell Viability (CNM + Cells)	Unconfined compression (30%)	(a) Optical Microscopy (b) Scanning Electron Microscopy (SEM)	x
	Set II: CNF CNF-COOH SWCNT SWCNT-COOH	Cell Viability (Cellular constructs)	Unconfined compression (30%)	Optical Microscopy	Solid Phase
Part C: Mechanical Characterization of Selected CNM	CNF-COOH	x	(a) Unconfined compression loading and unloading (50%) (b) Confined compression	x	(a) Solid Phase (b) Fluid Phase

Table 3.1: Test Plan Summary

materials.

Biocompatibility Tests

Biocompatibility tests, in the form of cell viability tests, are performed using live/dead staining of the constructs seeded with cells. Cell viability is assessed with respect to CNF concentration.

Mechanical Tests

Unconfined Compression Tests

Multi-step unconfined compression tests are performed where the specimens are loaded upto 50% strain in increments of 5% strain with each ramp followed by a dwell period of 1.5 hours for stress-relaxation. Lateral deformations are optically measured at each equilibrium point. The equilibrium stress-strain response coupled with the lateral deformation data is used to develop constitutive relationships for the solid phase (recall equation (2.44)).

Confined Compression Creep Tests

Single-step confined compression creep tests are performed in order to develop the constitutive relationship for the fluid phase and to determine the permeability constants (recall equation (2.66)).

The results from the mechanical tests are used for studying the improvement in the mechanical properties of agarose nanocomposites with respect to concentration of the CNFs added.

Part B: Study of the Effect of CNM Type and Functionalization

Different types of CNMs with different kinds of functionalizations are obtained from two sources as described earlier. Set I consists of CNF, CNF-OH, CNF-OX, MWCNT,

MWCNT-OH and MWCNT-OX and set II consists of CNF, CNF-COOH, SWCNT and SWCNT-COOH. These CNMs are mixed with 2.0% (wt./vol. of PBS) agarose at a concentration of 0.2% (wt. CNM/wt. agarose gel). These materials are compared with respect to biocompatibility and mechanical properties. In addition to this, dispersion characterization is performed for the nanocomposites to obtain a better understanding of the mechanical response. The following experiments are performed separately for the nanocomposites prepared using CNMs from each set.

Biocompatibility Tests

Set I

Cell viability tests are performed by simply suspending CNMs on top of cells are cultured in a monolayer in a dish. Cell viability is compared for different types and functionalizations of CNMs in set I.

Set II

Cell viability tests using live/dead staining are performed similar to those performed in part A. Cell viability is compared for different types and functionalizations of CNMs in set II.

Mechanical Tests

Unconfined compression tests are performed similar to those performed in part A. In this study, however, strain increments of 10% strain are used with a maximum strain of 30%. A reduced dwell period of one hour is used at each step for stress relaxation since it is observed from preliminary tests that the material reaches equilibrium within this period. Confined compression experiments are not performed in this study.

Dispersion Analysis

Set I

Dispersion of the CNMs in agarose is studied using optical microscopy and Scanning Electron Microscopy (SEM).

Set II

Dispersion of the CNMs in agarose is studied using only optical microscopy.

Dispersion analysis provides a good microstructural insight for understanding the material's mechanical response.

Part C: Detailed Mechanical Characterization of Selected CNM Nanocomposite

The results obtained from the study in part B are used to select the type and functionalization of CNM that provides the maximum enhancement in the mechanical properties of agarose without compromising its biocompatibility. The purpose of this study is to perform detailed mechanical testing of the agarose nanocomposite prepared with the selected CNM for robust computational modeling of the material. The selected CNM is used at a concentration of 0.2% (wt. CNM/wt. agarose gel) with 2.0% (wt./vol. of PBS) agarose. The following experiments are performed for the mechanical characterization

Mechanical Tests

Unconfined Compression Tests

Similar to part A, multi-step unconfined compression tests are performed where the specimens are loaded upto 50% strain in increments of 5% strain with each ramp followed by a dwell period for stress-relaxation. A reduced dwell period of 1 hour is used making sure that equilibrium is reached at each step. Loading is followed by unloading where the strain is reduced in steps of 5% decrements with dwell period of 1 hour in each step for stress recovery. Lateral deformations are optically measured at each equilibrium

point. The equilibrium stress-strain response coupled with the lateral deformation data is used to develop constitutive relationships for the solid phase.

Confined Compression Creep Tests

These are exactly similar to those performed in part A.

The results from the mechanical tests are used for computational modeling of the agarose nanocomposite, prepared using the selected CNM, as a biphasic material.

3.3 Specimen Preparation

Part A

CNFs are used at three different concentrations, 0% (control), 0.2% and 2.0% (wt. CNF/ wt. agarose), chosen based upon similar toxicity studies in the literature [53]. These are mixed with 2.0% (wt./vol. of PBS) agarose. Two kinds of specimens are prepared. Ones with cells (cellular constructs) are used for testing the biocompatibility of the composites and the ones without cells (acellular constructs) are used for mechanical characterization.

Part B

Each CNM is used at a concentration of 0.2% (wt. CNM/wt. agarose gel) and mixed with 2.0% (wt./vol. of PBS) agarose. One control case with 0% CNM and 2.0% (wt./vol. of PBS) agarose is also prepared. Similar to part A, two kinds of specimens are prepared. Cellular constructs are used for biocompatibility testing and acellular constructs are used for mechanical testing and dispersion characterization.

Part C

The CNM selected from part B is used at concentrations of 0% (control) and 0.2% (wt. CNM/wt. agarose gel) and mixed with 2.0% (wt./vol. of PBS) agarose. Only

acellular constructs are prepared for this study.

3.3.1 Preparation of Acellular Constructs

Part A

CNFs, at concentrations of 0% (control), 0.2% and 2.0% (wt. CNF/wt. agarose gel), are added to phosphate buffered saline (PBS). This mixture is first sonicated using a probe sonicator for 5 minutes for proper dispersion of the nanomaterials. Agarose (sigma) powder at a concentration of 2% (wt./vol. of PBS) is then added to the mixture. This mixture is then steam-sterilized at a temperature of 124 °C in an autoclave. After the autoclave cycle, the mixture is sonicated for an additional minute. These composites are then cooled to 45 °C in a water bath and cast between glass plates spaced about 2.5 mm apart in a custom mold. The composites are then allowed to gel at room temperature for 20 minutes. Once the mixture solidifies, it is immediately immersed in fluid (PBS) and kept hydrated in an incubator at a temperature of 37 °C. The gel is stored for at least two hours before testing in order to allow uniform swelling of all samples. A sterile 4 mm biopsy punch is used to create full-thickness, disk-shaped specimens for mechanical testing.

Part B

The method of preparation of the acellular constructs for this study is similar to that in part A with the exception of using each of the CNMs at a concentration of 0.2% (wt. CNM/wt. agarose gel) only. One control case is prepared with 0% CNM.

Part C

Acellular constructs are prepared for the selected CNM and a control case as in part B.

3.3.2 Preparation of Cells

Experiments using animal subjects or materials are conducted in accordance with the Guide for the Care and Use of Laboratory Animals (NIH Publication No. 8523, revised 1996) and University of Cincinnati Institutional Animal Care and Use Guidelines [1].

Part A

Chondrocytes are harvested from the rib cartilage of newborn mice and cultured in monolayer to passage 7. In a sterile environment, the cells are removed, centrifuged and re-suspended in normal culture medium. A final concentration of 5×10^5 viable cells/ml is placed in a T75 flask. The culture medium consists of Dulbecco's Modified Eagle's Medium (DMEM, Gibco NY, USA) containing 10% (vol/vol) fetal bovine serum (FBS) and 3% penicillin (100 U/ml) / streptomycin (100 μg/ml). The T75 flasks are incubated at 37 °C in a humidified 5% CO_2 incubator for 72 hours prior to seeding. Culture medium is changed every 3-4 days. Non-adherent cells are removed during medium changes.

Part B

For the CNM comparision studies, bone marrow cells harvested from tibias and femurs of euthanized adult Spraque-Dawley rats are used. Only passage 2-4 mesenchymal stem cells (MSCs) are used in this study. The procedure for the preparation of cells is the same as in part A.

Part C

Since cellular constructs are not prepared in this study, no cells are required.

3.3.3 Preparation of Cellular Constructs

Part A

The cells are detached from the culture dish using trypsin. After the cells are fully

detached, culture medium is added and the suspension is centrifuged. The supernate is removed and culture medium is added to obtain cell suspension with a cell concentration of 1×10^6 cells/ml. CNF-agarose composites are prepared as previously described for acellular constructs with the exception of using 0%, 0.4% and 4.0% (wt. CNF/wt. agarose gel) CNFs with 4% (wt./vol. of PBS) agarose, i.e., double the concentration used earlier for both CNFs and agarose. Once the composite gel is cooled to 40 °C, equal volumes of gel and cell suspension are combined to result in a 2% (wt./vol. of PBS) agarose mixture with CNF concentrations of 0%, 0.2% and 2.0% (wt. CNF/wt. agarose gel). This is cast in a multiwell dish under sterile conditions. The mixture is allowed to gel for 20 minutes at room temperature. Once the mixture gels, 2 ml of culture medium is added to each well. The multiwell dish is then incubated at 37 °C in a humidified 5% CO_2 incubator. Media is changed every other day.

Part B

The procedure for the preparation of cellular constructs is similar to part A with the exception that the initial concentration of CNMs used is 0.4% (wt. CNM/wt. agarose gel) to result in a final concentration of 0.2% (wt. CNM/wt. agarose gel) CNM after the addition of the cell suspension. One control case with 0% CNM is also prepared.

Part C

No cellular constructs are required for this study.

3.4 Biocompatibility (Cell Viability) Tests

Parts A and B (set II)

The biocompatibility of the nanocomposites is assessed by performing cell viability tests

using live/dead staining. After four days of culture, cells within the cellular constructs are labeled using Live/Dead stain (Molecular Probes) according to the vendor's protocol. Cells are viewed under a fluorescent microscope (Zeiss Axiovert) with a standard fluorescein filter (live cells) and a propidium filter (dead cells).

Part B (set I)

The biocompatibility of the nanocomposites in this set is assessed by simply suspending the CNMs on top of the cells cultured in monolayer in a dish. At the end of four days of culture, the cells are viewed under a flourescent microscope. Live cells appear spread out and dead cells appear rounded.

3.5 Mechanical Testing

3.5.1 Multi-step Unconfined Compression Tests

Objective of the Experiment

The goal of the unconfined compression experiments is to obtain the constitutive parameters for the solid phase. It is known that agarose is a biphasic material composed of fluid trapped in a porous solid. When sudden compressive deformations are applied to the mixture, initially the load is completely borne by the fluid due to pressurization. The mixture behaves like an incompressible solid instantaneously. However, as time progresses, the fluid slowly exudes from the pores and the load is shared by the solid and the fluid simultaneously. The response load gradually reduces. The transient response of the mixture is governed by several factors such as the porosity of the solid, the interconnectivity of the pores, the fluid pressure in the surrounding media, the viscosity of the

fluid and the fluid-solid interaction. Eventually, at equilibrium, when the fluid pressure inside the pores reduces to that equal to the fluid pressure in the surrounding media, then the load is completely carried by the solid phase. Thus, the equilibrium response solely depends on the solid phase properties. It is clear that the combined behavior of the mixture is viscoelastic. The multi-step unconfined compression experiments are performed such that the mixture is allowed to reach equilibrium after applying strain increments in steps. These equilibrium responses are used to develop a constitutive relationship for the solid phase in compression.

Testing System

The testing system used for performing the unconfined compression tests is a DC servo-controlled electromechanical test system (TestResources 100R) manufactured by TestResources Inc., Shakopee, MN. A 2.2 lb (10N) load cell is used for all the unconfined compression tests performed. Fig. 3.2 shows a picture of the testing system. The accuracy of the system is $\pm$ 0.2% to 0.5% of the load cell capacity and the position resolution is 0.07 microns.

Experiment Description

Part A

Acellular constructs are used for all the mechanical tests. Disk shaped specimens of 4 mm diameter and 2.5 mm height are obtained using a biopsy punch. The height and diameter of the sample are recorded in the beginning using a vernier caliper. The sample is then placed in a sufficiently deep chamber (dish) and is kept hydrated in PBS throughout the experiment. The indenter is then lowered into the chamber until it is in

Figure 3.2: Test Resources 100R Testing System used in the unconfined compression experiments.

contact with the top surface of the specimen. A tare load of 0.001N is applied to ensure contact. This load is less than the reaction load at 1% strain. A multi-step compressive strain profile is applied as shown in Fig. 3.3. The strain ramps are applied with a displacement rate of 0.01 mm/s for the 5% strain increment followed by a dwell period of 1.5 hours for stress relaxation. This is repeated up to 50% strain. The load history data is recorded and post-processed to obtain the nominal stress.

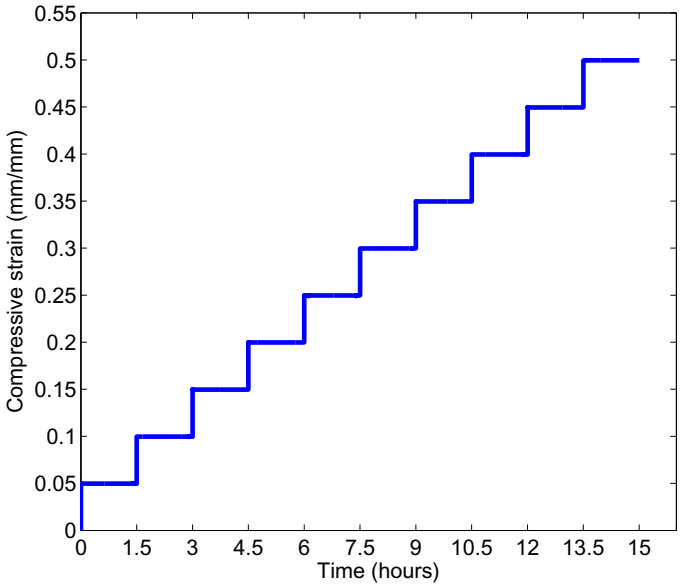

Figure 3.3: Strain profile for unconfined compression tests for part A.

It must be noted that since the indenter and the base are rigid and non-porous, fluid flow is only allowed in the radial direction through the vertical outer surface of the cylindrical specimen.

Optical measurement of Poisson's Ratio

In order to develop a robust model for the solid composed of volumetric and deviatoric components of the strain energy density function, it is important to measure the compressibility of the material. This is accomplished by measuring the lateral deformation in addition to the axial stress at each equilibrium step. This provides a good measure of the compressibility of the material. The lateral deformations are relatively very small for agarose due to high porosity and compaction during compression. Optical measurement of the lateral deformation turns out to be the most suitable option due to the difficulty of using conventional strain gages in the set-up.

The specimen is photographed at the beginning of the experiment and at the end of each equilibrium step. The camera (Nikon CoolPix 5700; 5.0 Megapixels; 8× optical zoom) is programmed to take pictures at each equilibrium point automatically. Figure 3.4 shows the images obtained for a 2.0% CNF specimen at equilibrium at 0% and 50% strains. The lateral deformations are measured by postprocessing the digital images

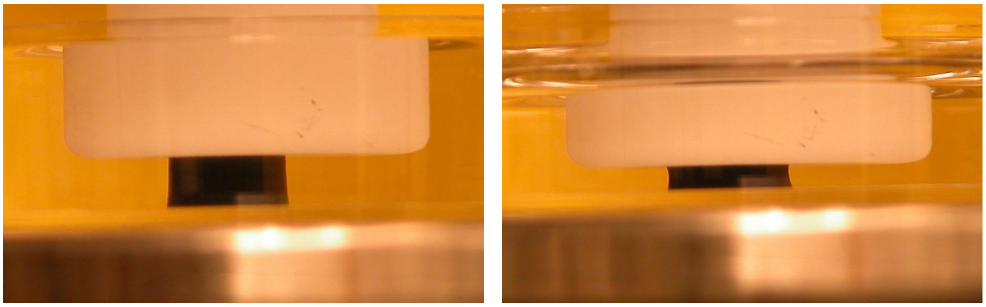

(a) 0% strain (b) 50% strain

Figure 3.4: Photographs of a 2.0% CNF specimen subjected to unconfined compression test at (a) 0% strain and at (b) 50% strain.

using the National Instruments Corporation (Austin, TX) software NI-ImaqVision with machine vision and measurement capabilities. The test data is smoothened by fitting a polynomial over the data and this smoothened data is used for the constitutive modeling of the solid phase.

Part B

The procedure used for performing the unconfined compression experiments for this study is similar to that used in part A with the exception that 10% strain increments are used up to a maximum compressive strain of 30%. The dwell period for each step is reduced to one hour making sure that equilibrium is reached at every step. Fig. 3.5 shows the strain profile used for this study. As in part A, measurement of the lateral deformation is performed optically.

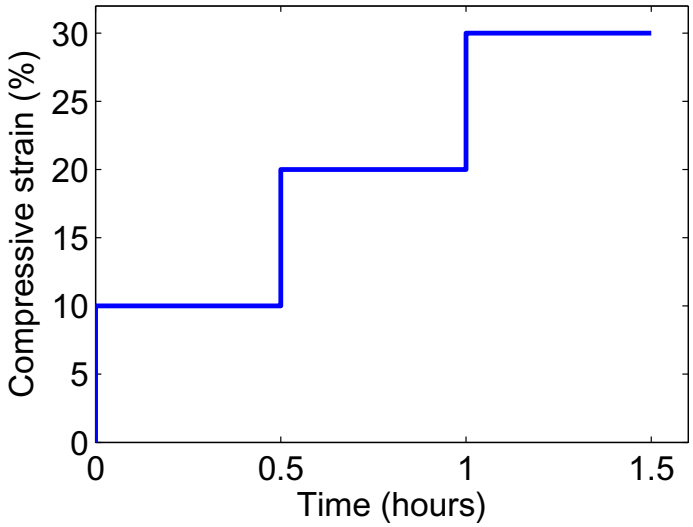

Figure 3.5: Strain profile for unconfined compression tests for part B.

Part C

For this study, the procedure used for the unconfined compression experiments is also similar to part A. However, in this case the multistep loading is followed by multistep unloading of the specimen. During loading 5% strain increments are applied up to a maximum compressive strain of 50%. A dwell period of one hour is used at each step for stress relaxation. This is followed by unloading where the strain is reduced in steps of 5% decrements with a dwell period of one hour in each step for stress recovery. Stress recovery is the exact opposite of stress relaxation. When the load on the specimen is suddenly removed, the compressive stress instantaneously drops and gradually rises to an equilibrium value as the specimen expands. Fig. 3.6 shows the strain profile used for this study. The lateral deformation of the specimens is measured optically during both loading and unloading.

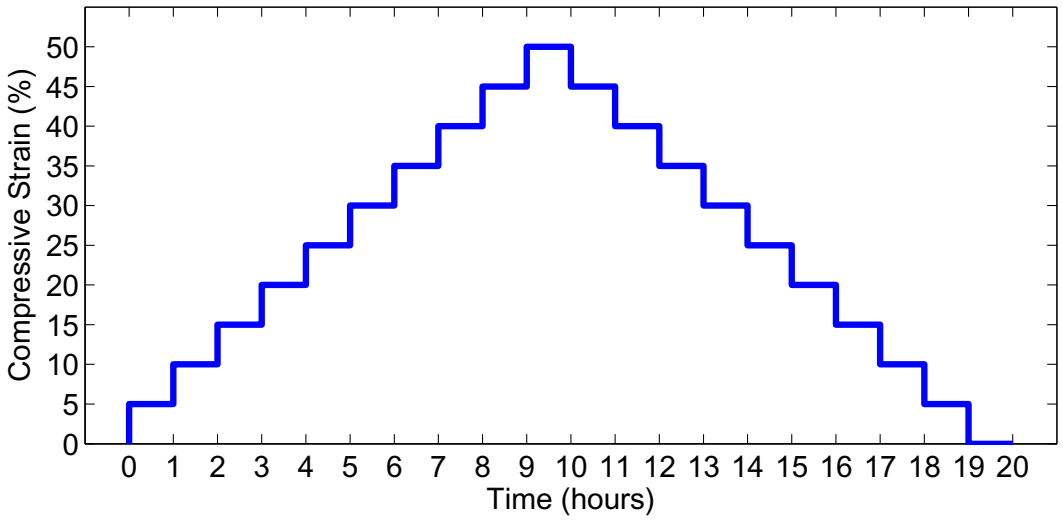

Figure 3.6: Strain profile for unconfined compression tests for part C involve loading and unloading.

3.5.2 Confined Compression Creep Tests

Objective of the Experiment

Confined compression creep tests have been routinely performed on soft tissues for quite some time. Mow et al. [66] and Holmes [36], among others, used confined compression creep tests as a method for understanding the fluid-solid interaction of the articular cartilage and other hydrated tissues. These tests are used as a standard to determine the fluid phase strain-dependent permeability constants for the biphasic material.

Testing system

A custom built confined compression testing system (Stress Engineering Services Inc., Mason, OH) is used for the confined compression creep tests. Fig. 3.7 shows the confined compression testing unit. The system is capable of applying a single dead weight of 0.3 N.

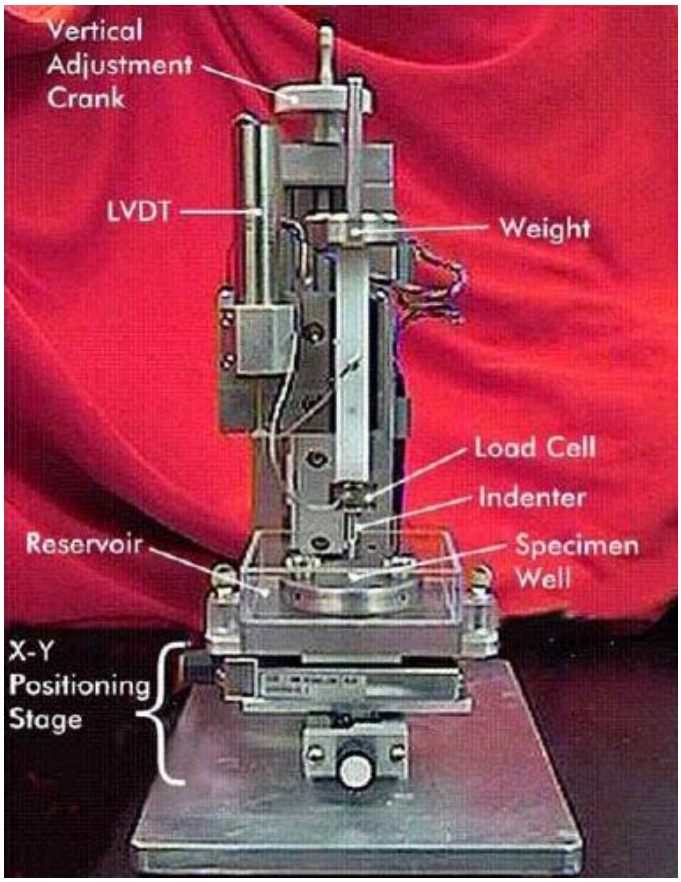

Figure 3.7: Confined compression testing unit.

The load is measured with a high resolution load cell (Sensotec Corporation, Columbus, OH) and the displacement is measured using an LVDT (Sensotec). Data acquisition is done using LabView (National Instruments, Austin TX).

Experiment Description

Parts A and C

The acellular constructs used in the unconfined compression tests are reused in the confined compression creep tests. The cylindrical specimens are placed in a confined

cylindrical well which has an inner diameter of 4 mm (equal to the specimen diameter). The bottom of the well is made up of a porous filter with pores large enough to allow free flow of fluid from the surface of the specimen into the reservoir. The side walls, however are rigid and non-porous. Thus, there is no radial flow of the fluid or lateral expansion of the solid. The deformation is purely uniaxial. The specimen is loaded by a non-porous platen/indenter with a dead weight. The dead-weight is instantaneously applied and the displacement of the indenter is recorded with respect to time. The displacement data is post-processed to obtain the strain history curve. Fig. 3.8 shows the schematic for the confined compression experiment. The fluid flows through the bottom porous

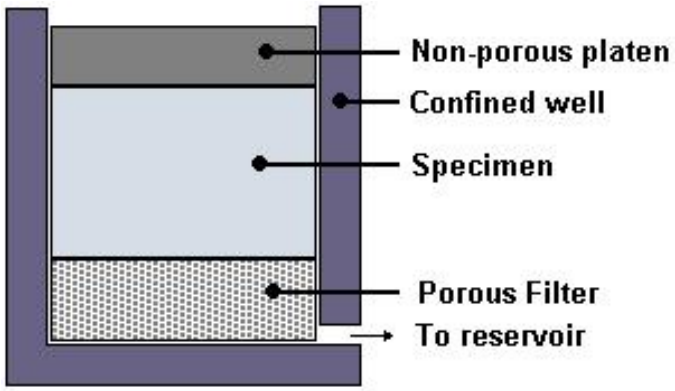

Figure 3.8: Confined compression test schematic

filter. The whole assembly is immersed in the reservoir to maintain the specimen in a hydrated state at all times. The load is held constant for 20000 seconds. This time period is selected based on previous experiments in order to guarantee that equilibrium has been reached.

3.6 Dispersion Analysis

3.6.1 Using Optical Microscopy

Part B (Set I and II)

Thin slices of about 0.5 mm thickness are cut from the acellular constructs and placed on glass slides to be viewed under an optical microscope (Zeiss Axiovert) at 400× magnification. Agarose, being transparent, clearly displays the dispersion of the CNMs.

3.6.2 Using Scanning Electron Microscopy

Part B (Set I)

Thin slices of about 0.5 mm thickness are cut from the acellular constructs and placed on stubs. These are then viewed under a scanning electron microscope to obtain images at magnifications ranging from 40× to 15000×.

3.7 Determination of Material Parameters From Experimental Data

The numerical modeling of the biphasic material requires the determination of the unknown material parameters. This includes the unknown constants in the strain energy density function for the solid phase constitutive description (see section 2.3.1) and in the strain-dependent permeability definition for the fluid phase (see section 2.3.2). The solid phase material constants are derived using the equilibrium data obtained from the unconfined compression experiments and the permeability coefficients are derived using the creep data obtained from the confined compression creep experiments as discussed

earlier. This section describes the detailed procedure used to determine these constants from experimental data.

3.7.1 Determination of the Solid Phase Material Parameters

Parts A, B and C

It is observed that the equilibrium loading stress-strain data for agarose and its nanocomposites as obtained from the unconfined compression tests are highly nonlinear, especially at high strains. Thus, it is clear that a linear elastic model is not sufficient to define the solid phase. It is necessary to consider a nonlinear hyperelastic model that fits the equilibrium loading curve. Also, the lateral deformation data obtained from the optical measurement suggest that the materials are highly compressible and the Poisson's ratio is not constant with respect to axial stretch. This suggests that the conventional incompressible or nearly incompressible models are not sufficient to describe the materials being tested. It is necessary to use a strain energy density function that accommodates the highly compressible nature of these materials. Obtaining a strain energy density function that fits the equilibrium strain-strain data and also simultaneously fits the lateral stretch data is a challenging task.

Agarose is modeled as a highly compressible, isotropic, hyperelastic material through the loading phase. If unloading is considered, a pseudo-elastic model is required for agarose. This is discussed later in this section for part C. Among the available forms of compressible hyperelastic strain energy density functions, the Ogden-Hill strain energy potential is the most suitable for agarose. This form is typically used to model foam-like or elastomeric materials. This potential is available in the commercial finite element package, ABAQUS under the name 'Hyperfoam'. Curve-fitting to obtain the material

parameters is performed in ABAQUS and the procedure is as described below.

Curve Fitting Using ABAQUS

The strain energy function for the Ogden-Hill material model, as discussed in Chapter 2, is given by

$$\psi_0^s = \sum_{i=1}^{N} \frac{2\mu_i}{\alpha_i^2} \left[\lambda_1^{\alpha_i} + \lambda_2^{\alpha_i} + \lambda_3^{\alpha_i} - 3 + \frac{1}{\beta_i} \left(J^{-\alpha_i \beta_i} - 1 \right) \right]. \tag{3.1}$$

The goal is to determine the unknown material parameters, μ_i, α_i and β_i in order to completely define the solid phase. The nominal stress, T_j obtained from this definition of the strain energy function is given by

$$T_j = \frac{\partial \psi_0^s}{\partial \lambda_j} = \frac{2}{\lambda_j} \sum_{i=1}^{N} \frac{\mu_i}{\alpha_i} \left(\lambda_j^{\alpha_i} - J^{-\alpha_i \beta_i} \right) \tag{3.2}$$

For the unconfined compression experiment, if $\lambda_1 = \lambda_A$ defines the axial stress, then $\lambda_2 = \lambda_3$ is the lateral stretch and the Jacobian is given by $J = \lambda_A \lambda_2^2$. The axial component of the nominal stress is, thus, given by

$$T_A = \frac{\partial \psi_0^s}{\partial \lambda_A} = \frac{2}{\lambda_A} \sum_{i=1}^{N} \frac{\mu_i}{\alpha_i} \left(\lambda_A^{\alpha_i} - J^{-\alpha_i \beta_i} \right) \tag{3.3}$$

Data obtained from unconfined compression experiments include nominal stress and lateral stretch with respect to change in axial stretch. This data is fit to the above equation using a nonlinear least squares minimization algorithm in ABAQUS that tries to minimize the relative difference between the experimental stress and analytical stress. ABAQUS employs the Marquard-Levenberg algorithm in the formulation by Twizell [98]

to obtain the unknown parameters by an iterative solution scheme [41]. This minimization is constrained by certain stability criteria on the strain energy density function as will be discussed further.

The finite element analysis problem simulates the unconfined compression experiment in ABAQUS using a single 8 noded axisymmetric continuum element with reduced integration (CAX8R). The strain energy density function cannot be completely arbitrary and is subject to certain constraints. Improper definitions of the strain energy function can lead to material instabilities and numerical problems in the solution of boundary-value problems [76, 32]. Material instability leads to physically unrealistic stress-strain curves. For example, compressive stresses may occur for tensile stretches. This generally occurs for modes of deformation outside the domain in which testing has been done for parameters' estimation. One of the constraints imposed on the strain energy density function is that it is required to be positive. Bilgili [11] provided a detailed discussion of the methods used to restrict the strain energy density function for hyperelastic models based on thermodynamical, mechanical and empirical criteria in order to obtain physically realistic definitions.

ABAQUS performs material stability checks along the primary deformation modes using the Drucker stability condition [41] which requires that the change in the Kirchhoff stress $\mathrm{d}\tau$ due to an infinitesimal change in the logarithmic strain $\mathrm{d}\epsilon$ satisfies the following inequality

$$\mathrm{d}\tau : \mathrm{d}\epsilon > 0 \tag{3.4}$$

which implies

$$\mathrm{d}\epsilon : \mathcal{D} : \mathrm{d}\epsilon > 0 \tag{3.5}$$

where $\mathcal{D}$ is the tangential material stiffness. Thus, the stability criterion requires that $\mathcal{D}$ should be positive definite.

The axial strain, lateral strain and nominal axial stress are provided to ABAQUS in a tabulated format and ABAQUS returns the material parameters μ_i, α_i and β_i with the stability information. In addition to the experimental data, the user is required to specify the value of the parameter N, which can take values from 1 to 6. However, this order should be selected carefully. The larger the value of N, the higher the oscillations in the numerical solution scheme and the higher the instabilities in the stress-strain curves. The lower the value of N, the lower the nonlinearity of the stress-strain curve and the lower the accuracy of the fit. Typically, when experimental data upto 50% strain is available, N=2 or 3 is chosen and when data upto 30% strain is available N=1 or 2 is chosen [41].

Part C

In part C, unloading data is available in addition to loading data and the material is modeled using a pseudo-elasticity model as described in section 2.3.1. The goal is to determine the parameters μ_i, α_i and β_i in the definition of $\psi_0^s(\lambda_1, \lambda_2, \lambda_3)$ as given in equation (3.1) and the parameters r and m used in the definition of η as given in equation (2.58).

In order to obtain the parameters μ_i, α_i and β_i, we use the equilibrium axial stress-strain and the equilibrium lateral strain data during the loading phase as discussed earlier.

In order to define η, both the loading and the unloading equilibrium stress-strain data are required. From equations (2.54) and (2.55), we see that η is a variable scaling factor

between the loading and the unloading stresses.

$$\eta = \frac{\sigma_j^e}{\sigma_{0j}^e} = \frac{T_j}{T_{0j}}. \tag{3.6}$$

The experimental values of η are obtained by taking the ratio of the nominal unloading stresses to the nominal loading stresses. The expression for η given in equation (2.58) is

$$\eta = 1 - \frac{1}{r}\tanh\left[\frac{\psi_{max}^s - \psi_0^s(\lambda_1, \lambda_2, \lambda_3)}{m}\right]. \tag{3.7}$$

This is curvefit to the experimental values of η using a nonlinear least squares algorithm in MATLAB in order to obtain the unknown parameters r and m.

Knowing r and m, the dissipation function $\phi(\eta), \eta$ and hence the pseudo-energy function given by equation (2.51) can be completely defined. The nominal loading and the unloading stresses can be computed from the pseudo-energy function using equation (2.53).

3.7.2 Determination of the Fluid Phase Permeability Coefficients

Parts A and C

Having determined the solid phase material properties from the unconfined compression test data, the next goal is to determine the permeability coefficients from the confined compression creep test data. The permeability coefficients, k_0, κ and M, as defined in Chapter 2 in equation (2.66), are used to define the fluid phase permeability. These are obtained by curve-fitting experimental strain-time data to the solution of the governing

differential equation for the confined compression problem as described below.

Governing Differential Equation for the Confined Compression Problem

In Chapter 2, momentum equations (2.70) and (2.71) are specialized for uniaxial problems and given by equations (2.75) and (2.78). The governing equation for the boundary value problem is given by equation (2.82). In the confined compression experiment, the deformation is strictly one-dimensional. The boundary conditions for this experiment are as shown in Fig. 3.9, which provides an axisymmetric model of the cylindrical disc. The bottom surface is free-draining. Hence the pressure is zero on the bottom surface while flow is restricted on the remaining boundaries. Radial displacement is restricted at all points. A dead load is suddenly applied on the top surface with a non-porous indenter. Since there is no flow of fluid across the top surface, using equation (2.77),

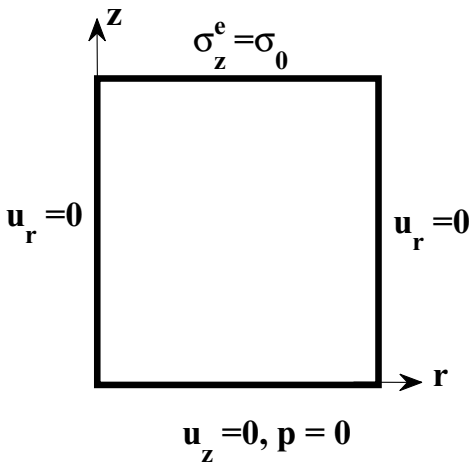

Figure 3.9: Boundary conditions for confined compression experiments.

we get $v_0 = 0$. Hence, the governing equation for the boundary value problem can be

written as

$$\frac{k}{\lambda}\frac{\partial \sigma^e}{\partial \lambda}\frac{\partial^2 U}{\partial Z^2} = \frac{\partial U}{\partial t}, \quad 0 \leq Z \leq h, \ t \geq 0 \tag{3.8}$$

and is subject to the initial condition,

$$U(Z, 0) = 0, \tag{3.9}$$

and the following boundary conditions,

$$U(0, t) = 0, \tag{3.10}$$

$$\sigma^e(h, t) = \sigma_0, \tag{3.11}$$

where, σ_0 is the applied load on the top surface. It should be noted that in the governing differential equation σ^e is the solid phase elastic stress and can be completely defined once the solid phase parameters are established from the unconfined compression experiments.

Finite Difference Approximation of the Confined Compression Problem

The governing differential equation (3.8) cannot be solved analytically since it has non-linear parameters. The coefficient,

$$H(\lambda, t) = \frac{k}{\lambda}\frac{\partial \sigma^e}{\partial \lambda}, \tag{3.12}$$

is a function of λ and t, where $\lambda = 1 + \dfrac{\partial U}{\partial Z}$. The permeability is also strain-dependent as defined by equation (2.66) Hence, a numerical implicit finite difference method is employed and the equation is solved iteratively.

The Z coordinate is discretized using grid points Z_i, where $i = 0$ to n is the node index

and the time axis is discretized with grid points t_j, where $j = 1, 2...$ is the time index. Let $U^k_{i,j} = U^k(Z_i, t_j)$ denote the finite difference approximation of $U(Z,t)$ at the end of the kth iteration. Then the finite difference approximation of the governing equation is given by,

$$\left(\frac{H^k_{\lambda+\Delta\lambda,j} - H^k_{\lambda-\Delta\lambda,j}}{2\left(\Delta\lambda\right)}\right)\left\{\frac{U^{k+1}_{i+1,j} - 2U^{k+1}_{i,j} + U^{k+1}_{i-1,j}}{\left(\Delta h\right)^2}\right\} = \frac{U^{k+1}_{i,j} - U^k_{i,j-1}}{\Delta t}. \tag{3.13}$$

Here, $\Delta h = h/n$, where h is the height of the specimen and $n+1$ is the number of nodes, such that $Z_{i=0} = 0$ and $Z_{i=n} = h$. The time step is denoted by $\Delta t = t_j - t_{j-1}$. The finite difference approximation is solved using the Thomas algorithm [94] for the tri-diagonal system of equations until a converged solution for $U^k_{i,j}$ was obtained.

Optimization Algorithm

The coefficient H includes the permeability k which contains the unknown constants k_0, κ and M for the strain dependent permeability relation given in equation (2.66). These parameters are determined by using an optimization algorithm that minimizes the difference between the experimental strain history with respect to time and the numerical strain history obtained from the solution of the finite difference approximate problem discussed above. The optimization algorithm used, called the Amoeba algorithm, is a search method for nonlinear unconstrained optimization, also known as the Nelder-Mead Simplex algorithm [75]. This method requires only function evaluations, not derivatives and is efficient for multi-dimensional optimization. The algorithm returns the values of the fluid phase permeability parameters for minimum difference between the experimental and the numerical strain data.

Chapter 4

Results and Discussion

In this chapter, we present the results obtained for the experiments and computational modeling performed in parts A, B and C. We discuss these results in detail in this chapter and provide the conclusions and some suggestions for future work in the next chapter.

4.1 Part A: Study of the Effect of CNM Concentration

4.1.1 Biocompatibility Tests

Fig. 4.1 shows the results for the live-dead staining experiment performed on the cellular constructs. The tests are performed as described in section 3.4. The cells within the constructs are arranged in a three-dimensional arrangement. As a result, it is difficult to focus on them. Also, since the cells do not have a flat substrate for attachment, they appear rounded and spherical and not spread out as they would when cultured in monolayer on a dish. The top three pictures show live cells as green dots viewed

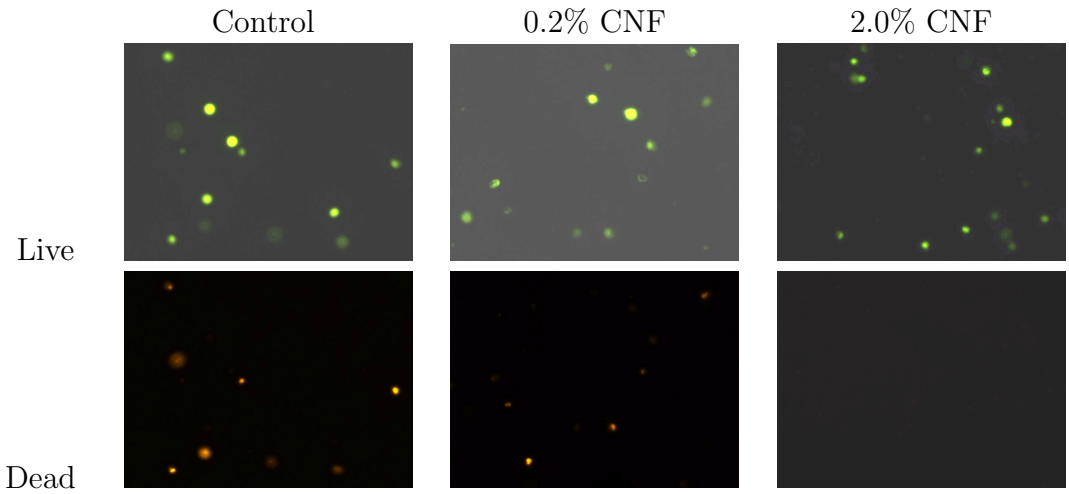

Figure 4.1: Cell viability test results showing live (green) and dead (red) cells in the composites after live/dead staining (Part A).

using a fluorescein filter for 0% (control), 0.2% and 2.0% CNF concentrations. The bottom three pictures show dead cells as red dots viewed using a propidium filter. We see that viable cells (green) are observed in the control as well as 0.2% and 2.0% CNF specimens. Dead cells, as indicated by red dots, are also observed, although in smaller amounts in the CNF-composites. The intensity of both stains in the 2.0% CNF group appeared comparatively lower. This is likely due to difficulties of imaging through the dense CNF.

The cell viability tests prove that cells actually survive in the presence of CNF and the increase in the concentration of CNF does not have a significant effect on cell viability. These preliminary tests help us make a qualitative assessment of the biocompatibility of these nanomaterials. It is important, however, to perform a quantitative analysis of the biocompatibility in order to qualify their use in tissue engineering scaffolds. This forms a part of the future work for this research.

4.1.2 Mechanical Tests

Multi-step Unconfined Compression Tests

The results of the unconfined compression tests are presented in this section. The strain profile applied to the specimens is as shown in Figure 3.3. The typical load history data obtained with respect to time is as shown in Fig. 4.2. It is clearly seen that the

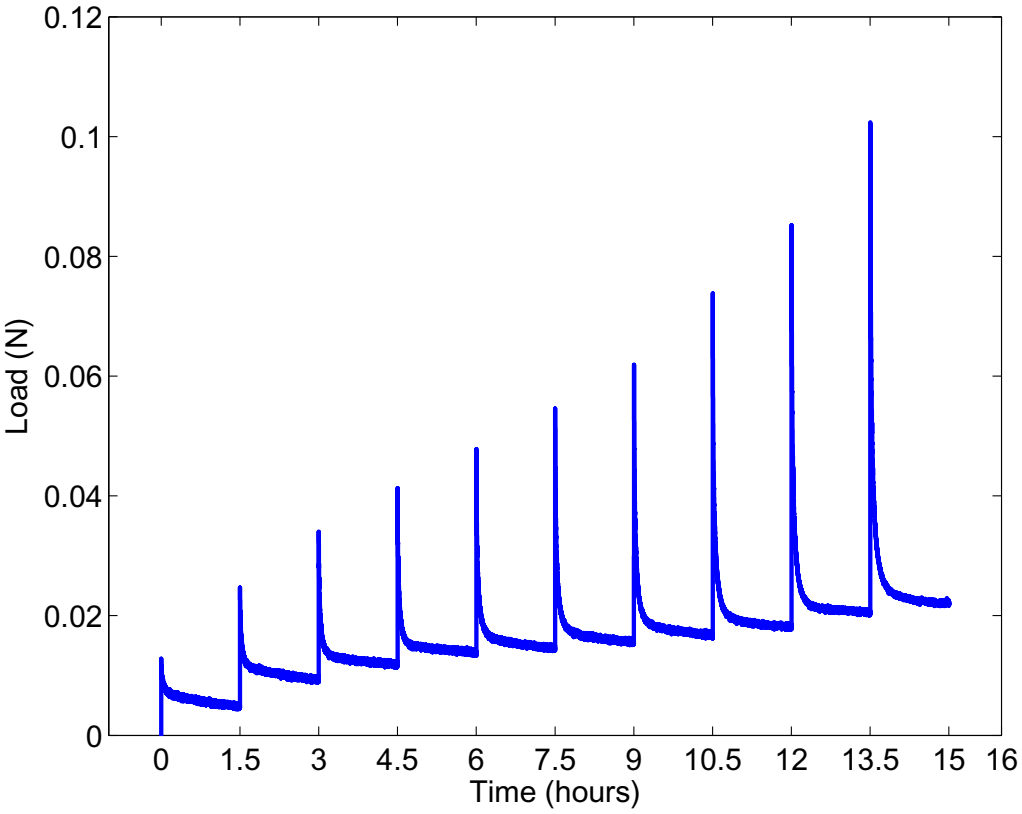

Figure 4.2: Typical load vs. time curve obtained for the unconfined compression tests (Part A).

biphasic material displays a viscoelastic response in the form of stress relaxation for the multi-step unconfined compression tests. The viscoelastic response of the biphasic

material can be attributed to the interactions between the fluid and the solid phases [54, 7] or to a combination of the interactions and the intrinsic viscoelasticity of the solid phase [90, 26, 23, 25, 24]. The intrinsic solid phase viscoelasticity is out of the scope of this research due to the lack of advanced experimental techniques to measure the solid phase viscoelasticity. Hence, the viscoelastic response is completely attributed to the interactions between the fluid and the solid phase. The solid phase itself is assumed to be nonlinearly elastic. The equilibrium values of the stress is computed for each strain increment from the load history data and is used to produce the stress-strain data for each specimen. In this study, three specimens of each material ($n = 3$) are tested. Figure 4.3 provides the mean values and standard error for equilibrium stress with respect to the axial strain for the three different materials tested. It is seen that the errorbar values are pretty low suggesting low variability in a single batch. Thus, n = 3 is a reasonable choice for number of specimens tested. The stress-strain data for all three cases is seen to follow the same S-shaped behavior. This is a characteristic feature of foam-like or elastomeric materials. Initially the stress-strain curve is fairly linear up to about 10% strain, followed by softening response from 10% to 30% strain which can be attributed to cell-wall buckling, which in turn is followed by a hardening response beyond 35% strain due to consolidation of the matrix. Clearly, there is a noticeable improvement in the mechanical properties due to the addition of CNF. However, from the graphs it is easy to guess that the enhancement in mechanical properties is not a linear function of the increase in concentration of CNF in the composite. This will be verified quantitatively once a numerical model is defined for the solid phase.

Fig. 4.4 provides the mean values and standard error for the Poisson's ratio versus axial strain as measured from the photographs taken at each equilibrium step. The Poisson's

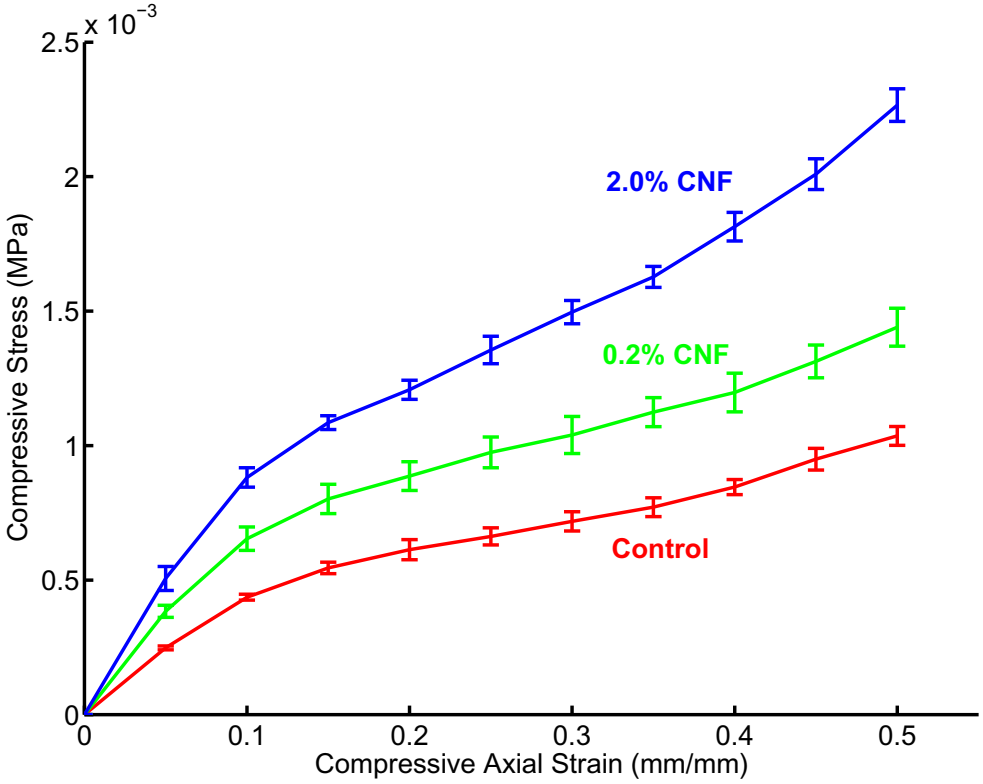

Figure 4.3: Equilibrium compressive stress vs. axial compressive strain data obtained from unconfined compression tests for the 0% (control), 0.2% and 2.0% CNF cases (Part A)

ratio for the three materials is not constant and depends on the axial strain. The value of the Poisson's ratio decreases with increase in axial strain. Also, the Poisson's ratio is significantly less than 0.5 suggesting that these materials are highly compressible. Thus, the incompressible or nearly incompressible forms of the strain energy density function are not suitable for describing such a material. It is also necessary to accommodate for a Poisson's ratio that varies with axial strain.

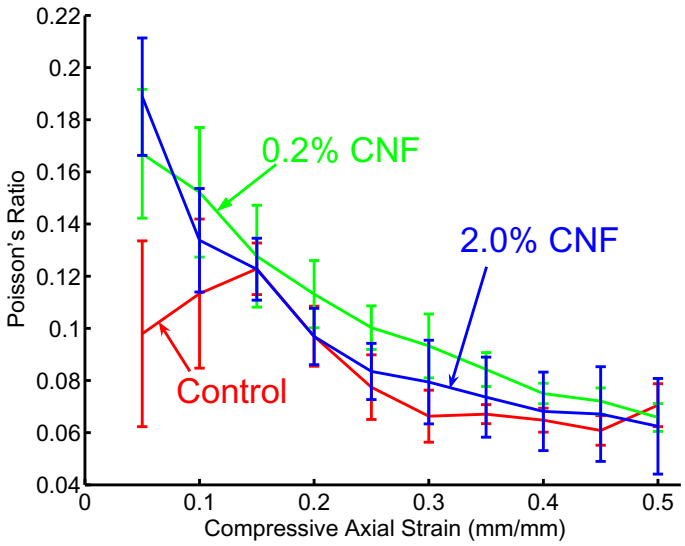

Figure 4.4: Poisson's ratio versus axial compressive strain data obtained from unconfined compression tests for 0% (control), 0.2% and 2.0% CNF cases (Part A).

Confined Compression Creep Tests

The confined compression creep tests are described in section 3.5.2. A sudden dead load is applied to the top surface of the specimens and the strain at the top surface is measured with respect to time. Fig. 4.5 shows the curves for one representative specimen for each of the three CNF concentrations. We see that the strain reaches an equilibrium value after about 4000 seconds. This kind of creep behavior is typical of viscoelastic materials. The biphasic material displays such a behavior due to fluid-solid interaction. The specimen gradually reaches equilibrium as the fluid is allowed to flow out through the porous filter at the bottom.

The results of these tests are used to model the fluid phase permeability as is discussed in the next subsection.

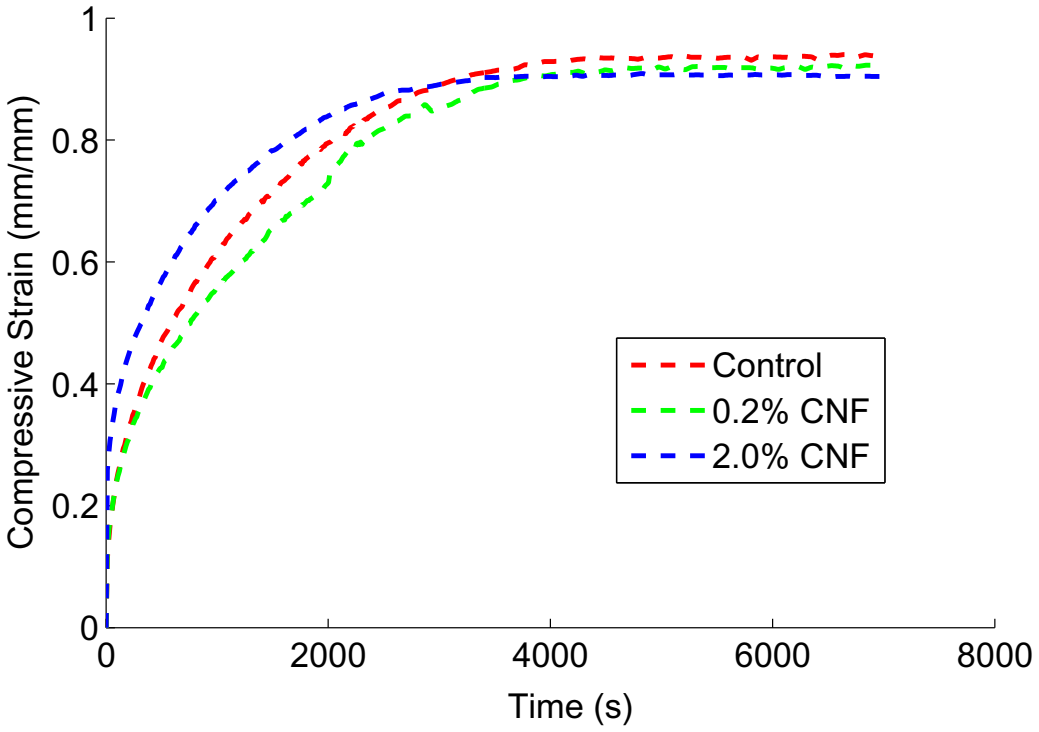

Figure 4.5: Strain history data obtained from confined compression tests for 0% (control), 0.2% and 2.0% CNF cases (Part A).

4.1.3 Computational Modeling of the Biphasic Composites

The results from the mechanical tests are used to develop a robust computational model for agarose and its composites with a complete constitutive description of the solid phase and the strain-dependent permeability. In this subsection, we discuss the solid phase material parameters for the Ogden-Hill strain energy potential and the fluid phase permeability constants obtained for the three CNF concentrations from the unconfined and confined compression tests respectively.

Solid Phase Material Properties

Several forms of the strain energy function for compressible hyperelastic isotropic materials were tried for curve-fitting over available experimental equilibrium stress-strain data from the unconfined compression experiments. The Ogden-Hill potential or the Hyperfoam model [41] defined in ABAQUS, provided the most satisfactory fit of all the options tried. The process of obtaining the material parameters for the Ogden-Hill potential using the equilibrium stress-strain data is described in section 3.7.1. The nominal lateral strain data and nominal equilibrium stress data are supplied to ABAQUS in order to obtain the unknown material parameters through a optimization algorithm. The finite element problem for unconfined compression is solved using a single-element discretization. The value of order N for the Ogden model is decided by trial and error. It was found that $N = 2$ provided the best fit with the least root mean square (RMS) error.

For each CNF concentration, 3 specimens are tested. Material parameters are obtained for each of the 3 specimens and the mean of the 3 specimens. Fig. 4.6 shows the comparison of the experimental data and the finite element model obtained for the three different CNF concentrations after curve-fitting for $N = 2$. Only the mean plots are shown for the three CNF concentrations. We see that the model provides an excellent fit over experimental data. The RMS error is observed to be within 3% for all specimens and means and is tabulated in Table 4.1. The results are presented in two formats as follows.

Mean of the properties (MoP): This is the set comprised of the means of the material parameters obtained for each specimen via curve-fitting

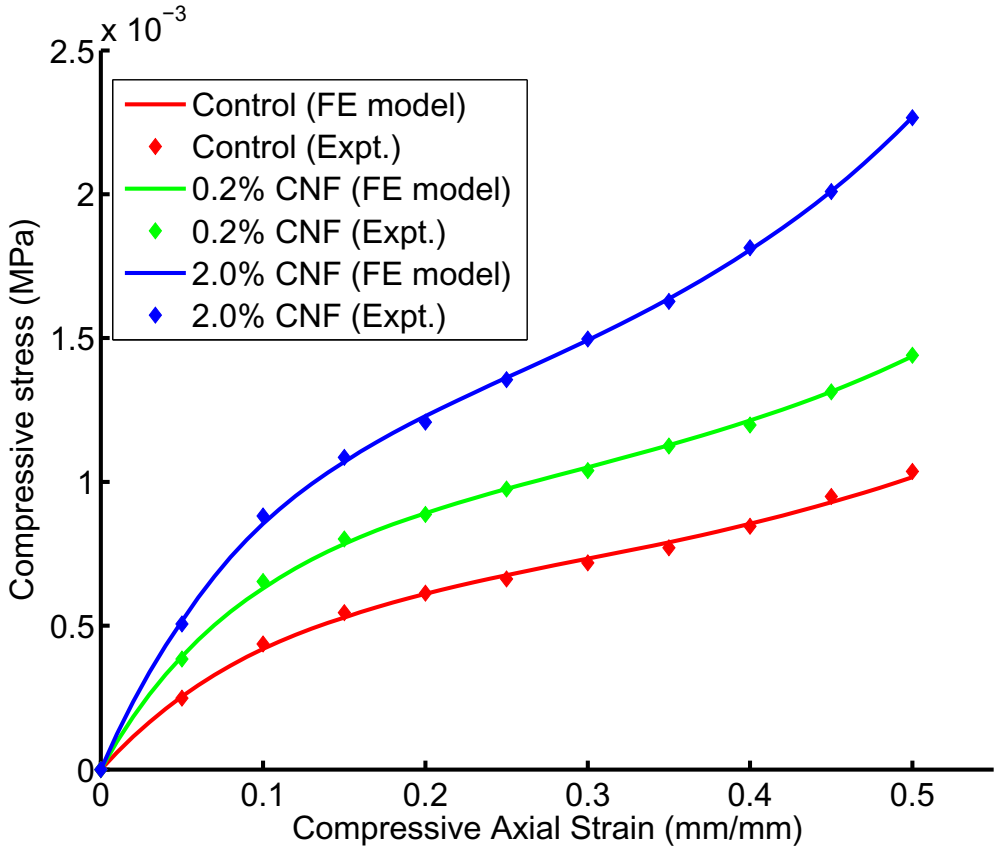

Figure 4.6: Curve-fitting the finite element model over the experimental data for 0% (control), 0.2% and 2.0% CNF. Dots represent experimental data and solid lines represent the finite element model predictions (Part A).

Properties of the mean (PoM): This is the set comprised of the material properties of the mean of the experimental data i.e. a mean data set is created from the experimental data and this mean data is supplied to the curve-fitting algorithm. The parameters thus obtained formed the PoM set.

Physically meaningful quantities like the initial shear modulus and the initial bulk modulus, as defined in equations (2.41) and (2.42), are reported. Table 4.1 provides the properties of mean (PoM) and the mean of properties (MoP) with their standard devia-

Table 4.1: Properties of mean and mean of properties along with RMS errors for the solid phase obtained from curve-fitting (Part A).

		Properties of Mean	Mean of Properties (Mean±SD)
Control (0% CNF)	μ_0 (MPa)	0.0028	0.00274 ± 0.00007
	κ_0 (MPa)	0.00259	0.00291 ± 0.00054
	RMS error (%)	2.81	2.76 ± 0.4576
0.2% CNF	μ_0 (MPa)	0.00427	0.00419 ± 0.00015
	κ_0 (MPa)	0.00536	0.0054 ± 0.00080
	RMS error (%)	1.38	1.743 ± 0.570
2.0% CNF	μ_0 (MPa)	0.00521	0.00512 ± 0.00052
	κ_0 (MPa)	0.00753	0.0077 ± 0.00106
	RMS error (%)	1.17	2.27 ± 0.455

tions for the three different concentrations of CNF considered. The RMS errors for the means and the mean RMS errors and their standard deviations are also reported in the table.

Comparison of the material properties from Table 4.1 is shown graphically in Fig. 4.7 which plots the mean of properties. The initial shear modulus increases by about 53% and 87% with the addition of 0.2% and 2.0% CNF respectively and the initial bulk modulus increases by about 86% and 165% with the addition of 0.2% and 2.0% CNF respectively. This is a significant enhancement in the mechanical properties considering the amount of carbon nanofibers added.

The solid phase can be completely characterized by the material parameters μ_i, α_i and β_i. Once the solid phase is completely defined, the solid phase material properties are used in the the optimization algorithm to determine the strain-dependent permeability constants.

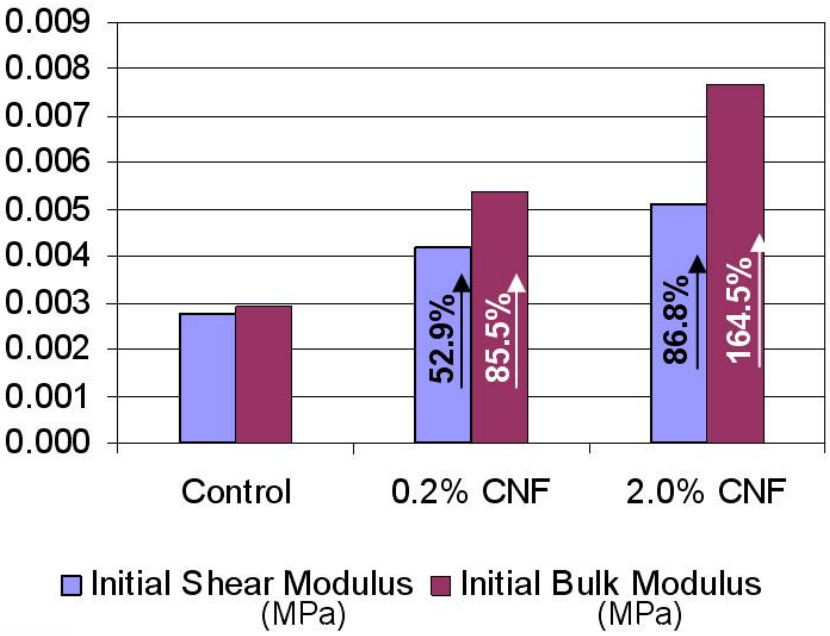

Figure 4.7: Comparison chart for the initial bulk and shear moduli for 0% (control), 0.2% and 2.0% CNF cases (Part A).

Strain-dependent Permeability

The strain history data is used to obtain the fluid phase permeability constants. The governing differential equations are solved using a finite difference approximation and the optimization is carried out using the Amoeba algorithm as discussed in section 3.7.2. Fig. 4.8 shows the comparison of the solution obtained from the finite difference approximation of the confined compression problem and the experimental data for three specimens, one from each of the three CNF concentrations. The solid phase material parameters derived from the unconfined compression experiments are used in this algorithm. We observe that the numerical approximation provides a very good fit over the experimental data. It is found that in the strain-dependent permeability equation (2.66), the coefficient $\left[\frac{\Phi_0\phi^f}{(1-\Phi_0)\phi^s}\right]$ does not significantly affect the dependence of per-

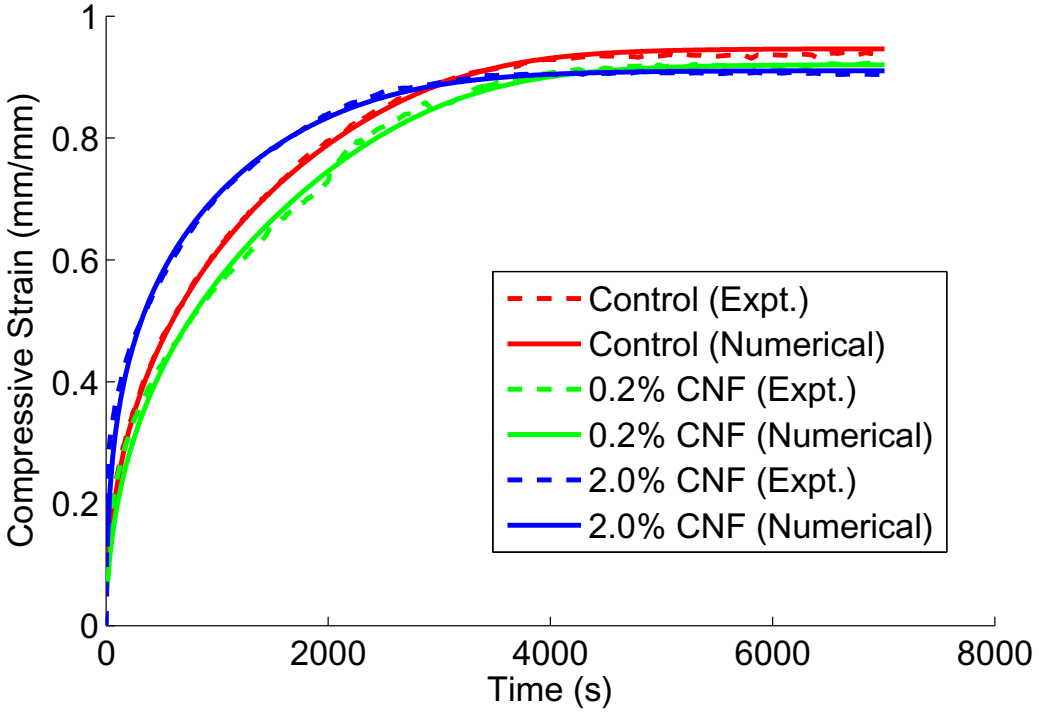

Figure 4.8: Comparison between the numerical and experimental data for the confined compression creep tests for 0%, 0.2% and 2.0% CNF cases (Part A).

meability on strain. Hence, we assume $\kappa = 0$ and use the optimization algorithm to determine the other two parameters k_0 and M. Table 4.2 provides the mean values and standard deviations of the two parameters for the three CNF concentrations. It is observed that the optimization algorithm is highly sensitive to the initial values used for k_0 and M. This can be attributed to the fact that the optimization is highly non-linear and unconstrained. Thus, these parameters have to be chosen judiciously. It is found that there are multiple combinations of k_0 and M that provide satisfactory fit to the experimental data i.e. the solution to the optimization algorithm is not unique. In summary, in part A, we studied the effect of CNF concentration on the mechanical

Table 4.2: Mean values and standard deviations of the strain dependent permeability parameters k_0 and M (Part A).

	k_0 (Mean ± SD) (m^4/Ns)	M (Mean ± SD)
Control (0% CNF)	1.64E-10 ± 6.45e-11	12.28 ± 1.57
0.2% CNF	7.17E-11 ± 4.74E-11	10.29 ± 1.88
2.0% CNF	1.77E-10 ± 8.25E-11	12.39 ± 1.71

properties and biocompatibility of agarose. We observed that the CNFs enhance the mechanical properties of agarose in a concentration dependent manner. Biocompatibility test results indicated that CNF-agarose constructs do not cause any cytotoxicity in mice chondroctyes. Mechanical testing protocols are established for characterization of agarose and its nanocomposites as biphasic materials. Computational models developed for the solid and fluid phase agree well with experimental results.

4.2 Part B: Study of the Effect of CNM Type and Functionalization

4.2.1 Biocompatibility Tests - Set I

Biocompatibility tests for this set are performed by suspending the CNMs in a dish in which cells are cultured in monolayer as described in section 3.4. Fig. 4.9 shows the images obtained of the cells after four days of culture for all CNM cases in this set. Live cells appear flat and spread out, while dead cells appear small and rounded.

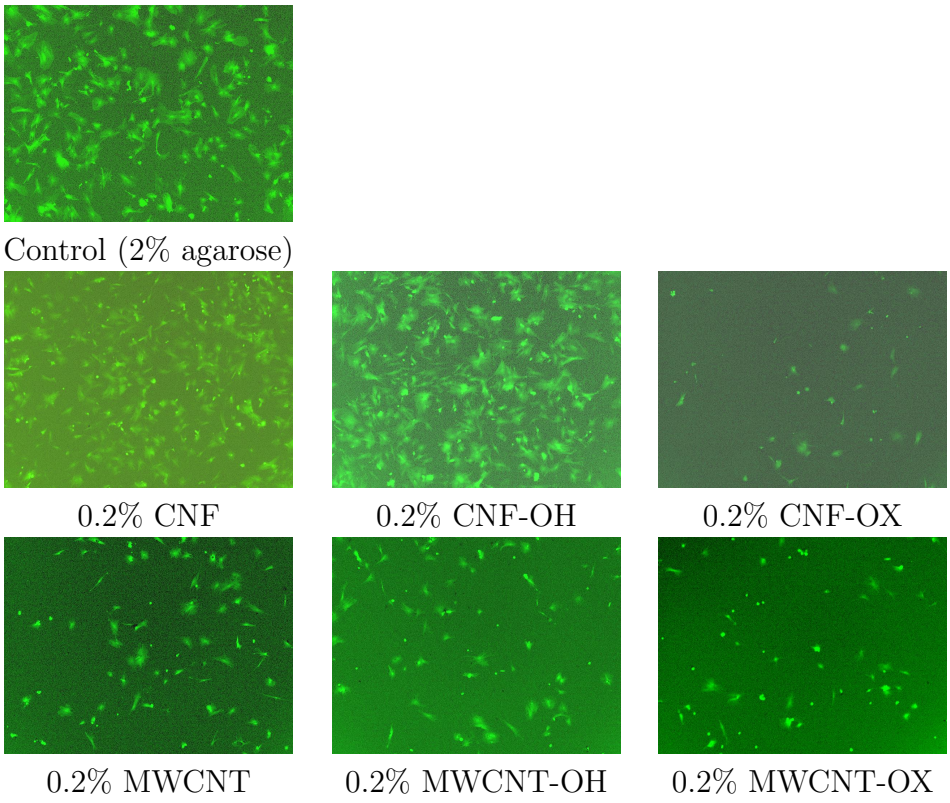

Figure 4.9: Cell viability test results for set I showing live and dead cells in the dish. Live cells appear flat and spread out while dead cells appear rounded (Part B).

Most of the dead cells get washed away during media changes. Thus, the total number of cells visible in the images are also an indicator of the cell viability in the presence of the CNMs. We see that the number of living cells in the case of 0.2% CNF-OX, 0.2% MWCNT, 0.2% MWCNT-OH, and 0.2% MWCNT-OX, is very low indicating that these CNMs adversely affect cell viability. Thus, these tests suggest that these materials display cytotoxicity with respect to rat MSCs. In the case of Control, 0.2% CNF and 0.2% CNF-OH, sufficient number of live cells are observed in the dish indicating that these materials do not cause any significant cytotoxicity with respect to rat MSCs.

As discussed in part A, the cell viability tests are preliminary tests that help us make

only a qualitative assessment of the biocompatibility of the CNMs. Quantitative analysis is important and forms a part of the future work for this research.

4.2.2 Dispersion Characterization - Set I

The dispersion of the CNMs in agarose is studied using two methods for the nanocomposites prepared in this set. These are discussed below.

Dispersion Characterization Using Optical Microscopy

The agarose nanocomposites are observed under an optical microscope and images are obtained at 400× magnification. Figure 4.10 shows the images obtained for the six nanocomposites prepared in this set. It is observed that the CNFs, with and without

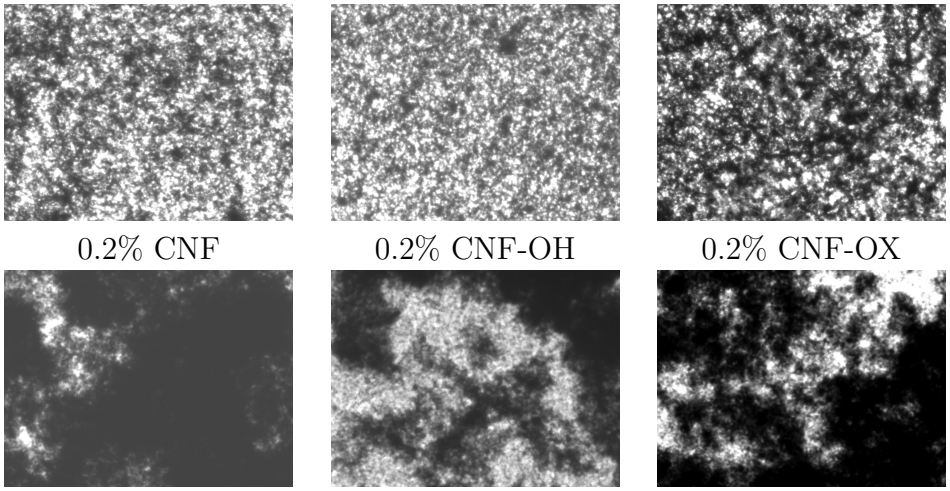

Figure 4.10: Optical microscopy images (400× magnification) of the nanocomposites in set I (Part B).

functionalization disperse relatively better than MWCNTs, with and without functionalization. Among the CNFs, those with OH functionalization disperse the best. This

has been observed to be directly related to the mechanical properties as will be discussed in the next section.

Dispersion Characterization Using Scanning Electron Microscopy (SEM)

SEM images are obtained for all six nanocomposites prepared in this set at magnifications ranging from 40× to 15000×. The images obtained at 5000× magnification are presented in Fig. 4.11. The SEM images for the CNFs (with and without functional-

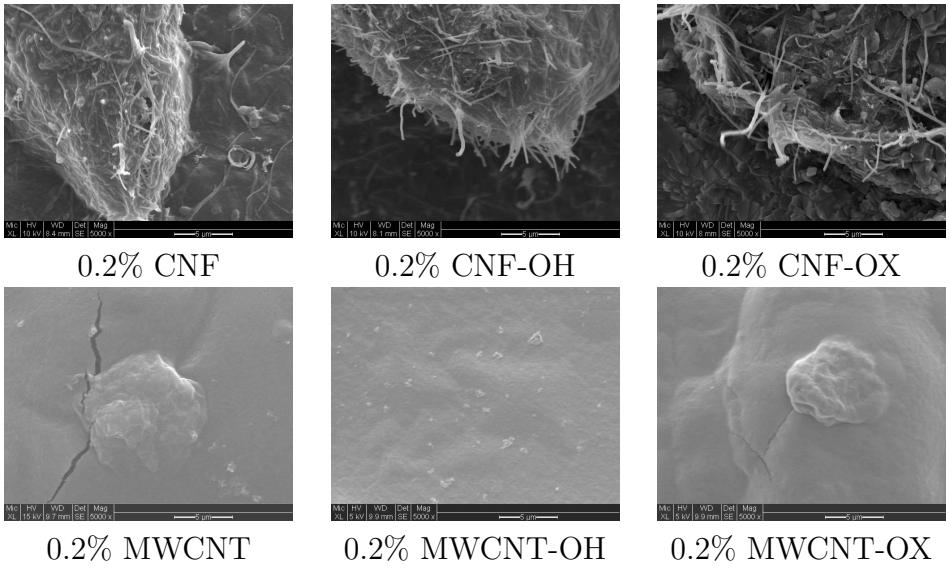

Figure 4.11: Scanning Electron Microscope (SEM) images (5000× magnification) of the nanocomposites in set I (Part B).

ization) show independent CNFs dispersed within the composites. However, in the case of MWCNTs, the nanotubes appear as agglomerated groups. This indicates that the quality of dispersion is better in the case of CNFs than MWCNTs. The results from the SEM images are in agreement with those obtained from the optical microscopy studies.

4.2.3 Mechanical Tests - Set I

The equilibrium loads from the unconfined compression experiments are used to obtain the equilibrium nominal stress-strain data for the specimens tested. Fig. 4.12 displays the mean values and standard errors for the equilibrium nominal stress with respect to axial strain for the seven materials tested. The standard error is observed to be very low

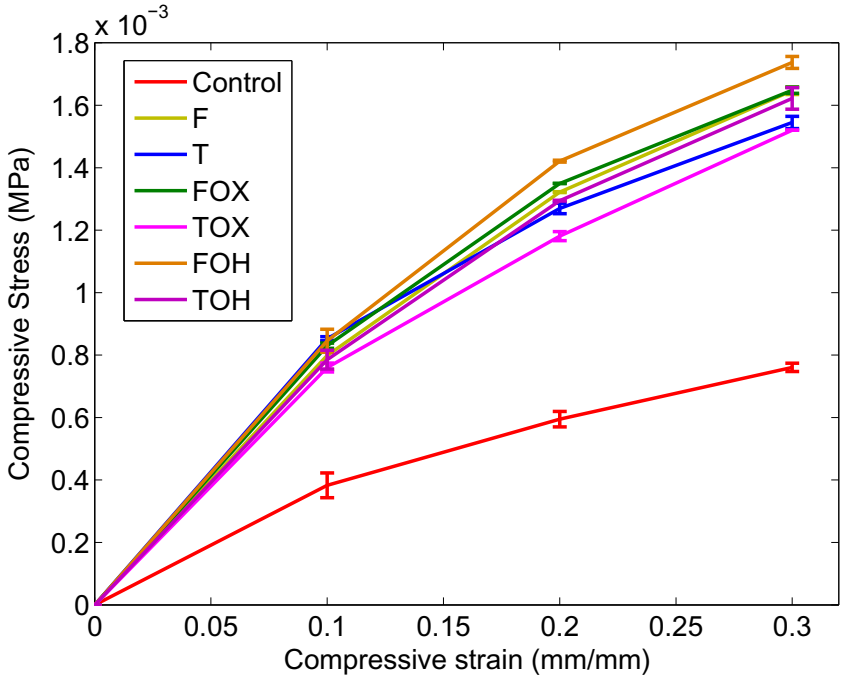

Figure 4.12: Compressive axial stress-strain data obtained from unconfined compression tests for the nanocomposites in set I (Part B).

for all cases suggesting a low variability within the batch. The stress-strain curves show a typical elastomeric behavior where we have a softening behaviour at higher strains due to cell wall buckling. We see that all CNMs in this set provide significant enhancement in the mechanical properties of agarose. CNFs, with and without functionalization, perform slightly better than the MWCNTs, with and without functionalization. This

can be attributed to the efficient dispersion of the CNFs compared to the MWCNTs as seen from the dispersion studies. We could speculate that this could also be due to the fact that CNFs have an imperfect molecular arrangement and may provide several sites for bonding with the matrix molecules, resulting in more effective load transfer. Also among CNFs, those with OH functionalization are observed to provide the maximum enhancement in the mechanical properties of agarose. This is also in close agreement with the results of the dispersion characterization.

4.2.4 Biocompatibility Tests - Set II

For this set the biocompatibility experiments are performed using live-dead staining of the cellular constructs as discussed in section 3.4. Similar to part A, the cells appear rounded in the three-dimensional arrangement. Hence, it is difficult to focus on them. Fig. 4.13 shows the results for the live-dead staining experiment performed on the cellular constructs. The images obtained for the live (green) and dead (red) cells are overlaid in a single image for each case. We see that the total number of cells, both live and dead, is greater in the control (2% agarose) case than the ones in which we have carbon nanomaterials. This is due to problems in imaging through the dense and opaque carbon nanomaterials as discussed in part A. Agarose, by itself is transparent and allows a clear view of the cells. WE also see that the number of dead cells is very low for all cases except 0.2% CNF. Even in the case of 0.2% CNF, there is a higher concentration of live cells compared to dead cells. Thus, we do not observe any significant toxicity effects caused by the CNMs in this set.

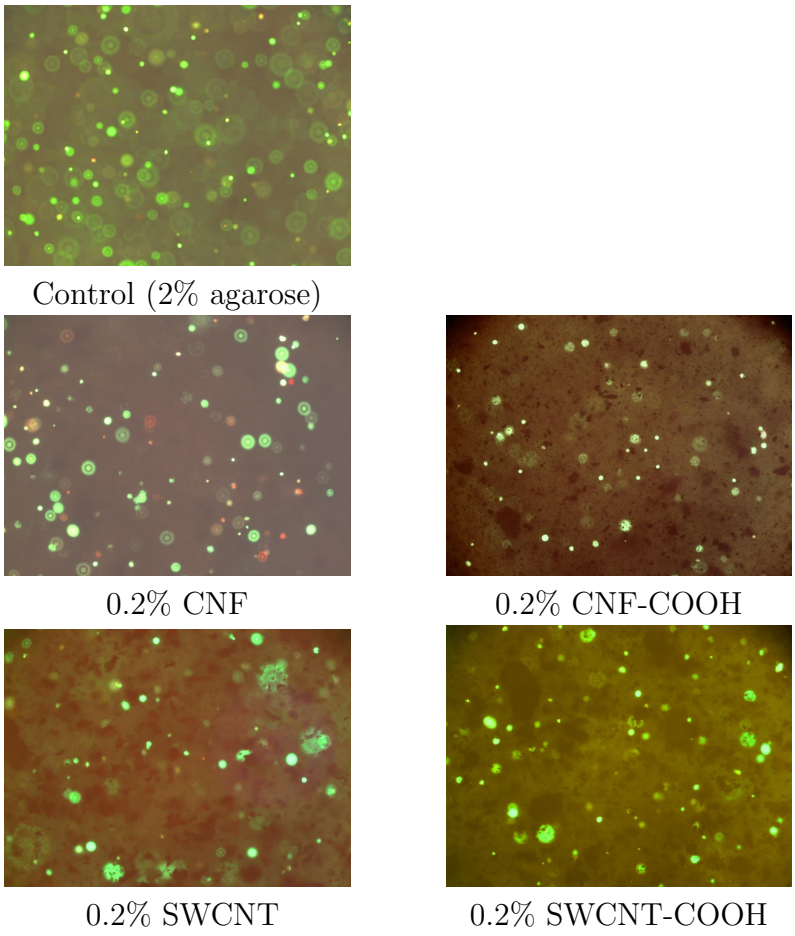

Figure 4.13: Cell viability test results showing live (green) and dead (red) cells in the composites in set II after live/dead staining (Part B).

4.2.5 Dispersion Characterization - Set II

Dispersion Characterization Using Optical Microscopy

From the dispersion characterization studies performed for set I, we found that optical microscopy is sufficient to perform a comparative assessment of the dispersion of the CNMs in agarose. Therefore, only optical microscopy studies are performed for the nanocomposites prepared in this set. Figure 4.14 shows the optical microscopy images

obtained at 400× magnification for all four nanomaterials prepared. We see that CNFs,

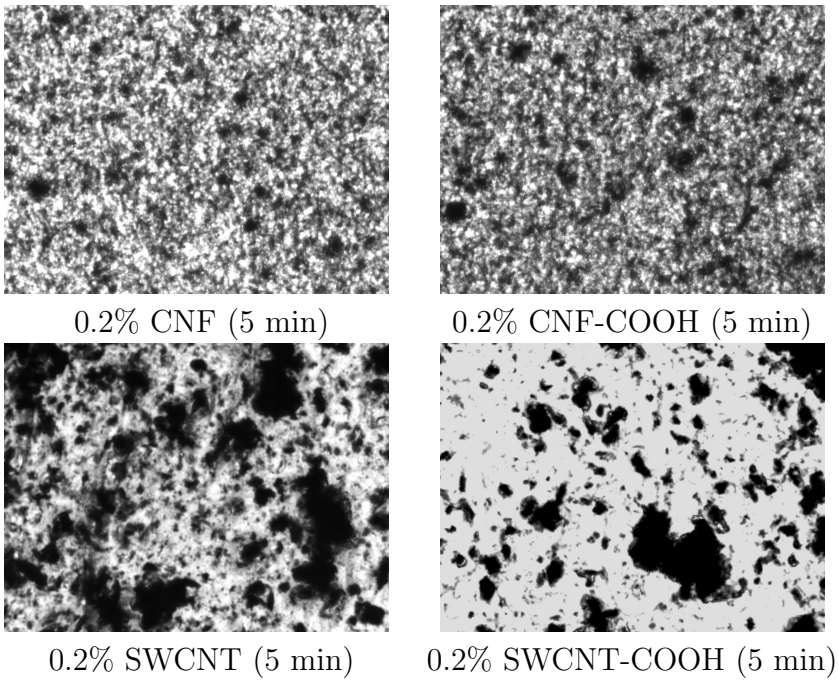

Figure 4.14: Optical microscopy images (400× magnification) of the nanocomposites in set II prepared using 5 mintues of sonication before autoclaving and 1 minute of sonication after autoclaving (Part B).

both untreated as well as COOH functionalized, disperse significantly better than the SWCNTs, untreated and COOH functionalized. This has been observed to be directly related to the mechanical properties as will be discussed in the next section.

4.2.6 Mechanical Tests - Set II

Fig. 4.15 displays the mean values and standard errors for the equilibrium nominal stress with respect to axial strain for the five materials tested. In this set too, a low variability is observed in the data as seen from the standard errors. There is significant enhancement in the mechanical stiffness for the CNF, CNF-COOH and SWCNT cases. However,

SWCNT-COOH actually has a lower initial stiffness compared to the control case. The CNF and CNF-COOH cases are clearly seen to perform better than the SWCNT and SWCNT-COOH cases. This can be attributed to the inefficient dispersion of the SWCNT and SWCNT-COOH in agarose. Our speculation that CNFs provide better load transfer from the matrix to the nanomaterials due to their imperfect molecular structure and better bonding is further supported by the results obtained for this set.

Interestingly, although COOH functionalization improves the mechanical properties of the CNF-agarose composite, it shows quite the opposite effect in the case of SWCNTs. We hypothesize that this is because COOH functionalization

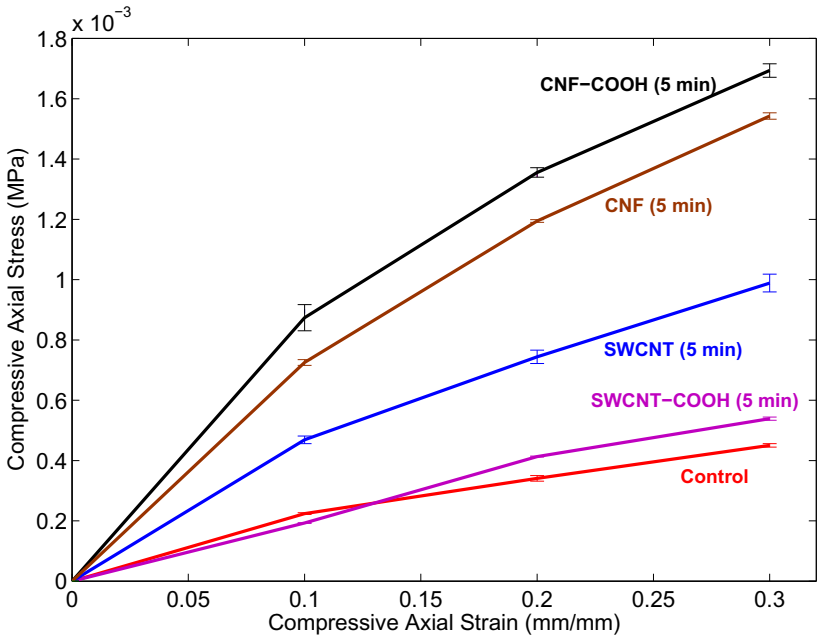

Figure 4.15: Compressive axial stress-strain data obtained from unconfined compression tests for the nanocomposites in set II (Part B).

4.2.7 Computational Modeling (Solid Phase) - Set II

The Ogden Hill potential or the Hyperfoam model is used to define the solid phase of the nanocomposites similar to part A. It was observed that $N = 1$ and $N = 2$, both provided good fits for the experimental data. However, the material parameters obtained using $N = 2$ did not always satisfy the stability criteria (see section 3.7.1). Considering that only four data points are available per specimen, this difficulty is expected. Therefore, $N = 1$ was chosen as the order for the strain energy potential. The results obtained for the curvefits are shown in Fig. 4.16. Solid lines show the computational model curve and the dots show the experimental mean for the stress-strain data. The model provides very good fits for all materials and the RMS error between the experimental values and the computational model was found to be less than 4% for all specimens.

Using the material parameters obtained from the curvefits, the initial shear and bulk

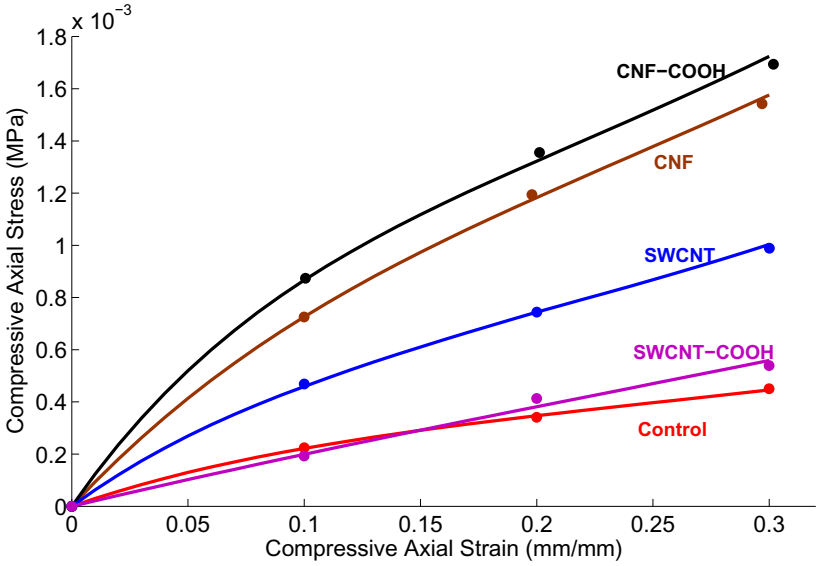

Figure 4.16: Curvefits obtained for the experimental data using the Hyperfoam material model in ABAQUS. Dots represent mean values from mechanical tests and solid lines represent the computational models for set II (Part B).

moduli, defined in equations (2.41) and (2.42) respectively, are computed for all materials. Fig. 4.17 shows their mean values and standard deviations for all the materials. The initial shear and bulk moduli show significant improvements for all cases except SWCNT-COOH, where we actually see a decrease of about a third. The CNF-COOH case shows the best improvement in the mechanical properties with an improvement in the initial shear modulus by 310.0% and in the initial bulk modulus by 328.8%.

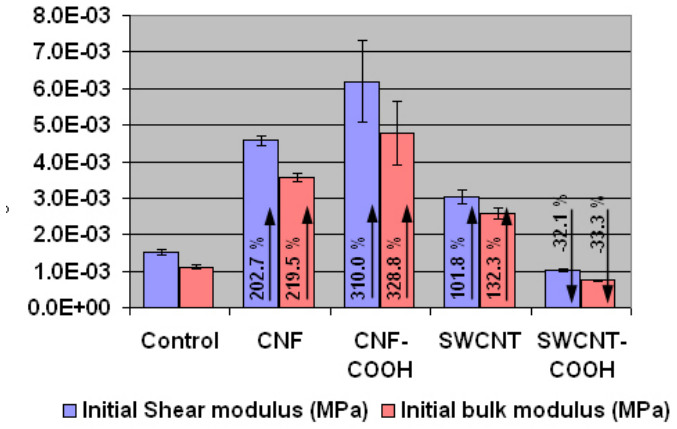

Figure 4.17: Comparison of initial shear and bulk moduli for the materials for set II (Part B).

4.2.8 Effect of Sonication Time - Set II

The effective load transfer from the matrix to the nanomaterials is subject to the proper dispersion of nanomaterials inside the matrix and the bonding between them. In order to study this, two groups of acellular constructs are prepared with two different sonication times before autoclaving. The constructs in the first group are sonicated for 1 minute before autoclaving followed by another 1 minute sonication after autoclaving and the constructs in the second group are sonicated for 5 minutes before autoclaving and 1

minute after autoclaving. The constructs from these two groups are compared with respect to dispersion and mechanical properties.

Effect of Sonication Time on Dispersion

Fig. 4.18 shows the optical microscopy images obtained for the nanocomposites prepared using 1 minute of sonication before and after autoclaving. This group is compared to that obtained using 5 minutes of sonication before autoclaving and 1 minute of sonication after autoclaving, shown in Figure 4.14. The CNF and CNF-COOH composites do not show significant differences in the dispersion quality between the two groups. The dispersion is good in both cases. However, comparison of the two groups for SWCNT and SWCNT-COOH shows significant differences in the dispersion quality, the group with 5 minutes of sonication before autoclaving is relatively effectively dispersed. However, even with 5 minutes of sonication the dispersion of SWCNT and SWCNT-COOH is still not as good as CNF and CNF-COOH.

Effect of Sonication Time on Mechanical Properties

Unconfined compression tests are performed on constructs prepared using 1 minute of sonication before autoclaving and the results are compared with the stress-strain data obtained earlier for the group with 5 minutes of sonication before autoclaving.

Fig. 4.19 shows the comparison between the equilibrium stress-strain data for CNF and CNF-COOH composites for the two cases. We see that the mechanical properties improve, although by small amounts, with the increase in sonication time. This is likely due to better dispersion and hence better load transfer from the matrix to the nanofibers.

Fig. 4.20 shows the comparison between the equilibrium stress-strain data for SWCNT

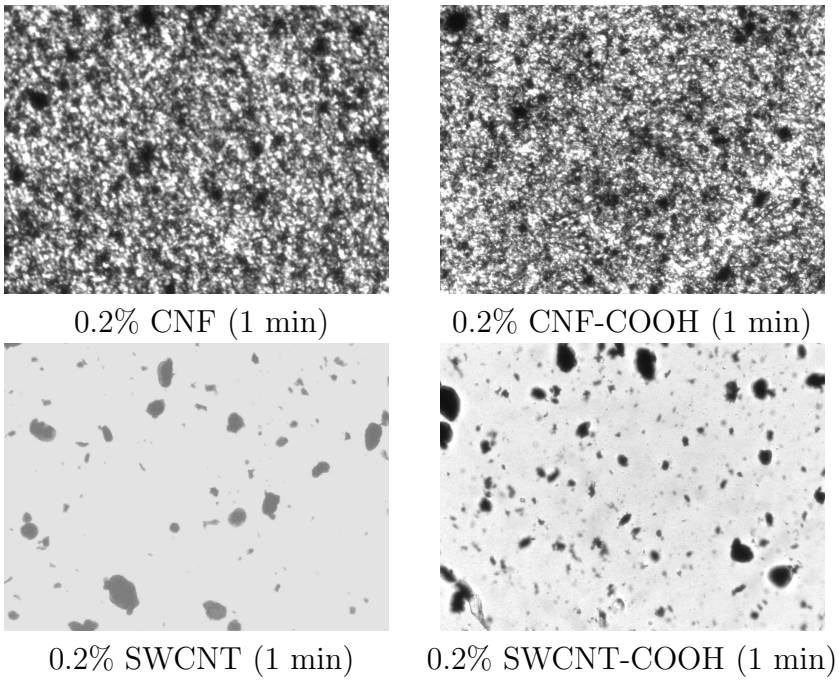

Figure 4.18: Optical microscopy images of the nanocomposites in set II prepared using 1 minute of sonication before and after autoclaving at 400× magnification (Part B).

and SWCNT-COOH composites for the two different sonication times. Here, however, that the mechanical properties of SWCNT and SWCNT-COOH worsen with increase in sonication time. We hypothesize that the very high stiffness of SWCNTs relative to the matrix material, coupled with the inefficient load transfer from the matrix to the SWCNTs, causes the SWCNTs to damage the matrix instead of reinforcing it. Better dispersion leads to more damage of the matrix and worsens the mechanical stiffness of the composite.

In summary, in part B, different types of CNMs with different kinds of functionalizations are assessed for biocompatibility, dispersion and mechanical properties. Cell viability test results suggest that agarose nanocomposites with CNF, CNF-COOH, SWCNT and SWCNT-COOH display no significant cytotoxicity with respect to rat MSCs. These

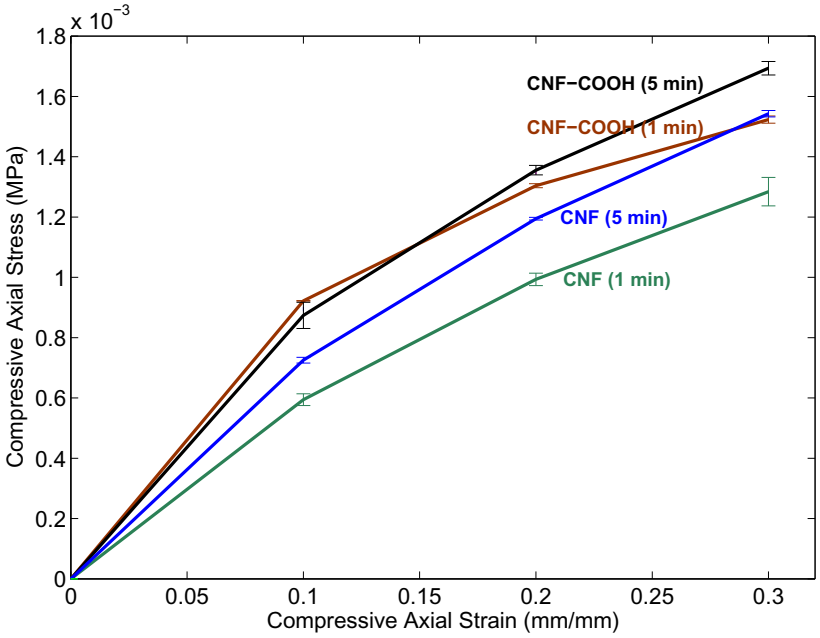

Figure 4.19: Effect of sonication time on the mechanical response of CNF and CNF-COOH in set II (Part B).

preliminary tests help us make a qualitative assessment of the biocompatibility of these nanomaterials. It is important, however, to perform a quantitative analysis of the biocompatibility in order to qualify their use in tissue engineering scaffolds. This forms a part of the future work for this research.

Dispersion characterization results obtained using optical microscopy indicate that CNF and CNF-COOH disperse more effectively in agarose compared to SWCNT and SWCNT-COOH. Due to their strong intermolecular attraction, SWCNTs tend to agglomerate resulting in poor dispersion. Stress-strain data obtained from uniaxial compression tests suggest that CNF and CNF-COOH composites have higher mechanical stiffness relative to the SWCNT and SWCNT-COOH composites. We speculate that the imperfect molecular structure of CNFs provides several sites for attachment with the matrix molecules

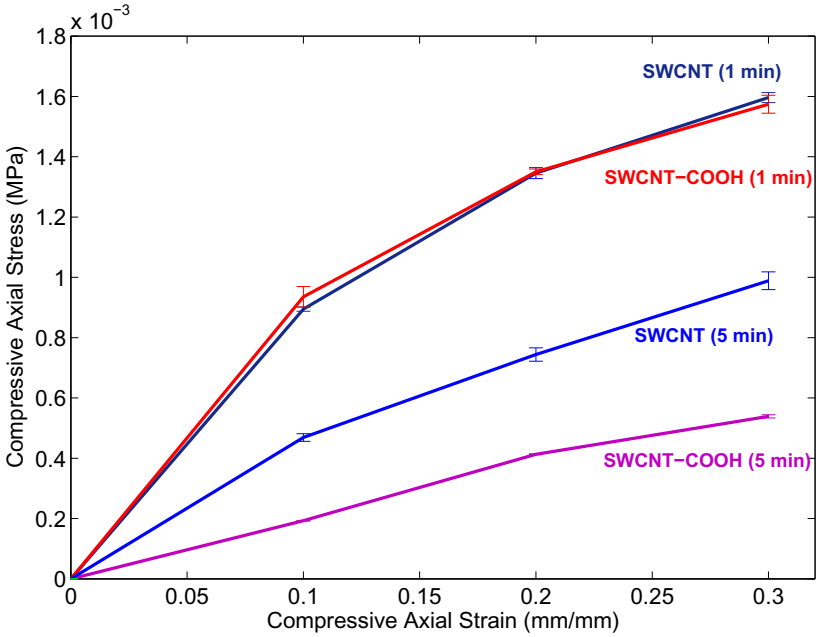

Figure 4.20: Effect of sonication time on the mechanical response of SWCNT and SWCNT-COOH in set II (Part B).

resulting in better bonding with the matrix and hence efficient load transfer from the matrix to the nanomaterials in the case of CNF and CNF-COOH composites. SWCNTs, on the other hand, do not bond well with the agarose molecules, resulting in inefficient load transfer from the matrix to the nanomaterials.

Increased sonication time results in better dispersion of the nanomaterials in agarose. Better dispersion leads to improved mechanical properties in the case of CNF and CNF-COOH composites. However, in the case of SWCNT and SWCNT-COOH composites, the mechanical properties depreciate with improved dispersion. This is counterintuitive, but it supports our earlier speculation that there is inefficient load transfer from the agarose matrix to the nanomaterials in the case of SWCNT and SWCNT-COOH composites.

The solid phase of each nanocomposite is modeled as a highly compressible hyperelastic material using the Ogden-Hill strain energy density function. The computational model provides a very good fit to experimental data. This is used to extract the initial bulk and shear moduli for quantitative comparison. It is observed that among the nanomaterials used, CNF-COOH provides the maximum enhancement in the mechanical properties when mixed with agarose at the given concentration.

4.3 Part C: Detailed Mechanical Characterization of Selected CNM Nanocomposite

The CNM type and functionalization that provide the best enhancement of the mechanical properties of agarose without compromising its biocompatibility is chosen based on the results obtained from the comparison studies performed in part B. In this section, CNFs with COOH functionalization (from set II) are studied further because they provide the best enhancement in the mechanical properties and also do not display any significant cytotoxicity as indicated by the cell viability experiments. We discuss the results obtained for the detailed mechanical characterization of the nanocomposites prepared using 0.2% (wt. CNM/wt. agarose gel) CNF-COOH along with a control case prepared with 2.0% (wt./vol. of PBS) agarose only.

4.3.1 Multistep Unconfined Compression Loading and Unloading Tests

These tests are similar to those performed in part A. However, in this case, loading is followed by unloading of the specimens as described in Chapter 3. The strain profile used for these tests is shown in Fig. 3.6. The load history data obtained for these experiments shows an interesting behavior which is discussed below.

Buoyancy Force Correction

The typical load history data obtained from the loading-unloading experiments is shown in Fig. 4.21 for one specimen. We see from the plot that the load at the end of the unloading is not zero as would be expected at zero strain. The load actually has a significant negative value at the end of unloading. This was investigated further and it was found that when the unconfined compression experiments are performed, the level of the fluid in the dish in which the specimen is placed goes down by a considerable amount due to evaporation of the fluid over the course of the experiment. This results in a decrease in the buoyant force exerted by the fluid on the indenter. This loss of fluid is significant since the unconfined compression experiments are carried out over a period of 20 hours. Thus, it is the buoyant force on the intenter that actually decreases with time and not the reaction force exerted by the specimen.

There are two possible ways to correct this problem: (a) maintain constant level of fluid in the dish throughout the unconfined compression experiment; (b) account for the loss of buoyancy force on the indenter by adding a correction to the measured load. The first approach is very difficult to implement. It is nearly impossible to prevent loss of fluid due to evaporation, since the dish cannot be covered. The second approach is not

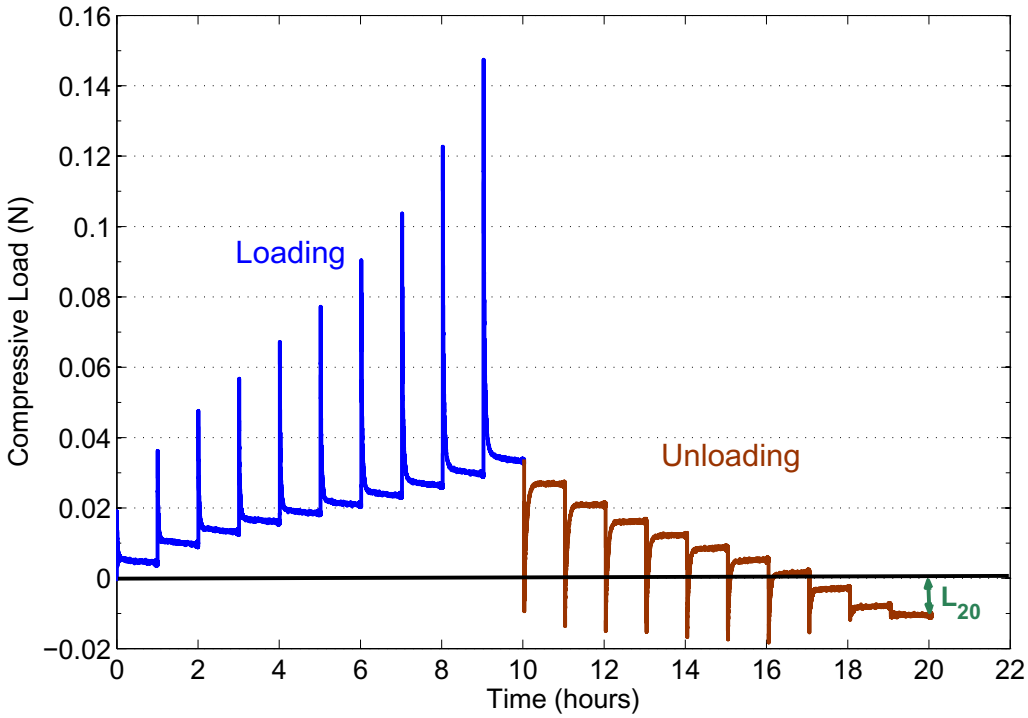

Figure 4.21: Load history data for unconfined compression loading and unloading of 0.2% CNF-COOH nanocomposite. Final load after complete unloading is negative (Part C).

very simple either. It is difficult to measure the loss of fluid continuously throughout the experiment in order to compute the buoyant force correction. However, we have developed a method that can approximate the loss of buoyant force through the course of the experiment and this can be added as a correction to the response load being measured.

It is known that the value of the load at zero strain should be zero at the end of unloading. Thus, the negative value of the response load measured at the end of the unloading cycle can be completely attributed to the loss of buoyant force. Thus, we know the change in buoyant force at the end of 20 hours. Assuming that the loss of fluid due to evaporation

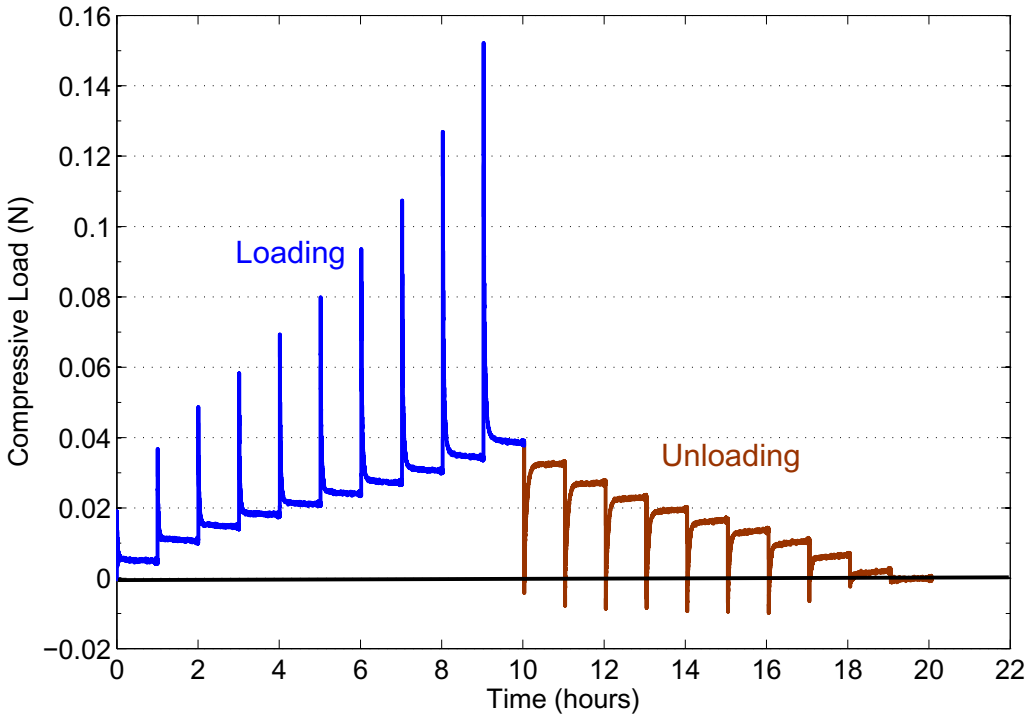

Figure 4.22: Corrected load history data for unconfined compression loading and unloading of 0.2% CNF-COOH nanocomposite (Part C).

is a linear function of time, and knowing that the buoyant force is a linear function of the height of fluid above the indenter, we can assume that the buoyant force varies linearly with time. Thus, if L_{20} denotes the loss in buoyant force at the end of 20 hours as shown in Fig. 4.21, then the linear buoyant force correction added to the response load is given by

$$BF_{corr}(t) = \frac{L_{20}}{(20)\cdot(3600)}t, \quad 0 \le t \le (20 \cdot 3600) \tag{4.1}$$

where t is the time in seconds. This correction is applied to the load versus time data and the corrected load versus time data is as shown in Fig. 4.22. It can be seen from

the figure that the buoyant force correction applied shifts the equilibrium loads to the positive side of the y-axis.

In order to justify the buoyancy force correction applied, separate experiments are performed wherein the indenter is just dipped in the fluid filled dish without any specimen and the variation of the buoyant force with respect to time is measured as the fluid evaporates for the same duration (20 hours) as required by the unconfined compression tests. The time history of the recorded load is as shown in Fig. 4.23. The loss in

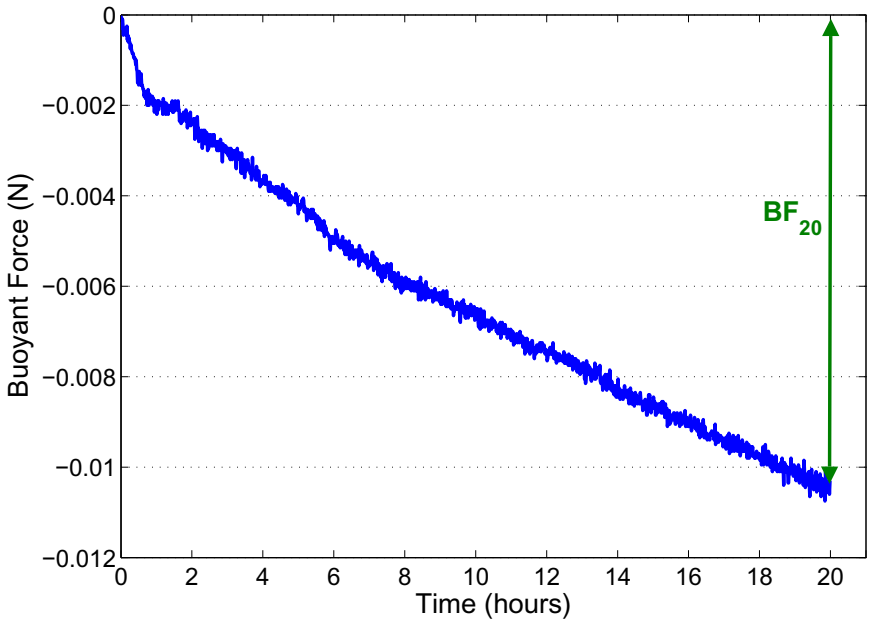

Figure 4.23: Buoyant force measurement with respect to time performed in a separate experiment (Part C).

the buoyant force at the end of 20 hours, denoted by BF_{20} in the plot, is found to be nearly equal to the correction L_{20} applied to the load history data from the unconfined compression test. This shows that the negative value of the load obtained at the end of the unloading cycle can be attributed to the decrease in the buoyant force due to fluid

evaporation. While the variation of the buoyant force with respect to time is not exactly linear, it can be approximated by a linear curve without too much loss in accuracy.

Equilibrium Stress-Strain Data for Loading and Unloading

From the corrected loading and unloading history data, the equilibrium stress is obtained for each strain increment (or decrement). Fig. 4.24 provides the mean values and the standard error for the equilibrium stress with respect to the axial strain for the control and the 0.2% CNF-COOH case. Solid lines indicate loading and dashed lines

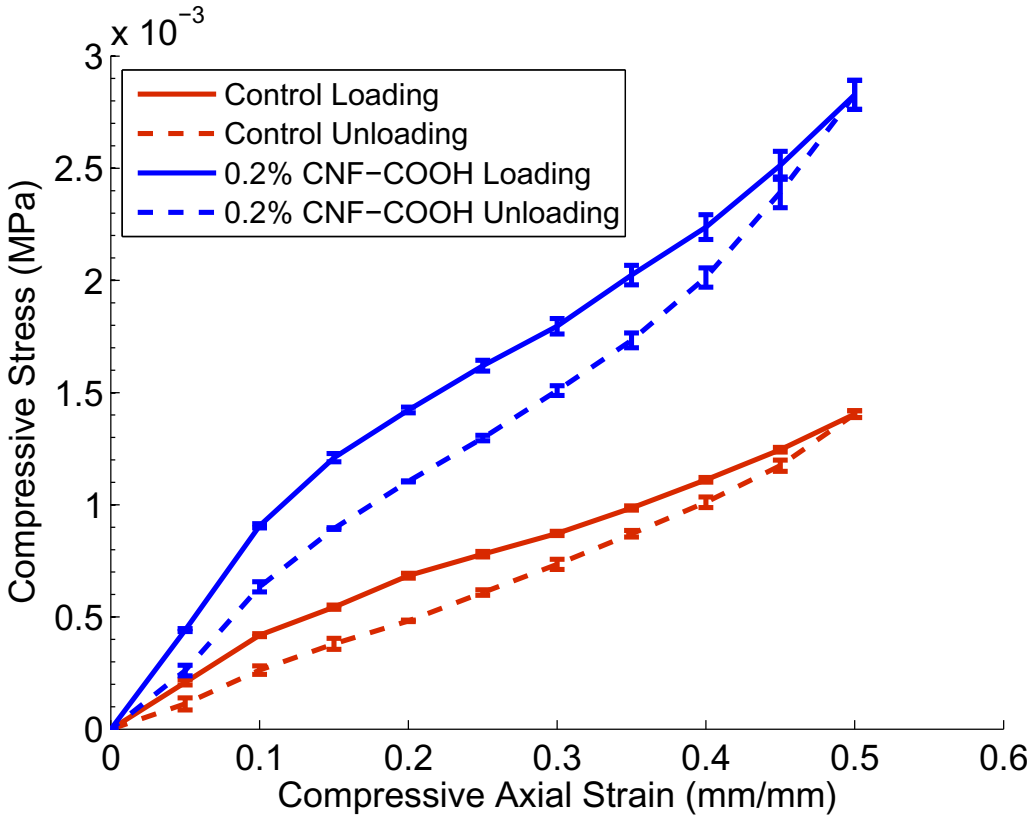

Figure 4.24: Equilibrium compressive stress vs. axial compressive strain loading and unloading data obtained from the unconfined compression tests for control and 0.2% CNF-COOH (Part C).

indicate unloading. As in parts A and B, the equilibrium stress-strain loading curves show the characteristic elastomeric behaviour. Three specimens ($n = 3$) are tested for the control case and five specimens ($n = 5$) are tested for the 0.2% CNF-COOH case. The errorbar values indicate low variability in the data. At the end of the unloading there is no residual strain in any of the specimens indicating that plastic deformation is not a concern for agarose and its nanocomposites. The unloading curve, however, follows a different path than the loading curve. This hysteresis is not time (or rate) dependent since the stress values considered here are equilibrium values and the stress-strain data obtained is for a quasi-static deformation.

It is important to note that it is unlikely that this hysteresis is due to the Mullin's effect. This is because the specimens are preconditioned up to 50% strain at the beginning of the experiments. Also, the specimens were reloaded after one loading-unloading cycle and it was observed that the second loading curve follows the same path as the first loading curve and not the first unloading curve. Thus, Mullin's effect is ruled out in this case.

It is clear that during the loading-unloading cycle, there is some energy dissipation through recoverable damage. This damage is recovered at the end of the resulting in no residual strains. It is possible that the biphasic material displays viscoelasticity on a different time scale such that the equilibrium is reached after a very long duration relative to the relaxation and recovery times used in the unconfined compression experiments. Due to this the actual equilibrium loads for the solid phase would be different from the ones obtained in the experiments. With the actual equilibrium loads the loading and the unloading stress-strain curves would actually coincide.

In order to model the equilibrium stress-strain data obtained from the loading-unloading

experiments, we model the material using the pseudo-elasticity theory discussed in Chapter 2. This kind of behavior is also found in particle reinforced rubbers [28]. The computational modeling is discussed later in section 4.3.3.

4.3.2 Confined Compression Creep Tests

Specimens used for the unconfined compression tests are reused for the confined compression creep tests. This is because we intend to use the constitutive relationships developed for the solid phase of the individual specimens using the results of the unconfined compression experiments into the optimization algorithm used for modeling the permeability. The procedure used for these experiments is exactly identical to that used in part A and is described in section 3.5.2. The strain history data is obtained by post-processing the displacement history data. Fig. 4.25 shows the representative strain history data obtained for the control and the 0.2% CNF-COOH specimens. The control specimens reach equilibrium at a much faster rate (typically within 200 s) compared to the CNF-COOH specimens (typically within 2000 s). This intuitively suggests that the permeability of agarose is higher than that of the CNF-COOH nanocomposite. This is verified by the model developed for the permeability in the next section. Also, as expected, the equilibrium strain is higher, although slightly, for the control case compared to the CNF-COOH nanocomposite since the nanocomposite is stiffer than agarose.

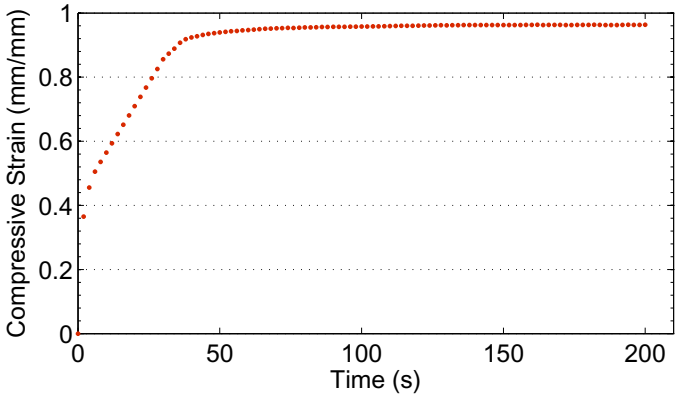

(a) Control

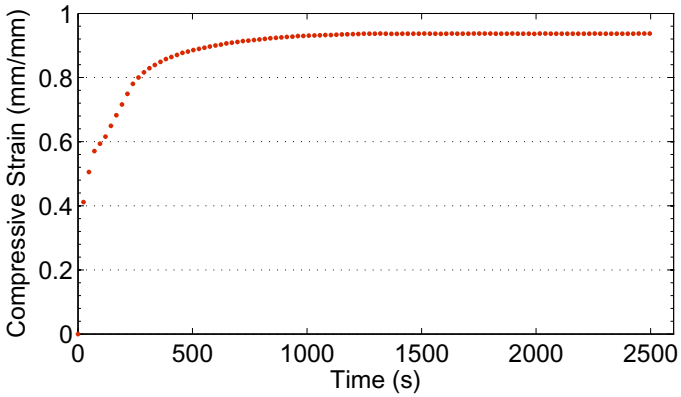

(b) 0.2% CNF-COOH

Figure 4.25: Representative strain history data obtained from confined compression experiments for (a) a control specimen and (b) a 0.2% CNF-COOH specimen

4.3.3 Computational Modeling of Agarose and the Agarose-CNF-COOH nanocomposite

The results of the mechanical testing are used to develop a robust computational model for agarose and the agarose-CNF-COOH nanocomposite with a constitutive description of the solid phase based on the equilibrium stress-strain data from the unconfined compression tests and a strain-dependent permeability definition for the fluid phase based

on the strain history data obtained from the confined compression creep tests.

Solid Phase Material Properties

As discussed in part A, the Ogden-Hill potential or the Hyperfoam model [41] defined in ABAQUS is the most suitable model to describe the loading stress-strain data. The lateral deformation data is obtained from the photographs of the specimens taken at each equilibrium point similar to part A. The value of the order N for the Ogden model chosen is 2. This gives the best fit for all specimens with a very low root mean square (RMS) error (less than 3%). The pseudo-elastic model is used to describe the unloading data and the procedure for obtaining the material parameters is described in section 3.7.1.

Figure 4.26 shows the comparisons of the mean values of the experimental data and the finite element model for the control case and the CNF-COOH nanocomposite. The dots represent mean values of equilibrium stresses obtained from experiments and solid lines represent the finite element model predictions. Clearly, the model provides an excellent fit over the loading data.

Table 4.3 tabulates the material parameters μ_i, α_i and β_i obtained for the mean experimental data. ABAQUS provides material stability information in addition to material parameters. The material models for all specimens are found to be stable at least within the mode of the deformation for which it is tested (uniaxial compression). Using the material model parameters μ_i, α_i and β_i, the initial shear and bulk moduli are determined as given by equations (2.41) and (2.42). These are reported in Table 4.4. The mean of the properties with standard deviations and the properties of mean (as discussed in part

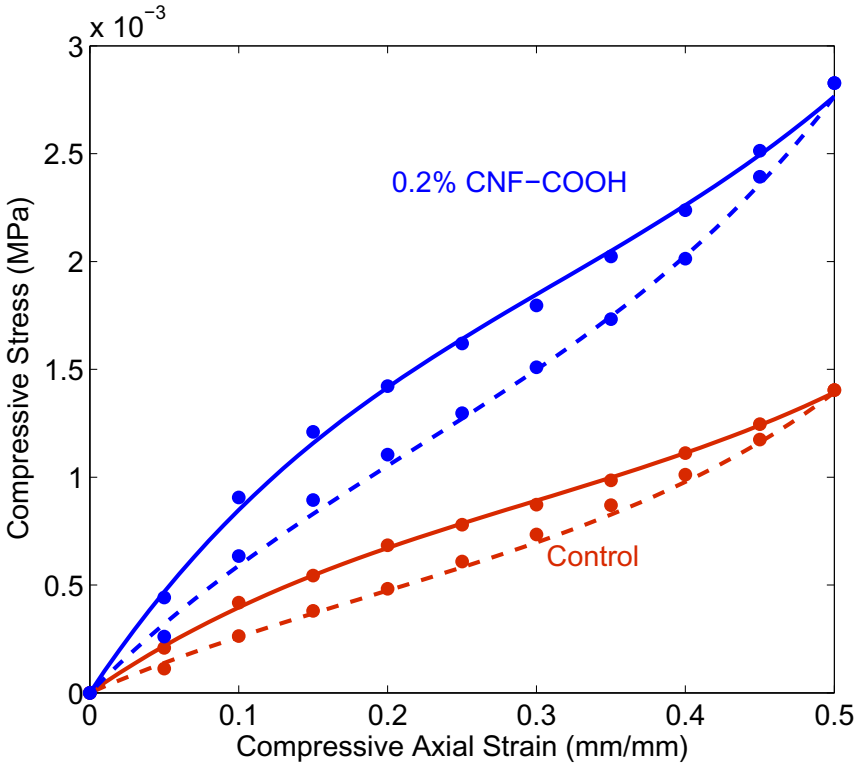

Figure 4.26: Curve-fitting the pseudo-elastic material model over equilibrium compressive stress versus axial compressive strain loading-unloading data obtained from the unconfined compression tests for control and 0.2% CNF-COOH (Part C).

Table 4.3: Material parameters μ_i, α_i and β_i obtained for the mean data (PoM) for the solid phase from curve-fitting (part C).

	i	μ_i	α_i	β_i
Control	1	2.21E-03	7.26	2.82E-02
(0% CNF-COOH)	2	-1.33E-04	3.25	-3.01E+00
0.2% CNF-COOH	1	4.77E-03	7.19	8.47E-03
	2	-3.40E-04	3.71	-3.14E+00

Table 4.4: Properties of mean and mean of properties for the solid phase obtained from curve-fitting (Part C).

		Properties of Mean	Mean of Properties (Mean±SD)
Control (0% CNF-COOH)	μ_0 (MPa)	2.08E-03	2.05E-03 ± 5.03E-04
	κ_0 (MPa)	2.31E-03	2.44E-03 ± 6.71E-04
	r	2.79E-03	5.38E-03± 2.07E-03
	m (MPa)	3.69E-01	2.87E-01 ± 1.14E-01
0.2% CNF-COOH	μ_0 (MPa)	4.43E-03 (112.98% ↑)	4.45E-03 ± 1.62E-04
	κ_0 (MPa)	5.17E-03 (123.81% ↑)	5.26E-03 ± 3.96E-04
	r	4.05E-03	4.78E-03 ± 8.45E-04
	m (MPa)	5.95E-01	5.80E-01 ± 9.72E-02

A) are tabulated. The unloading data is used to find the parameters r and m in the definition of η given in equation (2.58) using the procedure described in section 3.7.1. Table 4.4 reports the values obtained for these parameters as properties of mean and mean of properties with standard deviations.

Strain-Dependent Permeability

The strain history data obtained from the confined compression experiments is used to obtain the fluid phase permeability constants. The governing differential equations are solved using a finite difference approximation and the optimization is carried out using the Amoeba algorithm similar to part A. Fig. 4.27 provides the comparison between the solution obtained from the finite difference approximation and the experimental data for the control case and the 0.2% CNF-COOH case. The experimental data is shown using dots and the numerical model is shown using a solid line. Clearly, the numerical model

Table 4.5: Mean values and standard deviations of the strain dependent permeability parameters k_0 and M (Part C).

	k_0 (Mean ± SD) (m^4/Ns)	M (Mean ± SD)
Control (0% CNF-COOH)	4.39E-10 ± 1.89E-10	4.587 ± 1.744
0.2% CNF-COOH	5.50E-10 ± 2.52E-10	11.254 ± 1.116

provides a very good fit over the experimental data.

As in part A, the parameter κ is set to zero and the other two paramters k_0 and M (see equation (2.66) are determined using the optimization algorithm. The optimization problem is highly nonlinear and unconstrained, and the solution is highly sensitive to the initial values provided for the permeability parameters k_0 and M, and non-unique. Table 4.5 provides the mean values and standard deviations for the parameters k_0 and M for both materials tested. Using these mean values, the permeability of the materials is completely defined. Figure 4.28 shows plots of the permeabilities of both materials with respect to compressive strain up to a strain of 99% in confined compression for the mean parameters in table 4.5. At higher strains, agarose has a higher permeability compared to the CNF-COOH nanocomposite. For example, at 90% strain, the permeability of agarose is 5.57E-11 m^4/Ns, while that of the CNF-COOH nanocomposite is 3.48E-12 m^4/Ns. Thus, there is an order of magnitude difference in the permeabilities at higher strains. This explains why the time taken by the control specimens to attain equilibrium is a small fraction of the time taken by the CNF-COOH nanocomposite specimens to reach equilibrium in confined compression.

In summary, in part C, a protocol is developed for the detailed mechanical testing of the

agarose-CNF-COOH composite in the form of multi-step loading and unloading unconfined compression tests and confined compression creep tests. Constitutive descriptions are obtained for the solid phase based on the pseudo-elasticity theory and the fluid phase in the form of strain-dependent permeability. The models developed match very closely with the experimental results.

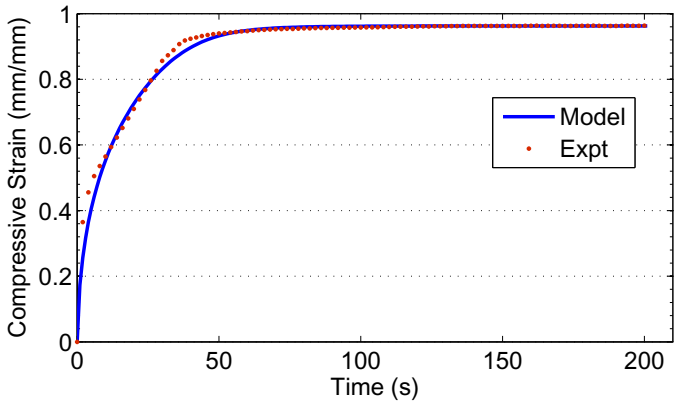

(a) Control

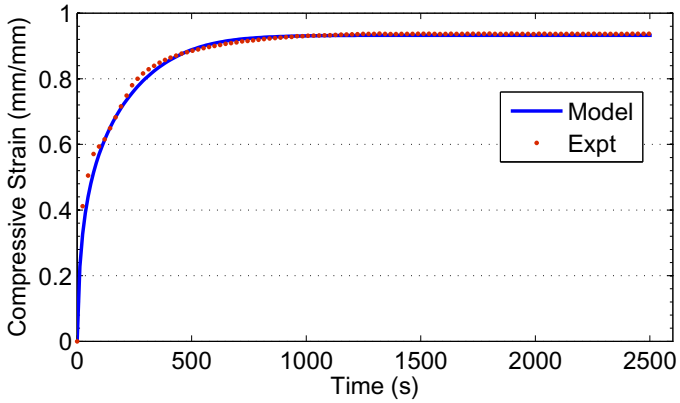

(b) 0.2% CNF-COOH

Figure 4.27: Comparisons between the numerical model and experimental strain history data for the confined compression experiments for (a) a representative control specimen and (b) a representative 0.2% CNF-COOH specimen (Part C).

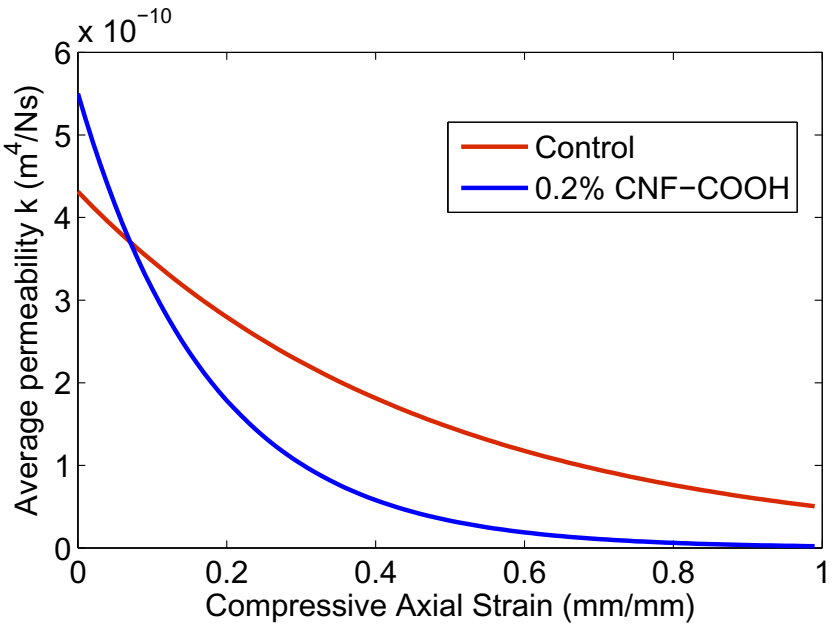

Figure 4.28: Permeability versus strain for the control and the 0.2% CNF-COOH case using the mean parameters from Table 4.5 (Part C).

Chapter 5

Conclusions and Future Work

In this chapter, we provide some concluding remarks based on the results obtained and the discussions in Chapter 4. We also provide suggestions for future work for this research.

5.1 Conclusions

As stated in section 1.3, this research has two broad aspects. The first deals with application of nanotechnology to tissue engineering in order to develop better scaffold materials and the second focuses on the mechanical characterization and computational modeling of soft porous biomaterials and their composites as biphasic materials. The specific research objectives were laid down for these two aspects in section 1.3.

The first research objective in the context of assessing the application of agarose and its nanocomposites as tissue engineering scaffolds, was to determine the effect of CNM concentration on the mechanical properties and biocompatibility of agarose. This study is performed in part A using carbon nanofibers (CNFs) supplied by the Nanoworld and

Smart Materials and Devices Laboratory at the University of Cincinnati. We find that the addition of CNFs enhances the mechanical properties of agarose in a concentration-dependent manner. Preliminary biocompatibility (cell viability) tests also show that these materials do not display any significant cytotoxicity to mice chondrocytes. It is important, however, to validate this finding through quantitative analysis techniques to assess the biocompatibility.

The second research objective in the context of assessing the application of agarose and its nanocomposites as tissue engineering scaffolds, was to determine the type and functionalization of CNM that most improves the mechanical integrity of agarose without adversely affecting its biocompatibility. This is addressed in the study in part B. Different types of CNMs with various functionalizations are obtained from two sources. Agarose nanocomposites prepared with these nanomaterials are subjected to biocompatibility testing, dispersion characterization and mechanical testing. Our results show that, in general, CNFs (untreated and functionalized) disperse more effectively compared to SWCNTs and MWCNTs (both untreated and functionalized). CNFs also provide better enhancement in the mechanical properties of agarose. We speculate that due to the imperfect molecular structure of CNFs, they provide several sites for bonding with the matrix molecules, resulting in better load transfer and stronger reinforcement of the matrix material. Again our preliminary biocompatibility tests show that CNFs and SWCNTs (untreated and COOH functionalized) do not cause any significant cytotoxicity to rat MSCs.

A major conclusion from the study in part B is that CNF-COOH provides the most mechanical enhancement in the mechanical properties of agarose without compromising its biocompatibility. This CNM is used for more detailed mechanical characterization

and computational modeling in part C.

The third research objective was to develop a standard method for the mechanical characterization of agarose and its nanocomposites. This study is performed in parts A, B and C. Agarose and its nanocomposites are modeled as biphasic materials. It is necessary to model both the solid phase and fluid phase to accurately predict the combined behavior of the two phases. Multi-step unconfined compression stress-relaxation tests are designed in order to model the solid phase from the equilibrium response of the biphasic material and single step confined compression creep tests are designed in order to use the transient data to model the fluid phase permeability. The mechanical testing protocols developed in part C can be used for developing robust numerical description of both phases of the biphasic materials.

The fourth and the last research objective was the develop a macro-scale material model for agarose and its nanocomposites based on the nonlinear biphasic theory. Using the mechanical testing protocols developed for the complete material characterization of agarose and its nanocomposites as biphasic materials, phenomenological constitutive models are obtained for the solid phase and the fluid phase permeability. A pseudo-elastic model coupled with a compressible hyperelastic definition for the loading phase is used for the solid phase constitutive description and a strain-dependent permeability is used for the fluid phase according to the nonlinear biphasic theory. The macro-scale biphasic material models developed here for agarose and its nanocomposites agree very closely with the experimental results.

The major accomplishments for this research are as follows.

- Novel biomaterials in the form of carbon nanomaterial (CNM) based composites of agarose are developed for use in tissue engineering scaffolds.

- The effect of important parameters, such as, the concentration of the CNMs, the type of the CNMs and the functionalization of the CNMs on the mechanical properties and the biocompatibility of the nanocomposites of agarose is established through a series of experiments. The following are the specific accomplishments in this part of the study
  - The effect of CNF concentration on the mechanical properties of agarose is assessed through rigourous mechanical testing and computational modeling. It is found that the addition of CNFs improves the mechanical strength of agarose in a concentration dependent manner.
  - The effect of CNF concentration on the biocompatibility of agarose is assessed through cell viability tests and no significant cytotoxicity is observed.
  - The effect of CNM type and functionalization on the mechanical properties is studied through mechanical testing and computational modeling using various types of CNMs (such as CNFs, SWCNTs and MWCNTs) from two different sources.
  - Comparison studies are also performed to assess the effect to CNM type and functionalization on the biocompatibility of the agarose-CNM nanocomposties based on cell viability studies
  - The quantitative comparison is successfully used to identify the CNM type and functionalization that give the best enhancement in mechanical properties of agarose without compromising its biocompatibility. The biomaterial and type is identified as CNF with COOH functionalization.
- Mechanical testing protocols are developed for robust computational modeling of

the biomaterials as biphasic materials. Mechanical tests are designed such that the results can be used to develop constitutive equations for the fluid and the solid phase. Multi-step unconfined compression stress-relaxation tests are used to model the solid phase constitutive equations and single-step confined compression creep tests are used to model the fluid phase permeability.

- Using the mechanical test data, computational models are developed based on the biphasic theory for agarose and its nanocomposites. A pseudo-elastic model is developed for modeling the solid phase in loading and unloading and a strain-dependent permeability is used for the fluid phase constitutive description. The computational model fits very closely on the experimental data.

5.2 Future Work

The following is a list of suggestions for future work for this research.

- Quantitative analysis methods need to be performed in order to better assess the biocompatibility of the nanocomposites. It is also essential to test cell migration, proliferation and differentiation in these materials for effective use of these nanomaterials as tissue engineering scaffolds.

- The dispersion of the nanomaterials in the agarose matrix can also be assessed quantitatively using techniques such as small angle light scattering (SALS) or small angle X-ray scattering (SAXS)

- Although, carbon nanomaterials are promising reinforcements for tissue engineering scaffolds, their non-biodegradability is an issue. Therefore, these materials can

only be used in small concentrations in specific tissues. The use of other biodegradable nanomaterials as reinforcements for bio-scaffolds needs to be investigated.

- The use of CNMs as reinforcements can be investigated for biomaterials other than agarose.
- The pseudo-elasticity model developed in this research can be made validated for longer mechanical tests with repeated loading and unloading cycles.
- Ultrafiltration experiments can be performed for direct measurement of the strain-dependent permeability of the biphasic materials.

Bibliography

[1] http://researchcompliance.uc.edu/iacuc.

[2] http://www1.amershambiosciences.com.

[3] http://www.min.uc.edu/nanoworldsmart.

[4] P. M. Ajayan. Nanotubes from carbon. *Chemical Reviews*, 99(7):1787–1799, Jul 1999.

[5] P. M. Ajayan, L. S. Schadler, C. Giannaris, and A. Rubio. Single-walled carbon nanotube-polymer composites: strength and weakness. *Advanced Materials*, 12(10):750–753, May 2000.

[6] A. Allaoui, S. Bai, H. M. Cheng, and J. B. Bai. Mechanical and electrical properties of a MWNT/epoxy composite. *Composites Science and Technology*, 62(15):1993–1998, 2002.

[7] C. G. Armstrong, W. M. Lai, and V. C. Mow. An analysis of the unconfined compression of articular cartilage. *Journal of Biomechanical Engineering*, 106(2):165–173, May 1984.

[8] A. C. Aufderheide and K. A. Athanasiou. Comparison of scaffolds and culture conditions for tissue engineering of the knee meniscus. *Tissue Engineering*, 11(7-8):1095–1104, Jul-Aug 2005.

[9] A. H. Barber, S. R. Cohen, and H. D. Wagner. Measurement of carbon nanotube-polymer interfacial strength. *Applied Physics Letters*, 82(23):4140, 2003.

[10] M. J. Biercuk, M. C. Llaguno, M. Radosavljevic, J. K. Hyun, A. T. Johnson, and J. E. Fischer. Carbon nanotube composites for thermal management. *Applied Physics Letters*, 80(15):2767–2769, Apr 2002.

[11] E. Bilgili. Restricting the hyperelasticmodels for elastomers basedon some thermodynamical, mechanical, and empirical criteria. *Journal of Elastomers and Plastics*, 36(2):159, 2004.

[12] R. M. Bowen. Incompressible porous media models by use of the theory of mixtures. *International Journal of Engineering Science*, 18:1129–1148, 1980.

[13] R. M. Bowen. Compressible porous media models by use of the theory of mixtures. *International Journal of Engineering Science*, 20:697–735, 1982.

[14] H. Bubert, S. Haiber, W. Brandl, G. Marginean, M. Heintze, and V. Brser. Characterization of the uppermost layer of plasma-treated carbon nanotubes. *Diamond & Related Materials*, 12(3-7):811–815, 2003.

[15] M. D. Buschmann, Y. A. Gluzband, A. J. Grodzinsky, J. H. Kimura, and E. B. Hunziker. Chondrocytes in agarose culture synthesize a mechanically functional extracellular matrix. *Journal of Orthopaedic Research*, 10(6):745–758, Nov 1992.

[16] D. L. Butler, S. A. Goldstein, and F. Guilak. Functional tissue engineering: The role of biomechanics. *Journal of Biomechanical Engineering*, 122:570–575, 2000.

[17] E. Charriere, J. Lemaitre, and P. Zysset. Hydroxyapatite cement scaffolds with controlled macroporosity: fabrication protocol and mechanical properties. *Biomaterials*, 24(5):809–817, Feb 2003.

[18] Y. K. Choi, K. Sugimoto, S. M. Song, Y. Gotoh, Y. Ohkoshi, and M. Endo. Mechanical and physical properties of epoxy composites reinforced by vapor grown carbon nanofibers. *Carbon*, 43(10):2199–2208, 2005.

[19] Y. K. Choi, K. I. Sugimoto, S. M. Song, and M. Endo. Mechanical and thermal properties of vapor-grown carbon nanofiber and polycarbonate composite sheets. *Materials Letters*, 59(27):3514–3520, 2005.

[20] H. Dai. Carbon nanotubes: synthesis, integration, and properties. *Accounts of Chemical Research*, 35(12):1035–1044, August 2002.

[21] R. de Boer. Highlights in the historical development of the porous media theory: Toward a consistent macroscopic theory. *Applied Mechanics Reviews*, 49(4):201–261, 1996.

[22] R. de Boer. *Theory of Porous Media. Highlights in Historical Development and Current State*. Springer-Verlag, Berlin, 2000.

[23] M. R. DiSilvestro and J. K. Suh. A cross-validation of the biphasic poroviscoelastic model of articular cartilage in unconfined compression, indentation, and confined compression. *Journal of Biomechanics*, 34(4):519–525, Apr 2001.

[24] M. R. DiSilvestro and J. K. Suh. Biphasic poroviscoelastic characteristics of proteoglycan-depleted articular cartilage: simulation of degeneration. *Annals of Biomedical Engineering*, 30(6):792–800, Jun 2002.

[25] M. R. DiSilvestro, Q. Zhu, and J. K. Suh. Biphasic poroviscoelastic simulation of the unconfined compression of articular cartilage: Ii–effect of variable strain rates. *Journal of Biomechanical Engineering*, 123(2):198–200, Apr 2001.

[26] M. R. DiSilvestro, Q. Zhu, M. Wong, J. S. Jurvelin, and J. K. F. Suh. Biphasic poroviscoelastic simulation of the unconfined compression of articular cartilage isimultaneous prediction of reaction force and lateral displacement. *Journal of Biomechanical Engineering*, 123:191197, 2001.

[27] P. S. Donzelli, L. M. Gallo, R. L. Spilker, and S. Palla. Biphasic finite element simulation of the tmj disc from in vivo kinematic and geometric measurements. *Journal of Biomechanics*, 37(11):1787–1791, Nov 2004.

[28] A. Dorfmann and RW Ogden. A pseudo-elastic model for loading, partial unloading and reloading of particle-reinforced rubber. *International Journal of Solids and Structures*, 40(11):2699–2714, 2003.

[29] A. Fujiwara, R. Iijima, H. Suematsu, H. Kataura, Y. Maniwa, S. Suzuki, and Y. Achiba. Local electronic transport through a junction of swnt bundles. *Physica B*, 323(1):227–229, 2002.

[30] R. Haggenmueller, H. H. Gommans, A. G. Rinzler, J. E. Fischer, and K. I. Winey. Aligned single-wall carbon nanotubes in composites by melt processing methods. *Chemical Physics Letters*, 330(3-4):219–225, 2000.

[31] Balakrishna Haridas. *Anisotropic poro-hyperelastic constitutive models for soft connective tissues: application to the study of age and stress modulated fibrocartilage metaplasia in tendons*. PhD thesis, University of Cincinnati, 2001.

[32] S. Hartmann. Parameter estimation of hyperelasticity relations of generalized polynomial-type with constraint conditions. *International Journal of Solids and Structures*, 38(44-45):7999–8018, 2001.

[33] W. C. Hayes, L. M. Keer, G. Herrmann, and L. F. Mockros. A mathematical analysis for indentation tests of articular cartilage. *Journal of Biomechanics*, 5(5):541–551, Sep 1972.

[34] P. H. M. Hoet, A. Nemmar, and B. Nemery. Health impact of nanomaterials? *Nature Biotechnology*, 22(1):19–19, Jan 2004.

[35] S. J. Hollister, R. D. Maddox, and J. M. Taboas. Optimal design and fabrication of scaffolds to mimic tissue properties and satisfy biological constraints. *Biomaterials*, 23(20):4095–4103, Oct 2002.

[36] M. H. Holmes. Mixture theories for mechanics of biological tissues, 1995.

[37] M. H. Holmes and V. C. Mow. The nonlinear characteristics of soft gels and hydrated connective tissues in ultrafiltration. *Journal of Biomechanics*, 23(11):1145–1156, 1990.

[38] G. A. Holzapfel. *Nonlinear Solid Mechanics: A Continuum Approach for Engineering*. John Wiley & Sons, New York, 2000.

[39] R. A. Horch, N. Shahid, A. S. Mistry, M. D. Timmer, A. G. Mikos, and A. R. Barron. Nanoreinforcernent of poly(propylene fumarate)-based networks with surface modified alumoxane nanoparticles for bone tissue engineering. *Biomacromolecules*, 5(5):1990–1998, Sep-Oct 2004.

[40] J. D. Humphrey. Continuum biomechanics of soft biological tissues. *Royal Society of London Proceedings Series A*, 459(2029):3–46, 2003.

[41] ABAQUS Inc. Abaqus Theory Manual, version 6.5. *Providence, RI*, 2005.

[42] T. A. N. Kelly, K. W. Ng, C. C. B. Wang, G. A. Ateshian, and C. T. Hung. Spatial and temporal development of chondrocyte-seeded agarose constructs in free-swelling and dynamically loaded cultures. *Journal of Biomechanics*, 39(8):1489–1497, 2006.

[43] G. E. Kempson, M. A. Freeman, and S. A. Swanson. The determination of a creep modulus for articular cartilage from indentation tests of the human femoral head. *Journal of Biomechanics*, 4(4):239–250, Jul 1971.

[44] S. Khan. Carbon nanotube based nanocomposite fibril for cartilage regeneration. Master's thesis, Drexel University, 2002.

[45] H. Koerner, G. Price, N. A. Pearce, M. Alexander, and R. A. Vaia. Remotely actuated polymer nanocomposites - stress-recovery of carbon-nanotube-filled thermoplastic elastomers. *Nature Materials*, 3(2):115–120, Feb 2004.

[46] R. J. Kuriger, M. K. Alam, D. P. Anderson, and R. L. Jacobsen. Processing and characterization of aligned vapor grown carbon fiber reinforced polypropylene. *Composites Part A: Applied Science and Manufacturing*, 33(1):53–62, 2002.

[47] W. M. Lai and V. C. Mow. Drag-induced compression of articular cartilage during a permeation experiment. *Biorheology*, 17(1-2):111–123, 1980.

[48] C. W. Lam, J. T. James, R. McCluskey, and R. L. Hunter. Pulmonary toxicity of single-wall carbon nanotubes in mice 7 and 90 days after intratracheal instillation. *Toxicological Sciences*, 77(1):126–134, Jan 2004.

[49] R. Langer and J. P. Vacanti. Tissue engineering. *Science*, 260(5110):920–926, May 1993.

[50] A. S. P. Lin, T. H. Barrows, S. H. Cartmell, and R. E. Guldberg. Microarchitectural and mechanical characterization of oriented porous polymer scaffolds. *Biomaterials*, 24(3):481–489, Feb 2003.

[51] S. S. Lo, R. L. Mauck, S. L. Seyhan, G. D. Palmer, V. C. Mow, and C. T. Hung. Mechanical loading modulates gene expression in chondrocyte-seeded agarose hydrogels. *Advances in Bioengineering, BED*, 51:219–292, 2001.

[52] K. Lozano and E. V. Barrera. Nanofiber-reinforced thermoplastic composites. i. thermoanalytical and mechanical analyses. *Journal of Applied Polymer Science*, 79(1):125–133, 2001.

[53] R. A. MacDonald, B. F. Laurenzi, G. Viswanathan, P. M. Ajayan, and J. P. Stegemann. Collagen-carbon nanotube composite materials as scaffolds in tissue engineering. *Journal of Biomedical Materials Research Part A*, 74(3):489–496, Sep 1 2005.

[54] A. F. Mak, W. M. Lai, and V. C. Mow. Biphasic indentation of articular cartilage–I. theoretical analysis. *Journal of Biomechanics*, 20(7):703–714, 1987.

[55] J. M. Mansour and V. C. Mow. The permeability of articular cartilage under compressive strain and at high pressures. *The Journal of Bone and Joint Surgery - American Volume*, 58(4):509–516, Jun 1976.

[56] A. Maroudas, P. Bullough, S. A. Swanson, and M. A. Freeman. The permeability of articular cartilage. *The Journal of Bone and Joint Surgery - British Volume*, 50(1):166–177, Feb 1968.

[57] M. P. Mattson, R. C. Haddon, and A. M. Rao. Molecular functionalization of carbon nanotubes and use as substrates for neuronal growth. *Journal of Molecular Neuroscience*, 14(3):175–182, Jun 2000.

[58] R. L. Mauck, C. T. Hung, and G. A. Ateshian. Modeling of neutral solute transport in a dynamically loaded porous permeable gel: implications for articular cartilage biosynthesis and tissue engineering. *Journal of Biomechanical Engineering*, 125(5):602–614, Oct 2003.

[59] R. L. Mauck, M. A. Soltz, C. C. B. Wang, D. D. Wong, P. H. G. Chao, W. B. Valhmu, C. T. Hung, and G. A. Ateshian. Functional tissue engineering of articular cartilage through dynamic loading of chondrocyte-seeded agarose gels. *Journal of Biomechanical Engineering*, 122:252–260, 2000.

[60] O. Meincke, D. Kaempfer, H. Weickmann, C. Friedrich, M. Vathauer, and H. Warth. Mechanical properties and electrical conductivity of carbon-nanotube filled polyamide-6 and its blends with acrylonitrile/butadiene/styrene. *Polymer*, 45(3):739–748, Feb 2004.

[61] C. A. Mitchell, J. L. Bahr, S. Arepalli, J. M. Tour, and R. Krishnamoorti. Dispersion of functionalized carbon nanotubes in polystyrene. *Macromolecules*, 35(23):8825–8830, Nov 2002.

[62] E. Mooney, P. Dockery, U. Greiser, M. Murphy, and V. Barron. Carbon nanotubes and mesenchymal stem cells: Biocompatibility, proliferation and differentiation. *Nano Letters*, 8(8):2137–2143, 2008.

[63] L. Moroni, J. R. de Wijn, and C. A. van Blitterswijk. 3D fiber-deposited scaffolds for tissue engineering: Influence of pores geometry and architecture on dynamic mechanical properties. *Biomaterials*, 27:974–985, 2006.

[64] V. C. Mow, M. C. Gibbs, W. M. Lai, W. B. Zhu, and K. A. Athanasiou. Biphasic indentation of articular cartilage–ii. a numerical algorithm and an experimental study. *Journal of Biomechanics*, 22(8-9):853–861, 1989.

[65] V. C. Mow, M. H. Holmes, and W. M. Lai. Fluid transport and mechanical properties of articular cartilage: a review. *Journal of Biomechanics*, 17(5):377–394, 1984.

[66] V. C. Mow, S. C. Kuei, W. M. Lai, and C. G. Armstrong. Biphasic creep and stress relaxation of articular cartilage in compression: Theory and experiments. *Journal of Biomechanical Engineering*, 102(1):73–84, Feb 1980.

[67] A. Nimmagadda and P. McFetridge. Single walled carbon nanotubes: An assessment of biocompatibility for tissue engineering applications. *Cardiovascular Pathology*, 13:81–82, 2004.

[68] E. Oberdorster. Manufactured nanomaterials (fullerenes, C-60) induce oxidative stress in the brain of juvenile largemouth bass. *Environmental Health Perspectives*, 112(10):1058–1062, Jul 2004.

[69] S. W. O'Driscoll, A. D. Recklies, and A. R. Poole. Chondrogenesis in periosteal explants. an organ culture model for in vitro study. *The Journal of Bone and Joint Surgery*, 76(7):1042–1051, Jul 1994.

[70] RW Ogden and DG Roxburgh. A pseudo-elastic model for the Mullins effect in filled rubber. *Proceedings: Mathematical, Physical and Engineering Sciences*, pages 2861–2877, 1999.

[71] S. L. Passman, J. W. Nunziato, and E. K. Walsh. A theory of multiphase mixtures. pages 286–325, 1984. In: Truesdell, C.(ed.) Rational Thermodynamics, Berlin, Heidelberg, New York: Springer.

[72] R. D. Patton, J. Pittman, L. Wang, and J. R. Hill. Vapor grown carbon fiber composites with epoxy and poly (phenylene sulfide) matrices. *Composites Part A: Applied Science and Manufacturing*, 30(9):1081–1091, 1999.

[73] S. J. Peter, J. A. Nolley, M. S. Widmer, J. E. Merwin, M. J. Yaszemski, A. W. Yasko, P. S. Engel, and A. G. Mikos. In vitro degradation of a poly(propylene fumarate)/beta-tricalcium phosphate composite orthopaedic scaffold. *Tissue Engineering*, 3(2):207–215, 1997.

[74] R. B. Pipes and P. Hubert. Helical carbon nanotube arrays: mechanical properties. *Composites Science and Technology*, 62(3):419–428, 2002.

[75] W.H. Press, S.A. Teukolsky, W.T. Vetterling, and B.P. Flannery. *Numerical recipes 3rd edition: The art of scientific computing*. Cambridge University Press New York, NY, USA, 2007.

[76] P. A. Przybylo and E. M. Arruda. Experimental investigations and numerical modeling of incompressible elastomers during non-homogeneous deformations. *Rubber Chemistry and Technology*, 71(4):730–749, 1998.

[77] D. Qian, E. C. Dickey, R. Andrews, and T. Rantell. Load transfer and deformation mechanisms in carbon nanotube-polystyrene composites. *Applied Physics Letters*, 76:2868, 2000.

[78] A. Rasheed, M. D. Dadmun, and P. F. Britt. Polymer-nanofiber composites: Enhancing composite properties by nanofiber oxidation. *Journal of Polymer Science: Part B: Polymer Physics*, 44:3053–3061, 2006.

[79] R. L. Sah, Y. J. Kim, J. Y. Doong, A. J. Grodzinsky, A. H. Plaas, and J. D. Sandy. Biosynthetic response of cartilage explants to dynamic compression. *Journal of Orthopaedic Research*, 7(5):619–636, 1989.

[80] L. S. Schadler, S. C. Giannaris, and P. M. Ajayan. Load transfer in carbon nanotube epoxy composites. *Applied Physics Letters*, 73(26):3842, 1998.

[81] J. K. Sherwood, S. L. Riley, R. Palazzolo, S. C. Brown, D. C. Monkhouse, M. Coates, L. G. Griffith, L. K. Landeen, and A. Ratcliffe. A three-dimensional osteochondral composite scaffold for articular cartilage repair. *Biomaterials*, 23(24):4739–4751, Dec 2002.

[82] D. Shi, J. Lian, P. He, L. M. Wang, F. Xiao, L. Yang, M. J. Schulz, and D. B. Mast. Plasma coating of carbon nanofibers for enhanced dispersion and interfacial bonding in polymer composites. *Applied Physics Letters*, 83:5301, 2003.

[83] X. Shi, J. L. Hudson, P. P. Spicer, J. M. Tour, R. Krishnamoorti, and A. G. Mikos. Rheological behaviour and mechanical characterization of injectable poly (propylene fumarate)/single-walled carbon nanotube composites for bone tissue engineering. *Nanotechnology*, 16(7):S531–S538, 2005.

[84] M. L. Shofner, F. J. Rodriguez-Macias, R. Vaidyanathan, and E. V. Barrera. Single wall nanotube and vapor grown carbon fiber reinforced polymers processed by extrusion freeform fabrication. *Composites Part A: Applied Science and Manufacturing*, 34(12):1207–1217, 2003.

[85] A. A. Shvedova, Castranova V, E. R. Kisin, D. Schwegler-Berry, A. R. Murray, Gandelsman V, A. Maynard, and P. Baron. Exposure to carbon nanotube material: Assessment of nanotube cytotoxicity using human keratinocyte cells. *Journal of Toxicology and Environmental Health-Part A*, 66(20):1909–1926, Oct 2003.

[86] M. A. Soltz and G. A. Ateshian. Experimental verification and theoretical prediction of cartilage interstitial fluid pressurization at an impermeable contact interface in confined compression. *Journal of Biomechanics*, 31(10):927–934, Oct 1998.

[87] M. A. Soltz and G. A. Ateshian. Interstitial fluid pressurization during confined compression cyclical loading of articular cartilage. *Annals of Biomedical Engineering*, 28(2):150–159, 2000.

[88] M. A. Soltz, A. Stankiewicz, R. L. Mauck, C. T. Hung, and G. A. Ateshian. Direct hydraulic permeability measurements of agarose hydrogels used as cell scaffolds. *Advances in Bioengineering*, pages 229–230, 1999.

[89] R. L. Spilker, P. S. Donzelli, and V. C. Mow. A transversely isotropic biphasic finite element model of the meniscus. *Journal of Biomechanics; Journal of Biomechanics*, 25(9):1027–1045, Sep 1992.

[90] J. K. Suh and M. R. DiSilvestro. Biphasic poroviscoelastic behavior of hydrated biological soft tissue. *Journal of Applied Mechanics*, 66(2):528–535, 1999.

[91] P. R. Supronowicz, P. M. Ajayan, K. R. Ullmann and?B. P. Arulanandam, D. W. Metzger, and R. Bizios. Novel current-conducting composite substrates for exposing osteoblasts to alternating current stimulation. *Journal of Biomedical Materials Research*, 59(3):499–506, Mar 2002.

[92] J. M. Taboas, R. D. Maddox, P. H. Krebsbach, and S. J. Hollister. Indirect solid free form fabrication of local and global porous, biomimetic and composite 3d polymer-ceramic scaffolds. *Biomaterials*, 24(1):181–194, Jan 2003.

[93] N. H. Tai, M. K. Yeh, and J. H. Liu. Enhancement of the mechanical properties of carbon nanotube/phenolic composites using a carbon nanotube network as the reinforcement. *Carbon*, 42(12-13):2774–2777, 2004.

[94] L.H. Thomas. Elliptic problems in linear difference equations over a network. *Watson Sci. Comput. Lab. Rept., Columbia University, New York*, 1949.

[95] E. T. Thostenson and T. W. Chou. Aligned multi-walled carbon nanotube-reinforced composites: processing and mechanical characterization. *Journal of Physics D-Applied Physics*, 35(16):L77–L80, Aug 2002.

[96] E. T. Thostenson, Z. F. Ren, and T. W. Chou. Advances in the science and technology of carbon nanotubes and their composites: a review. *Composites Science and Technology*, 61(13):1899–1912, 2001.

[97] C. Truesdell and R. Toupin. *The Classical Field Theories*. Springer, 1960.

[98] E. H. Twizell. Non-linear optimization of the material constants in Ogden's stress-deformation function for incompressible isotropic elastic materials. *Journal of the Australian Mathematical Society, Series B*, 24:424–434, 1983.

[99] Colvin V. The potential environmental impact of engineered nanomaterials. *Nature Biotechnology*, 22(6):760–760, Jun 2004.

[100] S. F. Wang, L. Shen, and Y. J. Tongs. Preparation and mechanical properties of chitosan/carbon nanotubes composites. *Biomacromolecules*, 6(6):3067–3072, 2005.

[101] D. B. Warheit, B. R. Laurence, K. L. Reed, D. H. Roach, G. A. M. Reynolds, and T. R. Webb. Comparative pulmonary toxicity assessment of single-wall carbon nanotubes in rats. *Toxicological Sciences*, 77(1):117–125, Jan 2004.

[102] T. J. Webster, M. C. Waid, J. L. McKenzie, R. L. Price, and J. U. Ejiofor. Nano-biotechnology: carbon nanofibres as improved neural and orthopaedic implants. *Nanotechnology*, 15(1):48–54, 2004.

[103] J. Werner, B. Linner-Krčmar, W. Friess, and P. Greil. Mechanical properties and in vitro cell compatibility of hydroxyapatite ceramics with graded pore structure. *Biomaterials*, 23(21):4285–4294, Nov 2002.

[104] Y. Yang, M. C. Gupta, K. L. Dudley, and R. W. Lawrence. The fabrication and electrical properties of carbon nanofibrepolystyrene composites. *Nanotechnology*, 15(11):1545–1548, 2004.

[105] E.D. Yildirim, X. Yin, K. Nair, and W. Sun. Fabrication, characterization, and biocompatibility of single-walled carbon nanotube-reinforced alginate composite scaffolds manufactured using freeform fabrication technique. *Journal of Biomedical Materials Research Part B: Applied Biomaterials*, 2, 2008.